NAVAL POSTGRADUATE SCHOOL

MONTEREY, CALIFORNIA

DISSERTATION

EFFECTS OF DIVERSE VARIABLES ON RESISTIVITY, RHEOLOGY, AND NETWORK VISUALIZATION OF ELECTRICALLY CONDUCTIVE EPOXY-CNT COMPOSITES

by

Joel J. Hubbard

June 2022

Dissertation Supervisor: Claudia C. Luhrs

THIS PAGE INTENTIONALLY LEFT BLANK

REPORT DOCUMENTATION PAGE	*Form Approved OMB No. 0704-0188*

1. AGENCY USE ONLY *(Leave blank)*	**2. REPORT DATE** June 2022	**3. REPORT TYPE AND DATES COVERED** Dissertation

4. TITLE AND SUBTITLE EFFECTS OF DIVERSE VARIABLES ON RESISTIVITY, RHEOLOGY, AND NETWORK VISUALIZATION OF ELECTRICALLY CONDUCTIVE EPOXY-CNT COMPOSITES	**5. FUNDING NUMBERS** RM250 RMP0P
6. AUTHOR(S) Joel J. Hubbard	
7. PERFORMING ORGANIZATION NAME(S) AND ADDRESS(ES) Naval Postgraduate School Monterey, CA 93943-5000	**8. PERFORMING ORGANIZATION REPORT NUMBER**
9. SPONSORING / MONITORING AGENCY NAME(S) AND ADDRESS(ES) DOD Space	**10. SPONSORING / MONITORING AGENCY REPORT NUMBER**

11. SUPPLEMENTARY NOTES The views expressed in this thesis are those of the author and do not reflect the official policy or position of the Department of Defense or the U.S. Government.

12a. DISTRIBUTION / AVAILABILITY STATEMENT Approved for public release. Distribution is unlimited.	**12b. DISTRIBUTION CODE** A

13. ABSTRACT (maximum 200 words)

The addition of high-aspect ratio nanometric conductive fillers (i.e., carbon nanotubes [CNTs]) to an epoxy matrix has been shown to improve electrical conductivity by many orders of magnitude. These nanocomposites, well-suited for electrostatic dissipation and electromagnetic interference applications, are of intense interest to the aerospace industry where epoxy resins are already widely employed. Future adoption and commercial production efforts are limited by a lack of understanding of how electrical and rheological properties of uncured mixtures relate to the finished composite, how they change throughout the epoxy curing process, or how these materials are affected by extreme operating environments. To bridge these gaps, the viscosity and electrical properties of uncured mixtures were characterized and correlated to cured values, potentially allowing for quality control at a point in the production process where remediation is possible. Rare-earth oxide nanoparticles, europium-doped yttria, were synthesized into CNT walls, enhancing the contrast of the conductive network in scanning electron microscopy and micro-computed tomography while also granting deep-UV fluorescence. Lastly, in-situ electrical measurements of an epoxy-CNT composite were conducted under simulated low-earth orbit conditions with instantaneous decreases in resistivity as large as 60% being documented.

14. SUBJECT TERMS carbon nanotubes, CNT, electrically conductive composites, low-earth orbit, LEO, rare-earth oxide, CNT rheology	**15. NUMBER OF PAGES** 147
	16. PRICE CODE

17. SECURITY CLASSIFICATION OF REPORT	**18. SECURITY CLASSIFICATION OF THIS PAGE**	**19. SECURITY CLASSIFICATION OF ABSTRACT**	**20. LIMITATION OF ABSTRACT**
Unclassified	Unclassified	Unclassified	UU

NSN 7540-01-280-5500

Standard Form 298 (Rev. 2-89)
Prescribed by ANSI Std. 239-18

THIS PAGE INTENTIONALLY LEFT BLANK

Approved for public release. Distribution is unlimited.

EFFECTS OF DIVERSE VARIABLES ON RESISTIVITY, RHEOLOGY, AND NETWORK VISUALIZATION OF ELECTRICALLY CONDUCTIVE EPOXY-CNT COMPOSITES

Joel J. Hubbard
Lieutenant Commander, United States Navy
BSME, University of Nevada, 2009
MS, University of Nevada, 2011

Submitted in partial fulfillment of the
requirements for the degree of

DOCTOR OF PHILOSOPHY IN MECHANICAL ENGINEERING

from the

NAVAL POSTGRADUATE SCHOOL
June 2022

Approved by:

Claudia C. Luhrs
Department of Mechanical
and Aerospace Engineering
Dissertation Supervisor
Dissertation Chair

Anthony J. Gannon
Department of Mechanical
and Aerospace Engineering

Walter Smith
Department of Mechanical
and Aerospace Engineering

Carlos F. Borges
Department of
Applied Mathematics

Jonathan Phillips
Energy Academic Group

Approved by:

Garth V. Hobson
Chair, Department of Mechanical and Aerospace Engineering

Michael E. Freeman
Vice Provost of Academic Affairs

THIS PAGE INTENTIONALLY LEFT BLANK

ABSTRACT

The addition of high-aspect ratio nanometric conductive fillers (i.e., carbon nanotubes [CNTs]) to an epoxy matrix has been shown to improve electrical conductivity by many orders of magnitude. These nanocomposites, well-suited for electrostatic dissipation and electromagnetic interference applications, are of intense interest to the aerospace industry where epoxy resins are already widely employed. Future adoption and commercial production efforts are limited by a lack of understanding of how electrical and rheological properties of uncured mixtures relate to the finished composite, how they change throughout the epoxy curing process, or how these materials are affected by extreme operating environments. To bridge these gaps, the viscosity and electrical properties of uncured mixtures were characterized and correlated to cured values, potentially allowing for quality control at a point in the production process where remediation is possible. Rare-earth oxide nanoparticles, europium-doped yttria, were synthesized into CNT walls, enhancing the contrast of the conductive network in scanning electron microscopy and micro-computed tomography while also granting deep-UV fluorescence. Lastly, in-situ electrical measurements of an epoxy-CNT composite were conducted under simulated low-earth orbit conditions with instantaneous decreases in resistivity as large as 60% being documented.

THIS PAGE INTENTIONALLY LEFT BLANK

TABLE OF CONTENTS

THIS PAGE INTENTIONALLY LEFT BLANK

LIST OF FIGURES

LIST OF TABLES

THIS PAGE INTENTIONALLY LEFT BLANK

LIST OF ACRONYMS AND ABBREVIATIONS

CNT	Carbon Nanotube
CVD	Chemical Vapor Deposition
DOD	Department of Defense
DUV	Deep Ultraviolet
EDS	Energy Dispersive Spectroscopy
EMI	Electromagnetic Interference
ESD	Electrostatic Dissipation or Discharge
FY	Fiscal Year
HAADF	High-Angle Annular Dark-Field
HRTEM	High Resolution Transmission Electron Microscope
ISO	International Organization for Standards
LEO	Low-earth Orbit
Micro-CT	Micro-Computed Tomography
MWCNT	Multi Walled Carbon Nanotube
NDE	Non-Destructive Evaluation
NDT	Non-Destructive Testing
SEM	Scanning Electron Microscope
STEM	Scanning Transmission Electron Microscope
SWCNT	Single Walled Carbon Nanotube
TEM	Transmission Electron Microscopy
TGA	Thermogravimetric Analysis
UT	Ultrasonic testing
XRD	X-ray Diffraction

THIS PAGE INTENTIONALLY LEFT BLANK

ACKNOWLEDGMENTS

I would first like to thank my advisor and dissertation committee chair Professor Claudia Luhrs. The guidance and advice you provided throughout our studies kept me steady on course while also allowing me to learn along the way. Your willingness to make time to support your students, expertise in the field of material science, and consummate professionalism, should serve as a model for all educators and academics.

I would also like to thank the rest of my committee: Professor Anthony Gannon, Professor Carlos Borges, Professor Jonathan Phillips, and Professor Walter Smith. These last few years have presented unique challenges and constraints on both teachers and students. I truly appreciate you taking on another, in the form of this PhD student. The time you invested throughout this process has not been wasted and has thoroughly contributed to my success here at NPS.

To my research group, thank you for your support and encouragement over the last years. CDR Earp, your initial guidance, both in navigating the NPS landscape and getting up to speed with CNT-based composites, went a long way. Additionally, we wouldn't have been able to hit the ground running if it wasn't for all the initial work you did with this difficult material. I'd also like to thank Professors Zea and Tirano at the National University of Columbia, and Tugba Isik and Professor Ortalan at the University of Connecticut. It is because of our partnership that these studies are complete and tell the full story.

Lastly, I want to thank my family, Mike and Diana Hubbard, Averi and Chris Bencken, and my girlfriend, Kaleigh, and dog, Lucy. Your support through the last three years of isolation and academic tunnel vision has made this possible. Without your encouragement and unconditional love, this, and many other accomplishments, wouldn't have been possible.

THIS PAGE INTENTIONALLY LEFT BLANK

I. INTRODUCTION

A. MOTIVATION AND FOCUS

Advances in the production of multi-walled carbon nanotubes (MWCNT) grown via chemical vapor deposition (CVD) has resulted in the ability to produce sufficient quantities at costs that make commercial utilization possible. As a result, CNT composites, consisting of a polymeric matrix and MWCNT nanofiller, have been the subject of increased interest in the materials engineering community [1–4]. A subgroup of these materials, epoxy-CNT composites, stand out. Through the addition of CNTs to a previously insulating epoxy, electrically conductive composites can be fabricated. For instance, the addition of extremely low loadings of a commercial CNT pulp, $< 0.2\%$, can decrease the resistivity of aerospace grade epoxy 12 orders of magnitude (2.14×10^{15} ohm-cm $\rightarrow \sim 10^{3}$ ohm-cm) [5]. This makes the nanocomposite now suitable for electrostatic dissipation (ESD) and electromagnetic interference (EMI) applications [6–10], where bulk electrical resistivity of at least $10–10^{11}$ ohm-cm CNT is required [11]. The aerospace industry already relies on epoxy materials in a variety of applications including adhesives, thin films, and structurally when used in conjunction with a fiber substrate. The prospect of CNT addition improving electrical properties, while maintaining light weight and promising fracture toughness [12,13], fatigue resistance [14–16], coefficient of thermal expansion [17], and specific strength [18], make them particularly suited for aerospace components [6,7]. Successful development and deployment of these materials for these EMI and ESD applications requires a deep understanding of the epoxy-CNT composite's electrical properties during production, evaluation, testing, and operation.

This thesis presents studies conducted with epoxy-CNT composites regarding aspects that span from areas of opportunity during their production steps, to enhancement of contrast in imaging methods employed for their evaluation and identifying how electrical properties change under simulated in-service conditions. The following chapters are formed from previously published work that that was subjected to minor modifications meant to make it more suitable in a dissertation format. This format is often referred to as "stapling." Since these chapters have been published already in peer reviewed journals,

they are self-contained and meant to stand-alone as a complete and thorough study. The reader will notice that each section reaffirms the use of these epoxy-CNT composites for ESD and EMI applications, features a thorough review of similar research efforts, and contextualize the study within the existing body of work in that field as it pertains to electrically conductive composites.

Regarding the opportunities during the production stage, the aim of the study presented herein was to identify relationships between uncured epoxy-CNT mixture properties and that of the corresponding cured composite. A thorough literature review revealed that the study of electrical properties of uncured CNT polymeric mixtures is very limited. In fact, of thousands of articles devoted to CNTs and their composites, only a small fraction of those address electrical properties. Those that do address electrical properties tend to focus primarily on the properties associated with the cured CNT composites. To the best of our knowledge, the published research that characterizes uncured properties, such as the viscosity of the CNT mixtures, does not establish a clear connection between the uncured and cured states, leaving any possible relationship to conjecture and extrapolation. A deeper upstanding of the electrical and rheological properties of an uncured CNT-epoxy mixture, and how these translate to the electrical performance in a cured composite is required as adoption continues. This knowledge can potentially allow screening and quality evaluation at time in production when changes can still be affected and would be of great value to industry moving forward. Thus, Chapter II herein establishes the relationship between the uncured electrical resistivity and viscosity of epoxy-CNT mixtures, and the electrical resistivity of the resulting composite after the addition of a hardening agent and curing. Thermal activation of the CNT filler, of varying durations, was used as a tool to manipulate these parameters within the study. The published work is entitled “Effects of Thermal Activation on CNT Nanocomposite Electrical Conductivity and Rheology” and was previously published the 2022 *Polymers* volume 14, issue 5, a special issue on Advances in Multifunction Polymer-Matrix composites.

In the area of CNT epoxy composites evaluation, the objective of the efforts presented aimed to enhance contrast in SEM imaging of CNT composites for better network detection. After curing, non-destructive evaluation of the electrically conductive

nanocomposite, that could point out areas where the CNT are agglomerated or the existence of large areas devoid of CNT, is difficult, in part, due to the scale of the filler. While existing methods focus on defects that impact mechanical properties and can detect flaws in the epoxy matrix, e.g., cracks or excess porosity, evaluation of the nanofiller dispersion, more relevant for the electrical properties, has not been fully developed. Several methods of evaluating this network and its dispersion have been proposed. For instance, infrared imaging has been suggested for non-destructive evaluation of CNT dispersion [19]. However, this technique's accuracy relies on uniform surface finish and would be limited to providing data from the top layers of the material being examined. Other techniques such as voltage-contrast imaging in scanning electron microscopy (SEM) [20–22], transmission electron microscopy (TEM) [23], and micro-computed tomography (micro-CT) [24], can be destructive, feature small sample areas, and are plagued by unique challenges working with a conductive material in an insulating matrix. More importantly, visualization of the CNT network is rendered even more difficult by poor contrast between the conductive filler and surrounding polymeric matrix. Techniques for evaluating finished composites are essential for inspection and testing and improvements to contrast of existing techniques would be welcomed. Chapter III and IV of this thesis pertain to finished composites and detection of defects and visualization the CNT network – factors that can influence electrical performance. The manuscript "Introduction of Rare-Earth Oxide nanoparticles in CNT-based Nanocomposites for Improved Detection of the Underlying CNT Network," comprises Chapter IV and was published in *Nanomaterials* volume 11, issue 9 in 2021 – part of the special edition on carbon-based nanocomposites.

The contributions to expanding the knowledge of these composites during in-service conditions consisted of determination of the instantaneous impact of extreme operating conditions on electrical properties. The severe conditions that accompany aerospace applications, for example, in low-earth orbit (LEO), require robust and resilient materials. Materials utilized in these environments would face exposure to atomic oxygen (AO), ultraviolet radiation (UV), thermal cycling, and high vacuum, and are all known to influence CNT material [25–27]. Several reports have examined CNT composite behavior under similar conditions, but have focused on initial properties and those after a period of

exposure lasting sometimes years [24,28,29]. The transient impact to the electrical properties epoxy-CNT composites produced by these extreme conditions, and their reversibility has not been quantified. An understanding of how long these electrical changes take to develop, and their permanence, would allow for improved design and incorporation of these nanocomposites. Chapter V presents our study of the instantaneous changes that the electrical properties of epoxy-CNT composite suffer in a LEO operating environment. This was originally published as the manuscript "Electrical behavior of CNT epoxy composites under in-situ simulated space environments" in *Composites Part B: Engineering,* volume 219, in 2021.

The focus of the research presented in this document has been to build a clearer understanding of the electrical properties and underlying CNT network in CNT-based epoxy nanocomposites and how these properties change during production, evaluation, testing, and operational conditions. By answering several questions, an opportunity exists to improve upon the existing body of work and contribute to the field:

1. Could the electrical properties of a CNT polymeric mixture be determined prior to curing and related to those of finished nanocomposite?
2. How does thermal activation affect the rheology of an uncured mixture and does this functionalization technique modify the electrical properties of the finished nanocomposite?
3. Can existing non-destructive evaluation (NDE) technology be utilized to investigate epoxy-CNT composites effectively?
4. Can methods of visualizing a CNT network be improved while maintaining the required electrical properties for EMI and applications?
5. How do extreme operating conditions like, vacuum, UV irradiation, and temperature influence the electrical performance of the composite in real-time? Are these changes detrimental and permanent?

To that end, the following chapters catalog several efforts designed to answer these questions and more. The viscosity and electrical resistivity of uncured CNT-epoxy

mixtures are characterized and presented alongside optical analysis of CNT bundle structure and electrical performance of the corresponding cured nanocomposite—allowing direct correlation between behavior of the in-process CNT-epoxy mixture and that of the final product. Regarding evaluation of these nanocomposites, a conventional method of non-destructive evaluation, ultrasonic testing, was characterized for the ability to detect flaws in a CNT-epoxy nanocomposite with on CNT loading, flaw type, and size being identified. Additionally, efforts to improve existing technology, SEM and micro-CT imaging, were made through the introduction of rare earth oxide (Eu:Y_2O_3) synthesized on thermally activated CNT bundles and allowed improvements in contrast and detection capability while exhibiting deep ultraviolet (DUV) florescence. The effects of an extreme, but likely operational environment, low-earth orbit, was also characterized. Through this, the instantaneous effects of vacuum, solar irradiance, and temperature fluctuations, used to simulate LEO, were documented and their reversibility over a matter of weeks was examined.

B. BACKGROUND

The previous section outlined the impetus for this research and briefly framed the need for CNT-nanocomposites in the aerospace industry and the importance of a deeper understanding of their electrical properties from production through deployment. This section will introduce the reader to the materials and concepts fundamental to the studies contained in Chapter II through V. A review of carbon nanotube structures and the epoxy matrix chosen for this study is provided. Additionally, familiarity with percolation theory and the importance of CNT dispersion is also necessary, and an introduction is provided clarifying these relationships as they pertain to the development of electrical properties within electrically conductive composites. The results of other published studies on electrical resistivity are also summarized and offer a starting point for context when viewing the results obtained in later chapters. Lastly, this research takes place at Naval Postgraduate School, an institution heavily invested on the interests of the U.S. Department of the Navy and U.S. Department of Defense (DOD). For that reason, a brief synopsis of nanotechnology and nanomaterial interest and congressional funding within the DOD is

included. However, financial commitments and interest in research efforts such as these are not relegated to the DOD – private industry also pushes for advancement in these areas.

1. Epoxy-CNT Nanocomposites

a. Filler Material - Carbon Nanotubes

Carbon nanotubes were formally introduced by Iijima in 1991 after observing "needle-like" tubes consisting of "coaxial tubes of graphitic sheets" [30]. Hindsight has revealed that various groups, as early as the 1960s, may have encountered what we now know to be CNTs during the course of their research on carbon whiskers or fibers through pyrolysis of hydrocarbons [31]. The first being Bacon et. Al. [32] and later Endo et. Al. [33,34]. Originally only identified as MWCNTs, the existence of single-walled variety along with differing chirality was documented in a 1993 issue of nature by Iijima et al. [35].

Carbon nanotubes can be described most simply as rolled up sheets of graphene, consisting of sp2 carbon atoms arranged in a hexagonal arrangement [10]. They are found in two forms, single-walled and multi-walled (SWCNT or MWCNT), with MWCNT being composed of concentric layers of these graphitic tubes held together by Vander Waals forces. DWCNT (double walled CNT) is sometimes used to refer to MWCNTs that consist of only two layers. Tube diameter varies depending on fabrication conditions and methods; however, SWCNT are smaller with approximate diameters of 1 to 2 nm, while MWCNT diameters are much larger from 10 to 240 nm [37]. CNTs have been synthesized by three primary methods: chemical vapor deposition (CVD), arc discharge, and laser ablation. Other methods exist, such as plasma synthesis [38] and pyrolysis of hydrocarbons [39], but have not seen widespread adoption. The last decade has seen significant advances in the production of these nanostructures on scales that can support commercialization and facilitate nanocomposite production [1]. More specifically, carbon nanotube (CNT) production through chemical vapor deposition (CVD) processes has expanded the availability of this highly lauded carbon structure, resulting in an increase in both research and industry implementation.

The orientation of the graphene sp2 hexagonal structure relative to the axis of the CNT tube can vary. This is referred to as chirality and comes in 3 different configurations: armchair, zigzag, and chiral. An illustration of the different chiral forms and their origination in a CNT structure can be viewed in Figure 1. When formed as a SWCNT, the chirality determines the electrical properties of the CNT, with armchair chirality being the most electrically conductive [31]. The chirality of MWCNTs is more ambiguous, with published studies documenting MWCNT of differing chirality [40,41] as well as uniform chirality [42,43]. Additionally, electrical transport mechanism are more complicated with the potential for interactions between concentric tubes and chirality [44].. As the mechanical properties of CNT nanocomposite have a long history of application in aerospace, these properties are more widely studied [13,18,45] than electrical properties. The focus in this study is the increasingly important, yet poorly understood, electrical properties of the bulk composite material.

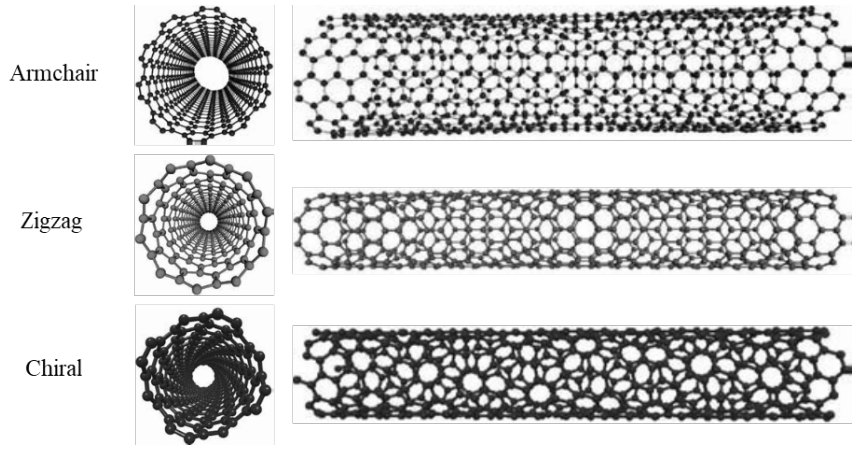

Figure 1. Illustration of the different types of SWCNTs chirality.
Source: [31].

The CNT pulp used in this study is a commercial product available from Nanocomp Inc. (Huntsman Corporation, Merrimack, NH, USA). The MWCNTs are grown via CVD over an iron catalyst as a sheet before being reduced to a pulp consisting of agglomerated bundles of CNTs 0.05 mm in diameter and up to 1 mm long with individual tube diameters

of ~30 nm [46]. The product is used as received, i.e., the iron catalyst nanoparticles are left in the pulp, notably this is also standard industrial practice.

b. Matrix material

Epoxy-CNT Nanocomposites are formed through the addition of CNT filler to an epoxy resin and subsequently curing to form the finished composite. Despite the existence of many polymeric composites, e.g., ABS [47], polypropylene [48], polycarbonates [49], and more [50–53], the studies contained herein focus on those utilizing epoxy resin for the surrounding matrix. More specifically, an aerospace grade epoxy resin, EA9396, well suited for aerospace applications due to its low volatile content and favorable mechanical properties. Loctite EA 9396 AERO (Henkel Corporation, Dusseldorf, Germany) is marketed for aerospace applications as an adhesive or in conjunction with a fiber substrate as a repair material [54] with highlighted features being: flexibility and toughness, high temperature, chemical, and compression load resistance [55]. Material properties of the EA 9396 epoxy can be seen in Table 1.

Table 1. Various properties of EA 9396 as reported by the manufacturer. Adapted from:[56]

Lap shear Strength	22.8 MPa (-55 ºC) 24.1 MPa 22.0 MPa (82 ºC) 8.6 MPa (350 ºC)	Volume resistivity	2.14×10^{15} ohm-cm
Tensile strength	55.2 MPa	Surface resistivity	3.17×10^{14} ohm-cm
T_g Dry	98 ºC* / 176 ºC $^{\Delta}$	Thermal conductivity	0.20962 W/mK
T_g Wet	63 ºC* / 107 ºC $^{\Delta}$	Coefficient of thermal expansion	70.7 µm/mºC (40ºC)
Viscosity	3.5 Pa S	Density	1.14 g/cm^3

Note: unless otherwise stated, reported values are at 25ºC

* Source: [56], $^{\Delta}$ Source: [54]

The epoxy is a two-part thermosetting epoxy with Part A consists of an epoxide and bis-phenol containing compounds and Part B being the polyfunctional amine hardener [57]. Per the manufacturer, Part A and Part B are mixed 10:3 by weight and can be cured at room temperature 25 ºC in 3–5 days or at 66 ºC in 1 h. Phenol and Elevated curing temperatures result in slight improvements to mechanical properties [54,56]. Previous analysis within the research group has also revealed that considerable improvements in moisture content and porosity are achieved through curing at elevated temperatures. For these reasons, curing is conducted at 66 ºC in all experiments of this study except for one sample in Chapter III for ultrasonic testing (UT).

c. Percolation Theory and Dispersion

Percolation theory, the notion of electrical flow through a blend of conductive and non-conductive media, has been the subject of research and several books [58,59]. It's governed by the notion that that the electrical properties of the bulk material are tied to the ability of the low concentration conductive material, here CNT, to form a conductive network in the host non-conductive matrix. The likelihood of the formation of a conductive path between elements of a randomly dispersed conductive filler in an insulating matrix depends on a variety of factors. Dimensionality of the filler material, i.e., its aspect ratio [60], volumetric dispersion within the surrounding matrix [61,62], and its tendency to agglomerate [63] can all influence overall electrical behavior. Within this theory is the percolation threshold, which the material transitions from behaving as an insulator to capable of electrical conduction [64] and is typically quantified as wt% or vol% of the filler material.

These factors are often intertwined and co-dependent. For instance, higher aspect ratio fillers like CNT are more likely to intertwine, making agglomeration more likely, and impeding mechanical dispersion efforts. Further, poor matrix-CNT interaction on the CNT walls can influence dispersion efforts and lead to agglomeration when affinity for CNT bundles is favored. Functionalization of tube walls, to facilitate solubility and decrease van der Waals forces, between tubes can ameliorate this to a degree and is discussed further in

Chapter I. As these factors are not directly related to percolation theory, discussion will end here and resume when warranted in the studies that follow.

Directly related to percolation theory is the aspect ratio of the filler material. It's influence on percolation threshold and has been demonstrated both theoretically [65,66] and experimentally [62,67]. The high aspect ratios of CNT have led to percolation thresholds common reported as <.1wt% CNT loading [5,68,69] with thresholds as low as 0.0025 wt% reported for long, aligned MWCNT bundles [64]. Composites fabricated in a similar fashion with graphite nanoplatelets have experimentally determined the threshold as ~ 4 wt% [70], while classic percolation theory for a spherical filler is substantially higher for truly random mixtures with spherical conductive phase material [71–73]. In sum, higher aspect ratios lead to lower percolation thresholds due to a higher probability of there being a conductive path. Figure 2 illustrates the expected behavior of electrical resistivity as the percolation threshold is crossed.

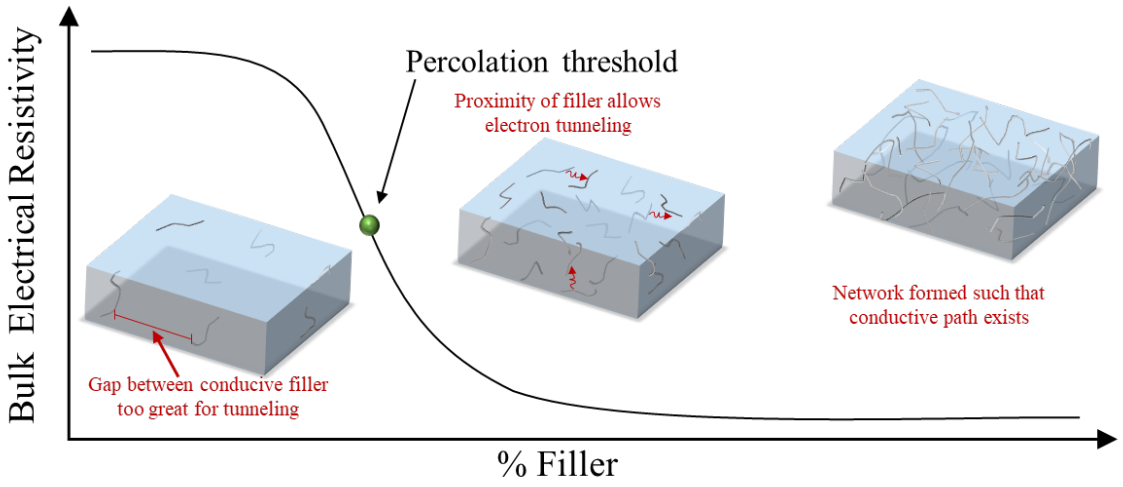

Figure 2. Resistivity behavior during transition in relation to the percolation threshold. Adapted from [74].

At loadings below the percolation threshold, there is no viable conductive network for charge to flow. Above the percolation limit the filler forms a connected network for electron to travel. Between these extremes, the filler does not form a complete network,

and electrical conduction can only occur through a quantum phenomenon known as electron tunneling [67,75–77]. This mechanism is outside the scope of the present study and readers are directed to the previously cited literature for further discussion.

Dispersion of the conductive filler also plays a role in establishing uniform conductive properties in the composite. However, its impact can vary depending on filler content. Figure 3 illustrates this point. For loadings above the percolation threshold, there exists an “optimal” level of dispersion. With poor dispersion, there could be excellent conductivity in that local region, but poor bulk electrical conductivity. As dispersion increases and the conductive nanofiller is distributed, it’s tendency to agglomerate, results in concentrated areas (rich with CNTs) and excluded volumes (devoid of CNTs). This is ideal for facilitating a conductive path as it has the effect to concentrating the conductive media into less volumetric area and result in significant decreases in resistivity. From this point on, increasing the dispersion through further mixing cycles can breakup these excluded volumes and decrease resistivity. At lower filler loadings the electrical resistivity of the bulk composite is less sensitive to dispersion. Due to the scarcity of conductive media, bulk resistivity experiences little change regardless of dispersion, solely due to there being a lack of a conductive path. While not studied directly, this is the basis for why the control of dispersion and filler content is critical to ensuring uniform properties in the resulting composite. For further discussion on this topic, and its mechanisms the reader is encourage to consult reference [5].

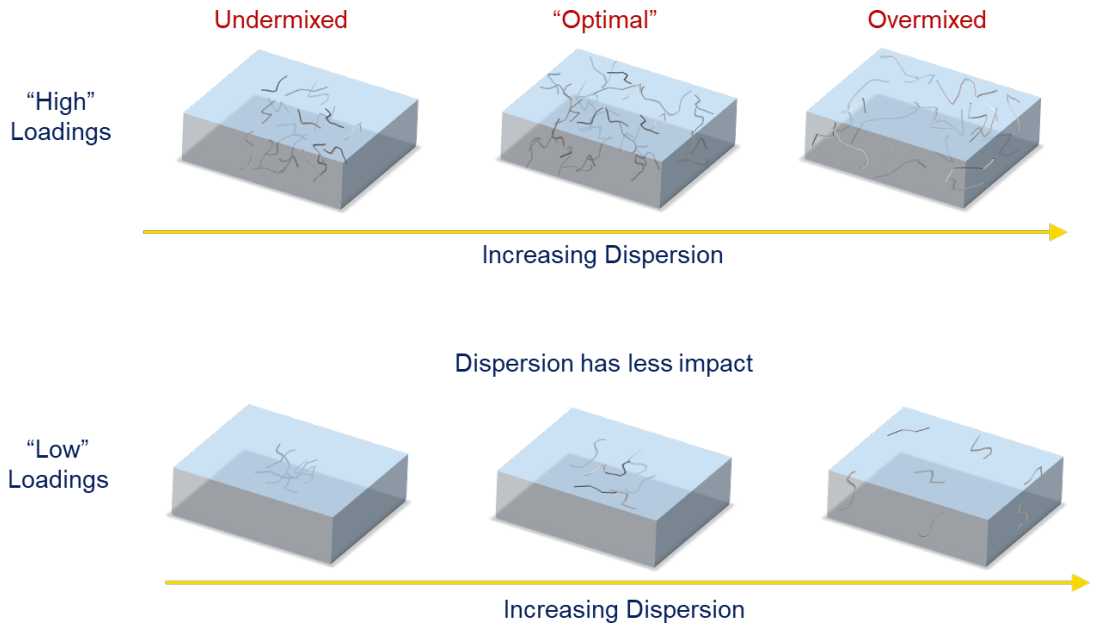

Figure 3. Dispersion effects on bulk electrical resistivity.

d. Electrical resistivity

These nanocomposites can be formed in conjunction with a substrate, as a solid structural material, or as studied here, without a substrate. This method is particularly attractive when a charge dissipation path on top of a complex shape is desired or when patterns of electrically conductivity thin films are desired. For EMI and/or ESD applications the electrical resistivity presented of the bulk composite must be between ~10-10^6 and 10^6–10^{11} ohm-cm, respectively [11]. Table 2 presents the results of many studies on CNT-epoxy nanocomposites with loadings ranging from 0.4 wt% to as high as 15 wt%. Note that in all cases, the resulting materials would be suitable for these applications. This serves as a baseline for the expected electrical performance of these materials and will be compared against in future chapters.

Table 2. Electrical properties of various epoxy-CNT composites studied by other groups. Adapted from [78].

CNT Type	CNT wt% studied	Dispersion method	ρ (Ohm-cm)	Source
Aligned MWCNT	0.01	Shear mixing	5×10^{1}	[64]
MWCNT	0.18	Solution mixing	2.5×10^{2}	[68]
SWCNT	0.21	High-frequency sonication	8.33×10^{4}	[79]
SWCNT/DWCNT	0.4	Solution mixing	1×10^{3}	[80]
SDS suspended MWCNT	0.5	Bulk mixing	4×10^{8}	[81]
MWCNT	0.5	Calendering process	1×10^{4}	[82]
MWCNT	0.75	Roll milling	1×10^{2}	[83]
Palmitic acid mod. CNT	0.8	Mechanical mixing	1.45×10^{4}	[84]
Oxidized MWCNT	1	Solution mixing	1×10^{3}	[85]
Pristine MWCNT	1	Solution mixing	1×10^{3}	[86]
MWCNT	1.4	Solution mixing	2×10^{2}	[61]
CNT	2.5	Solution mixing	7.69×10^{3}	[87]
MWCNT	4	Bulk mixing	5×10^{2}	[88]
MWCNT	5	Calendering process	2	[89]
MWCNT	10	Solution mixing	3.33×10^{4}	[90]
SWCNT	15	Solution mixing	10	[91]

2. Department of Defense and Nanomaterial Interest

Nanomaterials have the potential to offer properties superior to conventional engineering materials. For this reason the Defense Nanotechnology Research and Development program was established by Congress with the authorization of the 2013 National Defense Authorization Act (NDAA) [92]. The primary focus was to "discover, control, and exploit unique phenomena of military importance that may be encountered in materials at sub-100 nm length scales." [93]. It was the Department of Defense's vision to establish research programs in this burgeoning field to safekeep technical superiority and meet security goals. The potential for these nanoscale materials was not limited to the

United States. China revealed through the Chinese Academy of Science nearly as much investment on nanomaterials as on their national defense [93]. Japan, Singapore, and many European countries took up similar efforts during this timeframe as well. For example, Sweden in "Defense Applications of Nanocomposite Materials" [18] and Australia with "Advanced Materials and Manufacturing— Implications for Defence to 2040" [94,95], make similar arguments that the future of defense lies in successful development of these technologies

In support of this effort, each military service in the United States provided a list of goals and challenges in the areas of fundamental phenomena and processes, materials, manufacturing, and many others to guide research efforts. Additionally, collaborations with other agencies outside the lifelines of the DOD structure were targeted; this can be seen in Table 3. What becomes evident is that the effort is not an isolated effort, solely for the purposes of warfighting, but a government-wide effort to establish research programs supporting everything from warfighting efforts to medical treatments to environmental research. Now, 17 years after inception, an excess of $31 billion has been invested in research and development efforts at the nano-scale with 1.7 billion from FY21 alone [96].

Table 3. DOD collaborations on nanomaterial development with other agencies. Source [93].

Areas of Interest	DOE	NASA	NSF	NIST	NIH
Quantum computing	X	X	X	X	
Directed energy (DE)	X	X			
Thermal energy conversion	X	X			
Manufacturing			X	X	
R&D partnerships	X	X	X		
Electrodes and catalysts	X	X	X		
Tumor destruction					X
Materials research centers			X		
CB defense	X				
Fiber photocells/ batteries		X			

These efforts have already resulted in a push for implementation within the aerospace industry with both the F-35 Lightning [97] and Army helicopter [98] programs looking to utilize components with CNT integration. Another area that could benefit from the employment of developed nano materials is unmanned aerial vehicles (UAVs). A United States Air Force (USAF) report from 2013 anticipated its UAV inventory growing from ~100 to more than 1400 by 2035 [99]. Optimization of airframe weight, efficiency, and endurance are identified as significant hurdles and can be improved through these technologies [100]. EMI and ESD applications increase resiliency against both environmental and malicious attacks in the electromagnetic spectrum. Employing electrically conductive composites can result in weight savings, benefiting military aircraft and spacecraft through increased payload capabilities and on-station time.

THIS PAGE INTENTIONALLY LEFT BLANK

II. EFFECTS OF THERMAL ACTIVATION ON CNT NANOCOMPOSITE ELECTRICAL CONDUCTIVITY AND RHEOLOGY

A. BACKGROUND

This chapter was previously published in the special issue of *Polymers* by MDPI on Advances in Multifunctional Polymer-Matrix Composites [101]. Minor edits and additions have been made to adapt the text to the current manuscript.

Many industries are now utilizing nanocomposites due to the enhanced material properties achieved with relatively low nanofiller loadings. One such nanocomposite, carbon nanotube (CNT) epoxy composites, is particularly attractive to the aerospace industry, where favorable electrical properties can be incorporated into structural and adhesive components. CNT's high aspect ratios enable the generation of electrically conductive composites at extremely low loadings [5,64,68,102]. The reduced resistivity of these materials makes them appealing to a wide variety of industries where electrostatic dissipation (ESD) or electromagnetic interference (EMI) solutions are needed [7,10,103–106].

The conductivity of the finished material is primarily a function of nanofiller loading and its dispersion within the surrounding matrix. Inconsistent dispersion resulting in agglomerated areas of CNT bundles or areas devoid of CNTs can occur during the mixing and stages of production. The resulting inhomogeneity in these localized areas can have detrimental effects on the material, potentially causing unreliable performance, hotspots, or premature failure [107].

Efforts to validate complete CNT dispersion in the finished composite product have employed various techniques. Several groups utilized scanning electron microscopy (SEM) employing voltage or charge contrast imaging to identify CNT bundles within a composite but are limited in practicality for commercial use due to the small sample area and destructive nature of the sample preparation for analysis [20,21,108–110]. In [111] rare-earth oxides are utilized to increase the contrast of CNT microstructure in SEM and micro-computed tomography images, and a novel technique utilizing UV-florescence properties

of the synthesized nanoparticles is proposed. Pantano et al. [19] proposed infrared imaging as a technique to identify defective areas but could potentially be limited by resolution and analysis depth. In all cases, the finished nanocomposite is inspected after fabrication is completed and the dispersion has already been established, successfully or not.

Functionalization of the outer CNT surface has been explored as a method to increase solubility or interaction between the CNT and dispersing medium, e.g., solvent or polymer. Approaches typically involve the covalent or noncovalent attachment of chemical groups meant to interact with the matrix material or through the reduction of the CNT surface energy and van der Waals forces [112]. Methods vary widely but have included the attachment of chemical groups such as aminophenyl ($C_6H_4NH_2$) and nitrophenyl ($C_6H_4NH_2$) for use in a liquid crystalline polymer [113], polymer functionalization through styryl-grafted MWCNTS [53], and metal or rare-earth oxide attachment [111,114,115]. More straightforward methods of thermal activation or annealing at low temperatures in an oxygen atmosphere have been used to reduce the amount of amorphous carbon, produce defect sites, and increase oxygen-containing functional groups on the CNT surface—resulting in hydrophilic behavior and enhanced dispersion in organic solvents [116–119]. Overall, surface functionalization can be tailored to the application and can lead to improvements in thermal, mechanical, and electrical properties of the resulting composites by improved dispersion and interaction with the surrounding medium.

Additionally, increased nanofiller loading or surface functionalization causes rheological changes in CNT polymeric mixtures. The correlation of mixture viscosity to the dispersion CNT filler was first documented in [120] and found to vary by CNT wt%. The rheological behavior of CNT–polymer composites, e.g., polycarbonate, polyethylene, and various others [121], as well as epoxy resin composites [122–124] have been characterized. The focus has often been centered on changes in the viscosity of the solution or melt mixture the CNTs are added to. The effects of utilizing viscosity-reducing agents have also been explored [125].

Characterization of the effects of thermal activation/annealing on the electrical and rheological properties of uncured epoxy mixtures and the resulting cured composite have not been conducted. The study described in the next sections of this manuscript expands

on the existing body of knowledge by characterizing the effects varying activation time has on the electrical conductivity and rheology of an uncured CNT–epoxy mixture, cured composites electrical resistivity, as well as the resulting changes to the phases present and the CNT microstructure. As the use of nanocomposite technologies mature and expand, the need for quality control measures becomes increasingly important to ensure product consistency. The information contained in this study expands the understanding of how production techniques affect end-product performance and can enable the development of other paths for assessing composite properties prior to curing.

B. MATERIALS AND METHODS

1. Nanofiller and Matrix Materials

Composite synthesis was conducted with unactivated and activated CNT pulp. The CNT pulp was provided by Nanocomp Technologies Inc. (Huntsman Corporation, Merrimack, NH, USA). The multiwall carbon nanotubes (MWCNTs) received were grown as a sheet, produced from nanoparticles of iron that served as catalyst in a chemical vapor deposition process. The resulting product was then reduced to a pulp using an industrial burr mill and holland beater resulting in intertwined bundles approximately 1 mm in length and 0.05 mm in diameter [46] with an iron content of approximately 25.6 wt% [111]. This corresponds to a bundle aspect ratio of ~20. Aspect ratios for individual CNT are considerably higher given that CNT diameter is orders of magnitude smaller than the bundles they comprise.

The unactivated pulp was subjected to an activation process through heating at 500 °C in an open tube furnace (Thermo Scientific Lindberg/Blue M model TF55035A-1, Waltham, MA, USA) for 1, 2, or 2.5 h. Composite samples (cured and uncured) were fabricated with unactivated, and 2.5 h activated CNTs for 0.014 and 0.2 wt% CNT loadings. Composites with 0.75 wt% loading were analyzed in an unactivated state and with activation times of 1, 2, and 2.5 h.

The matrix of the fabricated nanocomposites consisted of Loctite's EA9396 two-part aerospace epoxy (Henkel Corporation, Dusseldorf, Germany). The cured epoxy has a reported electrical resistivity of 2.14×10^{15} Ohm-cm [56].

2. Sample Synthesis

Unactivated and activated CNTs were dispersed in the epoxy matrix using a FlackTek asymmetric speed mixer (Landrum, SC, USA). Five dispersion cycles were utilized with varying speeds and are featured in Table 4. Low vacuum was applied for 3 min between each dispersion cycle to reduce air entrapment.

Table 4. Steps of the synthesis process for cured and uncured CNT nanocomposite samples.

		Cycle 1		Cycle 2		Cycle 3		Cycle 4			Cycle 5	
Cured Samples	Part A + CNTs Added	Low Speed (1 min)	3 min Vacuum	Medium Speed (2 min)	3 min Vacuum	High Speed (1 min)	3 min Vacuum	High Speed (1 min)	Part B Added	3 min Vacuum	High Speed (1 min)	1hr at 66ºC
Uncured Samples												

Both cured and uncured samples were analyzed in this study. Samples were synthesized using a ratio of 100:30 by weight Part A to Part B and subsequently cured at 66 °C for 1 h. Uncured samples, used for resistivity measurements, and all viscosity determinations, were created without adding the corresponding amount of hardening agent, Part B, or subjecting to elevated temperatures.

3. Resistivity Measurements

Resistivity was measured directly from prefabricated circuit boards. The boards allow for eight individual measurements of the subject material. The experimental setup and corresponding equations can be found in [111]. Samples were tested without Part B in an uncured state through the application and leveling of a thin film on the circuit board. Cured samples were measured after undergoing the curing process already described. The voltage potential across a 1 cm × 1 cm sample area was measured with a generic digital multimeter under a 5 µA current supplied by a 2400 Keithley source meter (Tektronix, Inc., Beaverton, OR, USA). The epoxy film thickness of cured samples was determined by cross-sectioning and examination via a Nikon Epiphot 200 metallurgical microscope

(Nikon, Tokyo, Japan). Uncured sample thickness is approximately the same as the thickness of the tape used to stencil the sample area (0.19 mm).

4. Sample Characterization

Analysis of the crystalline phases present in the unactivated pulp and at various levels of activation were resolved via X-ray diffraction analysis (XRD) with a Rigaku Miniflex 600 (Woodlands, TX, USA) operating with a Cu source.

CNT bundle characteristics of cured composites were obtained via a metallurgical microscope Nikon Epiphot 200 (Melville, NY, USA). Samples were polished progressively to a 4000 grit and then imaged at 50× magnification.

Raman analysis of CNT pulp samples was conducted using a Renishaw In-via Confocal Raman Microscope (West Dundee, IL, USA). The sample was focused at 50× magnification before being excited with a 633 nm HeNe source utilized in conjunction with 1800 l/mm grating. The data presented represent the average of four locations for each sample.

Viscosity measurements were determined by a Bohlin C-VOR Rheometer acquired from Malvern Instruments Worcestershire, UK. The data were collected at 25 °C using a parallel plate configuration. The diameter of the plate was 20 mm with a gap of 0.5 mm. Data were recorded in oscillatory mode at a fixed frequency of 1 Hz between strains of 1 and 1000%.

C. RESULTS AND DISCUSSION

1. Activation Effects on Sample Mass and Phases Present

Thermal activation of the CNT pulp at elevated temperatures results in mass loss due to the oxidation of surface carbon to form CO and CO_2. Figure 4 presents the mass of CNT remaining after the sample undergoes the activation process. As shown, 93.66, 62.46, and 50.78% mass remains after 1, 2, and 2.5 h activation, respectively. While there is a change in mass associated with thermal activation, the CNT pulp utilized to fabricate composites of a target wt% were weighed after this process took place.

Additionally, as C==C bonds are broken, oxygen species are introduced as a form of covalent functionalization to the CNT surface [119]. This observation was confirmed in a study by Chen et al., based on X-ray photoelectron spectroscopy binding energy peaks, were assigned to ether C-O-C and quinone C=O during the analysis of CNT pulp thermally activated for durations of 30–120 min at temperatures of 350–550 °C. Increased temperatures were found to preferentially target quinone group functionalization while duration was found to have a minimal effect [118].

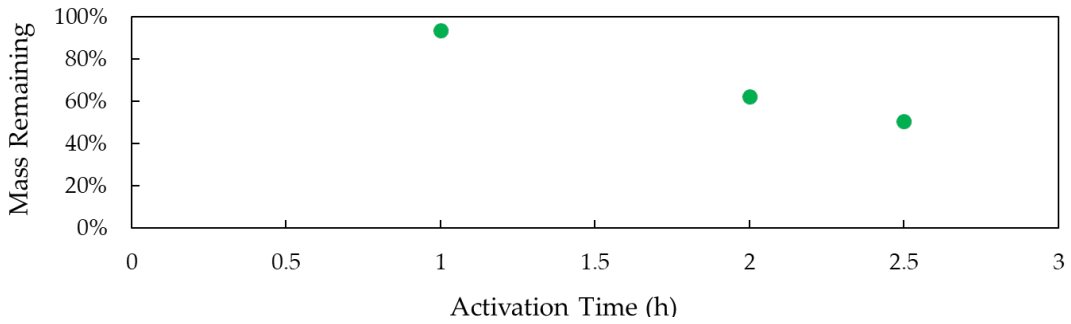

Figure 4. The percentage of remaining mass as a function of activation time.

The CNT pulp was not treated/cleaned prior to the incorporation of nanotubes into the epoxy mixture, that is, the iron catalyst leftover from the CVD process employed to fabricate the CNT remains present. This approach emulates the process currently employed by industry; the pulp is dispersed into the epoxy as received without being freed of the catalyst. As a result, the thermal activation, apart from modification of the carbon surface, leads to the oxidation of the remaining iron catalyst. Thus, the mass losses represented in Figure 4, and the properties found and described in the next sections, include both the loss of carbon and the oxidation of iron particulates.

XRD analysis was performed to determine the effects of thermal activation on crystalline phases in the CNT pulp. The diffraction pattern of the unactivated and activated CNT pulp is revealed in Figure 5. The unactivated CNT pulp consisted of primarily two phases, sp2 carbon arranged as tubular structures composed of rolled-up graphene sheets (CNT), and iron. As the activation time increases, the iron catalysts suffer progressive oxidation; FeO is not detected in the samples activated for 1 h and is likely to only be

present only during the initial steps of the reaction, instead, Fe_3O_4 and Fe_2O_3 peaks are identified. From 1 h to 2 h, the reflections corresponding to metallic iron completely disappear. The reflections of iron (II, III) oxide (Fe_3O_4), and iron (III) oxide (Fe_2O_3) dominate the pattern, with a marked reduction in the intensity of the peaks corresponding to Fe_3O_4 and increase of the Fe_2O_3 reflections as the activation time increases. After 2.5 h the iron catalyst has almost fully oxidized to iron (III) oxide.

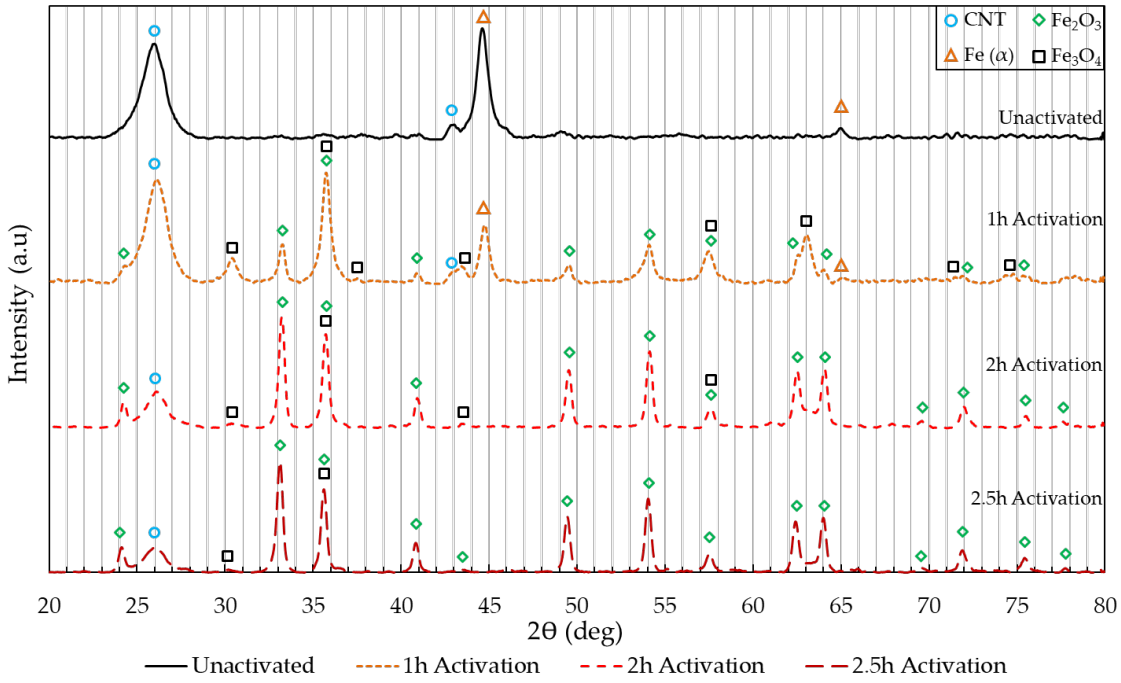

Figure 5. XRD diffraction pattern of unactivated, 1, 2, and 2.5 h activated CNTs and the resulting phase identification.

2. Electrical Resistivity Characterization

The resistivity of 0.014, 0.2, and 0.75 wt% in cured and uncured states with varying levels of activation can be seen in Figure 6. All data points referenced as uncured were measured from a viscous mixture consisting of the epoxy matrix with CNTs dispersed while cured data points come from a solid composite (hardener added to the first mixture and allowed to cure). These loadings were chosen as they span from before to after the percolation limit (which marks the change in conductive mechanisms) is reached [5]. Increased CNT loading resulted in decreased resistivity (increased electrical conductivity)

in all cases due to a more robust three-dimensional CNT network being present. Uncured composite mixtures exhibited resistivity higher than the cured composites by factors of 40, 114, and 36 in the 0.014, 0.2, and 0.75 wt% loadings, respectively. The 2.5 h activation of 0.014 wt% CNT mixtures resulted in resistivities that exceeded the ability of the test setup to measure accurately. Thermal activation resulted in decreased conductivity in both the uncured mixture and cured composite, the severity of which increased with activation time with a large jump occurring when activation was lengthened from 1 to 2 h.

One potential cause of this decrease in conductivity is the progressive oxidation of the iron catalyst discussed previously. Iron is traditionally considered a good conductor of electricity. Iron oxides, specifically magnetite (Fe_3O_4) and hematite (Fe_2O_3), demonstrate more semiconductor qualities depending on particle size and structure [126–130]. It then follows that the large amount of iron initially present (25.6 wt%) transitioning to magnetite (Fe_3O_4) and hematite (Fe_2O_3) is in part responsible for the increase in resistivity witnessed. The magnitude of which is uncertain without conducting further studies and considering other factors.

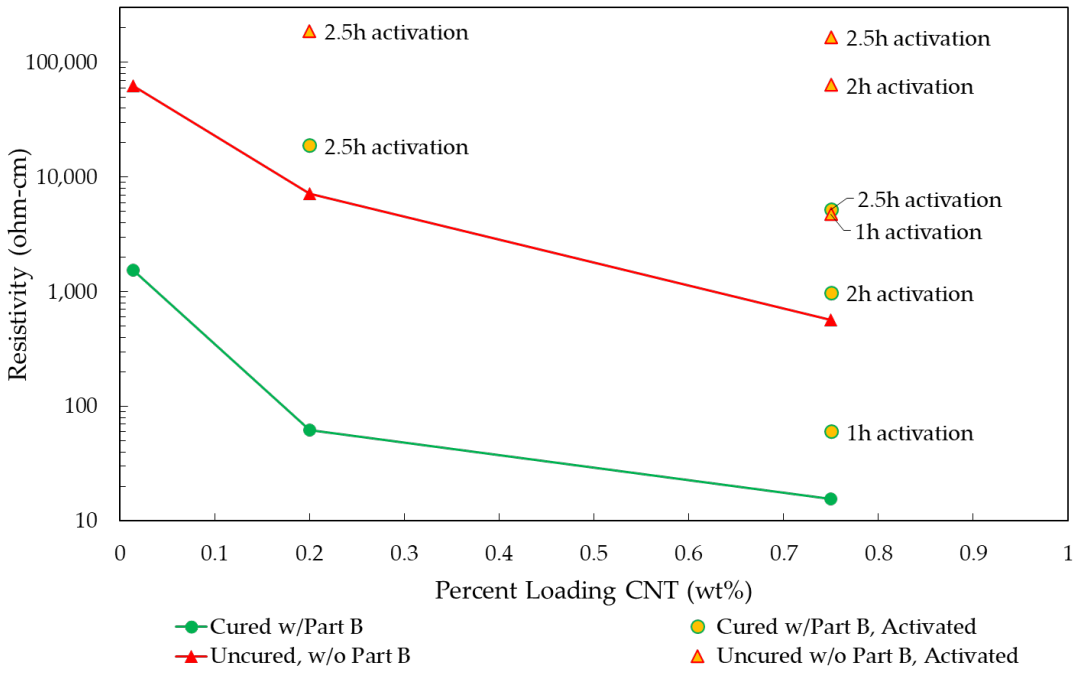

Figure 6. Resistivity of cured and uncured CNT consisting of unactivated and activated CNTs.

Raman analysis found in literature shows that the intensity of the D-band peak at approximately 1350 cm^{-1} increases as MWCNT structural integrity decreases (increased defects), or as the amount of amorphous carbon and impurities increase [131]. Here, it was hypothesized that a decrease in conductivity could be partially attributed to increased defects in the CNT crystalline structure caused by vacancies in the sp2 lattice sites and attached oxygen species from the thermal activation in an oxygen containing atmosphere. This behavior is documented in [118,119], where a study of thermal activation was found to initially reduce amorphous carbon, decreasing D-band intensity. The increased defect production associated with higher temperatures and longer exposure times eventually overshadowed any decrease driven by the reduction in amorphous carbon, resulting in an overall increase of the D-band peak.

Figure 7 presents the results of Raman spectroscopy of unactivated CNT pulp, and that activated for 1, 2, and 2.5 h. The D-band intensity was found to initially increase before decreasing significantly as activation time is increased past one hour. This decrease in the resulting I_D/I_G is indicative of improved CNT quality and a reduction of amorphous carbon — this differs from the overserved changes in peak behavior reported in the previously cited studies by Chen et al. and Mercier et. al. and may indicate that the CNT product used in this study contains larger concentrations of amorphous carbon.

Another possible explanation for the difference in D-band behavior when compared to other published work, is that the MWCNT used in this study feature larger aspect ratios and high agglomeration density. The latter is mainly attributed to the fabrication route, which produces intertwined CNT forming a mat, and is later broken into a pulp. As a result, the CNT pulp may experience non-uniform exposure to the activation conditions. The subsequent analysis did reveal D-band intensity varied by location within each individual sample—supporting this conclusion. However, because bulk CNT composite conductivity decreased as activation time increased, it is unlikely that changes to the nanometric structural integrity of individual tubes played an appreciable role in influencing resistivity in the finished composite. These large changes are likely the result of other factors analyzed in the coming paragraphs.

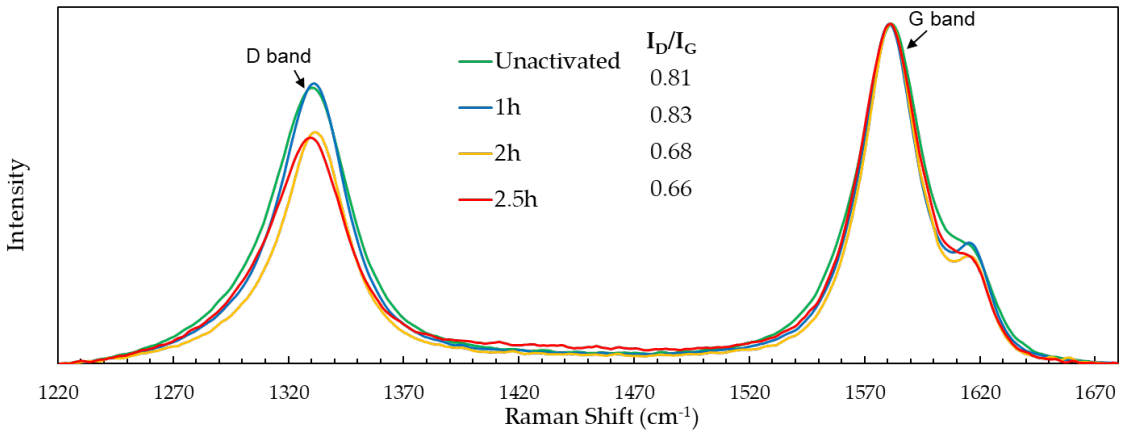

Figure 7. Raman spectroscopy of the D and G-band of unactivated and thermally activated CNT pulp.

Figure 8 presents optical microscopy of finished (cured) nanocomposites produced from CNT that were subjected to varying activation times. It is important to note that samples were fabricated from distinct batches of CNT pulp that were activated for different activation times. The network was imaged in four random locations for each sample. The figure is best observed left to right with the understanding that activation time increases in this direction. An effort was made to keep the focus plane near the middle of the film.

Initially, a robust CNT network consisting of thick intertwined CNT bundles exists with the bundle lengths spanning most of the field of view, 143 µm wide. Because these structures are not straight and the strands curve through the captured frame, the actual length is assumed to be > 143 µm in many locations for both the unactivated and 1 h activated samples. As activation time is increased, a distinct breakdown in the CNT bundle length, bundle diameter, and level of entanglement was observed. Differences between unactivated and 1 h activation times, while discernable, were the least severe, with bundle thickness and length largely intact. Samples fabricated from 2 h activated CNT exhibit a more obvious reduction in bundle thickness and bundle length dropped below 100 µm. Lastly, specimens made with 2.5 h activated pulp show the largest disparity between all the samples with CNT bundle length appearing both more homogenous and significantly shorter, with lengths in the range of 10–30 µm. Structural damage to CNT under similar conditions was documented in [118] through TEM imaging. This compromise to the

integrity of the CNT itself, with the shear strains of the dispersion process, are the presumed cause of the observed decreases in CNT bundle length.

Past research indicates that the tridimensional CNT network, including the aspect ratio of CNTs, plays a significant role in the conductivity of the resulting composite [63,66,132]. That behavior is consistent with percolation theory that was discussed previously in Chapter II.B.1.c. This observed breakdown of the CNT network, to include the length of CNT bundles associated reduction in aspect ratio, is likely a major contributor to the measured increases in resistivity previously discussed.

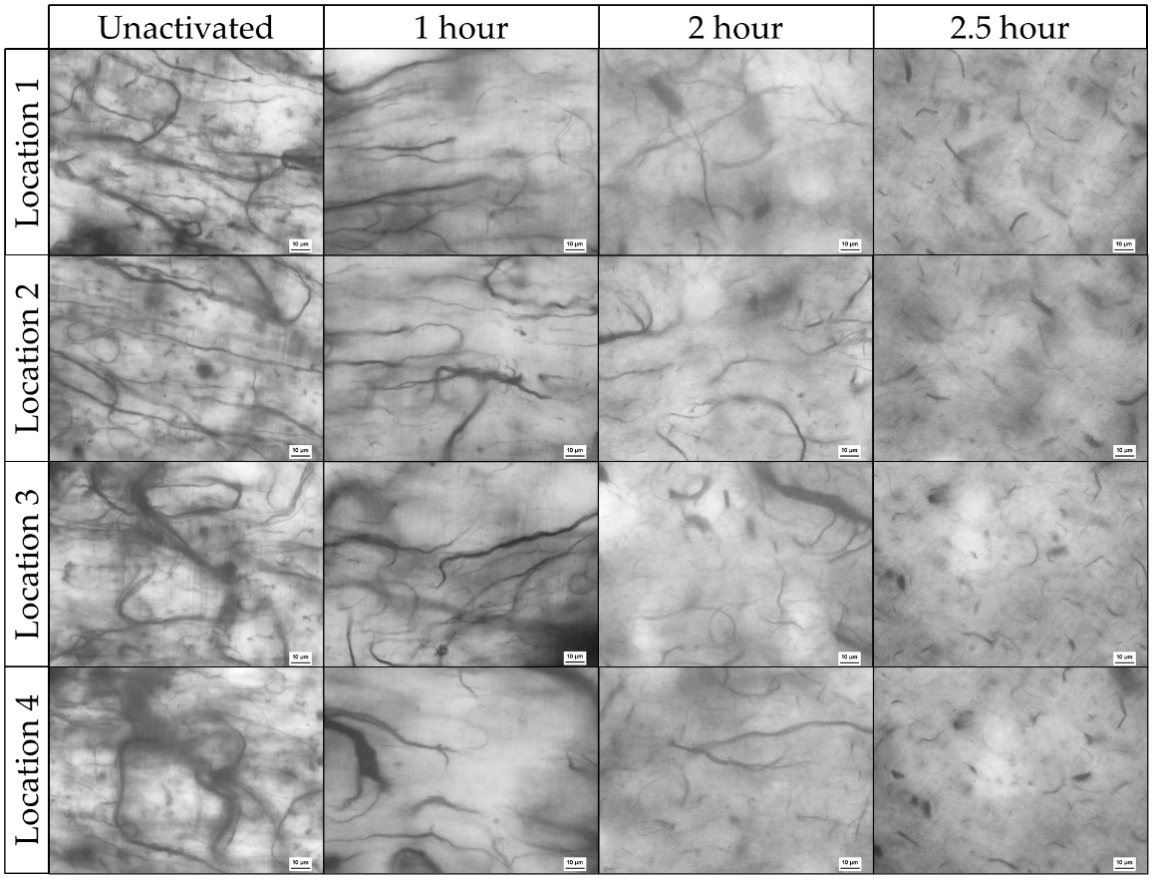

Note: scale bar is 10 µm, individual panel widths are 143 µm.

Figure 8. Optical microscopy from four locations in unactivated, 1, 2, and 2.5 h activated CNT pulp.

The electrical resistivity measurements obtained in this study by varying activation duration were compared with two datasets obtained in previous studies, (1) varying the number of cycles in the mixing protocol and, (2) utilizing 3 mm silica beads to aid dispersion. Figure 9 presents the 0.75 wt% CNT composite electrical resistivity derived here (Figure 9a) alongside the two datasets adapted from [5] (Figure 9b,c). The silica beads were added prior to the mixing process and strained out of the mixture prior to curing (prior to cycle 1, and after cycle 5 in Table 4) to aid dispersion of the CNT pulp. These beads introduce shear forces that have the effect of increasing dispersion and decreasing bundle size by impact and attrition—essentially functioning as grinding media within the asymmetric mixture. This breakdown of the interconnected CNT network leads to an increase in the resistivity of the composite. Similarly, mixing (without beads) initially improves conductivity through the dispersion of the CNT filler, however, past a certain threshold the resistivity increases as the CNT pulp is over-mixed. While 0.75 wt% CNT loading was analyzed here, note that these effects differ (less severe) at loadings below the percolation limit, e.g., 0.014%. In sum, electrical resistivity depends on the connectedness of the CNT network for a percolation path, past a certain level of dispersion, further homogeneity can result in a reduction of electrical conductivity. For a more in-depth discussion on percolation theory and these mechanisms, the reader is directed to [5].

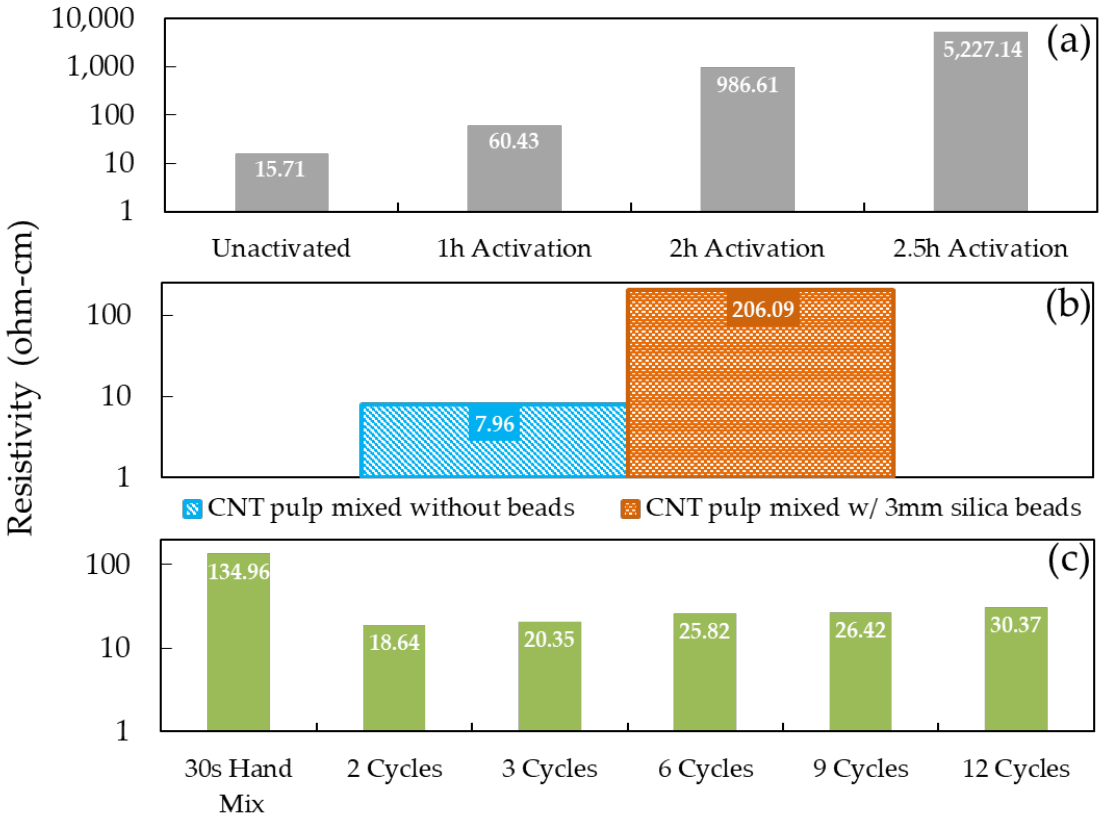

Figure 9. Comparison of 0.75 wt% CNT cured composite resistivities when, a) activation time is varied, b) silica beads are used in the mixing process to encourage separation of tube bundles, and c) the number of mixing cycles is varied.

The magnitude of the effects observed in previous studies, i.e., the use of beads and varying mixing cycles, is significantly smaller than those seen to result from thermal activation (this study). Over-mixing through additional dispersion cycles results in a ~2x increase in resistivity, while bead mixing has a more meaningful impact of 1–2 orders of magnitude. Activation changes result in 2–3 orders of magnitude difference. This suggests that the differences are likely the result of an amalgamation of the changes documented thus far, e.g., of phase changes associated with the remaining iron catalyst oxidation, a decreased interconnected CNT network, and reduced aspect ratio of the CNT pulp, and potentially increased dispersion resulting from surface functionalization.

3. Viscosity Characterization

Notable differences in the viscosity of activated CNT/Epoxy mixtures are observed when working with unactivated and activated CNTs within the studied loading (% of CNT) regime. Activated samples tend to agglomerate less and have a more consistent texture, often leading to greater ease of application onto surfaces for thin-film samples production. Indicative of this is the post-cured appearance of ~0.19 mm thin-film samples shown in Figure 10. The finished texture, more specifically the surface profile of the cured composite, changes drastically based on activation level. The unactivated CNT film appears distinctly as a sample with varied heights with activated samples reducing this effect and eventually curing as a smooth surface in the case of 2.5 h activation. When interpreted in conjunction with the breakdown of CNT bundles seen in optical microscopy presented in Figure 8, we speculate that the inconsistencies in profile height are the result of larger agglomerations causing raised areas in the composite. That is, areas higher in profile height are likely dense regions of CNTs. As the CNT bundle length and thickness decreases, as discussed in relation to Figure 8, this effect decreases, and results in smoother texture when cured as a film.

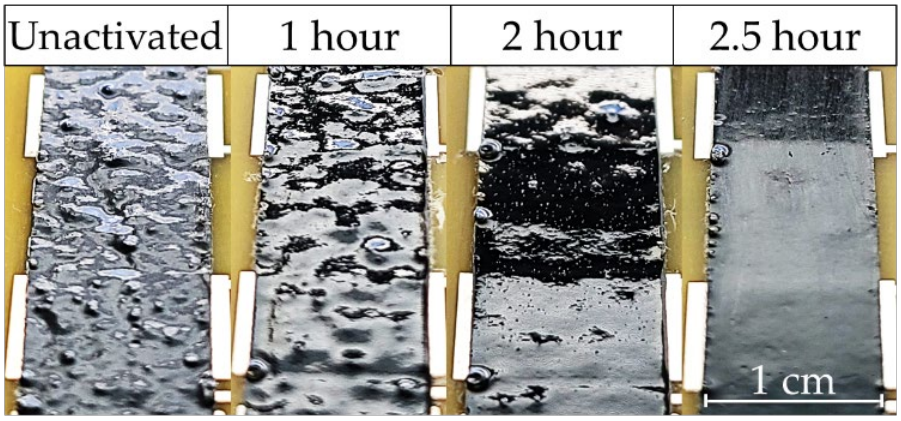

Figure 10. Close-up view of cured epoxy fabricated with CNTs under various levels of activation.

Figure 11 presents the viscosity measurements obtained from nine unique samples. At low strains, increased CNT loading percentage results in increased viscosity. In all

cases, viscosity decreases with increasing strain. Above ~40% strain a distinct change in slope occurs as the samples converge to similar viscosities. Prior to this point, higher CNT loadings produce steeper decreases in viscosity as strain increases. The behavior is consistent with the findings of Rahatekar et al., where through optical analysis and comparable viscosimeter geometry, viscosity at low shear strain rates was found to increase with MWCNT loading and shear thinning behavior was correlated to the breakdown of CNT bundle agglomeration [133]. The convergence of all samples to a similar point indicates that a breakdown of the agglomerations has occurred and past this ~40% strain, viscosity is dominated by the properties of the base epoxy.

Of the nine samples, one exhibits behavior inconsistent with the rest. At low strains, the 0.2 wt% CNT sample presents viscosity consistent with what is to be expected, i.e., greater than the 0.014% loadings and less than the 0.75% loadings. However, it decreases more rapidly as strain increases and does not converge to the same point as the rest. The consistency in the behavior of the rest of the samples leads the authors to speculate that other factors may be at play. The raw CNT pulp is sometimes very tightly agglomerated. If the required loading featured more of these regions than normal, it is possible the resulting dispersion was inconsistent with other samples. Differences in environmental run conditions of the viscosimeter could also lead to differences in behavior. Further testing and analysis of the sample in question would need to be performed to confirm the mechanism for such discrepancy.

Thermal activation had the effect of decreasing the viscosity of the mixture compared to its unactivated counterpart at all strains. The only exception was the outlier already discussed (general trend still held true at low strains). The 0.014 wt% mixtures display a slightly higher viscosity than the base epoxy but, after thermal activation, drops to a level near pure EA9396. At 0.75% loadings, thermal activations effect on decreasing viscosity is also seen which the most dramatic fall coming at 2.5 h activation time. Large differences in the slope at which viscosity decreases are seen for the two loadings. The differences in this initial slope are attributed to large differences in the microstructure. At 0.014%, below the percolation limit, the connectedness of the CNT network is sparse, with CNT bundle interaction having a limited effect on both the initial viscosity on the mixture

and resulting in weak dependence on strain. At 0.75%, a robust interconnect network of CNT bundles exists, viscosity at low strains increases dramatically and increasing strain results in larger reductions in viscosity as shear forces separate agglomerates and interactions between CNT bundles.

The effects of CNT functionalization with oxygen species and its impact on viscosity may need further study and have been targeted for future work. The vast differences in the size of the CNT pulp seen in Figure 8 make it difficult to decouple the viscosity effects of shorter CNT bundles from any improvements that functionalization caused through improved matrix interaction. However, the combined result of thermal activation is a significant decrease in mixture viscosity across all loadings.

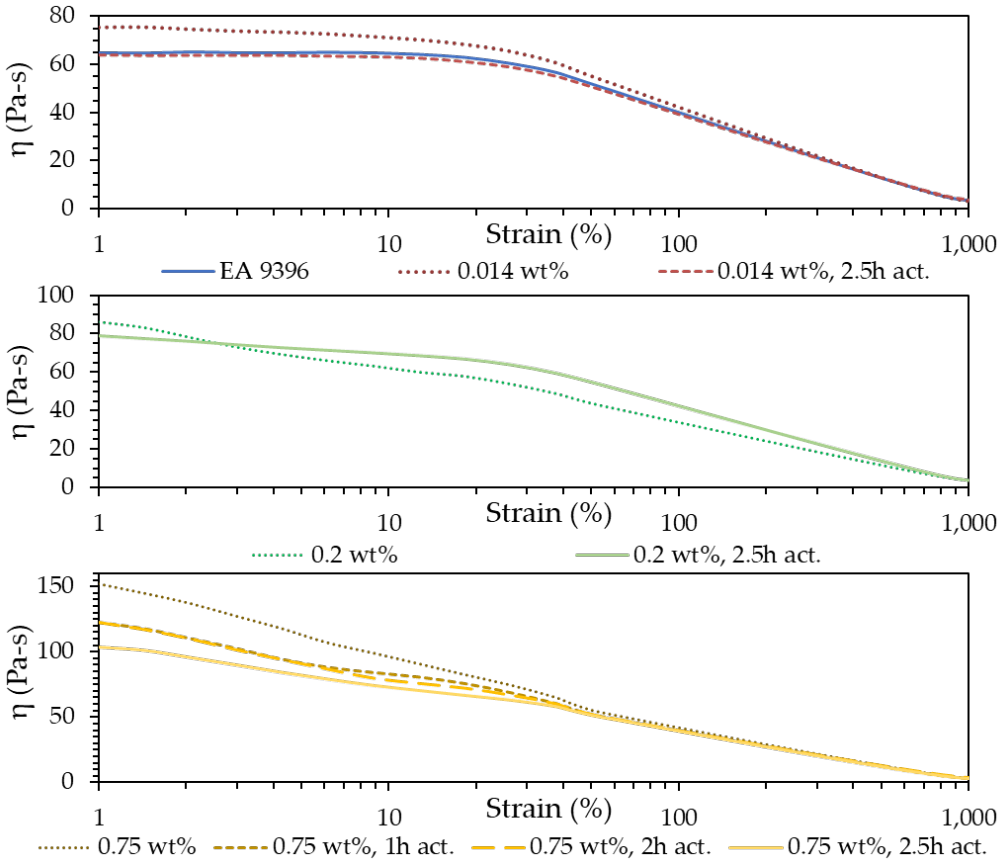

Figure 11. Measured viscosity as a function of strain for 0.014, 0.02, and 0.75 wt% CNT loadings with different activation times.

These results involving the electrical resistivity of uncured epoxy–CNT mixtures and cured epoxy–CNT nanocomposites suggest a predictable relationship between the electrical performance in uncured and cured states at all levels of thermal activation. Rheological measurements also found notable trends within each CNT wt% loading regime where both thermal activation duration and decreased CNT loading result in measurable decreases in viscosity at lower strains. This points to an opportunity to identify poor dispersion, loading, or subpar electrical performance of a resulting nanocomposite through in-line quality control—something readily employed by many industries. Electrical resistivity has been identified for use in the concrete industry for testing mixtures' resistance to chloride permeability and the associated corrosion of mechanical reinforcements [134,135]. Even more widespread, many industries utilize viscosity as a metric to ensure the quality of the resulting product. The food industry utilizes viscosity to guarantee texture and batch-to-batch consistency [136]. Pharmaceutical manufacturers utilize viscosimeters at regular checkpoints to safeguard solutions, emulsions, and suspensions critical to drug delivery [137,138]. Similarly, coatings and lubricants are subjected to viscosity standards to ensure the proper application method is chosen and desired thickness is achieved [139–141], or lubricating protection is maintained [142–144]. Findings such as the ones presented in this manuscript make the development of similar techniques utilizing epoxy–CNT mixture conceivable.

D. CONCLUSIONS

The data collected here indicate that thermal activation has significant impacts on the electrical and rheological performance of CNT–epoxy mixtures both in production and after curing. Thermal activation of CNT pulp increases resistivity by 2–3 orders of magnitude in both uncured and cured CNT–epoxy composites. These effects were documented across loading regimes. The resistivity of uncured mixtures mirrored the behavior of cured CNT composites, suggesting that absent other defects in the production process the performance of the uncured mixture could be an indicator of finished composite performance. The thermal activation of CNT pulp also dramatically affected the uncured mixtures' viscosity. Viscosity was found to increase with increasing CNT loading and be

inversely dependent on activation time. At high strains, the mixtures viscosity approximates that of the base epoxy.

These findings expand upon the existing body of knowledge already available and demonstrate that there are verified trends within CNT loading regimes as activation time is varied. Additionally, they show the potential for precured viscosity and mixture resistivity as an indicator of the behavior and properties of the corresponding cured composite. When taken together this data has demonstratable value to industry, namely in the form of understanding how the effects of thermal activation, as a functionalization technique, change dispersed CNT mixtures and the corresponding composite performance. As commercialization grows this data can facilitate inspection and validation efforts of CNT–polymer composites at a stage of production that would still allow for remediation.

III. ULTRASONIC TESTING

A. BACKGROUND AND THEORY

Conventional NDE techniques vary widely by the application and industry. Simple visual inspections can be successfully employed on products deemed to have low-risk applications while more stringent industries looking to satisfy regulatory requirements, whereas pressure vessels in the nuclear industry, can require radiographic testing. Somewhere between these extremes is ultrasonic testing (UT), where it is one of the most common and extensively employed in shipbuilding [145] and aerospace [146] industries where it is used on composite structures, including carbon-fiber reinforced polymers (CFRP) [147,148]. Inspections conducted on these materials utilize frequencies on ~5-10 MHz with devices that are often handheld or employed in automated, in-line quality assurance mechanisms for composite materials [149,150], However, these frequencies result in resolutions of several hundred microns [151].Higher resolutions with more advanced acoustic techniques exist and have been utilized to image GNP and MWCNT composites [152,153]. One such technique, referred to by Levin et. Al. as the "acoustic analog of the dark-field light microscopy," has been utilized to achieve resolutions in the 10s of μm [154]. This technique also has the potential for 1–2 um resolution with increased operating frequencies in the GHz range [151]. However, impulse acoustic microscopy requires sophisticate equipment, thin samples, and features fields of view similar to SEM.

As a result of these limitations, a study to explore the usefulness of conventional frequency UT on MWCNT composites was conducted. Should longitudinal velocity, or porosity, prove useful in evaluation of CNT composites, and this study demonstrate feasible measurement of these properties via conventional operating frequencies, there is potential value in this method. Herein, a predominately binary pass/pass/failure (flaw detected/no flaw detected) analyses is conducted with UT device. Four defect types, a) concentrated CNTs alternated with areas devoid of those, b) glass beads, c) copper wire, and holes, were introduced to simulate four different cases. The first, concentrated CNTs would simulate a poorly dispersed pulp, the interface here were represent the worst-case scenario the acoustic wave traveling from an area of 0% CNT to that of extreme

concentration. Next, glass beads, are another analogue to an area devoid of CNTs but with the known acoustic properties of the borosilicate glass. Secondly, a copper wire could simulate metallic contamination or the surface the epoxy adhesive is applied on. This would validate the use of UT for film thickness measurements. Lastly, holes were used to simulate an area of excess porosity.

Ultrasonic testing utilizes artificially produced acoustic waves to collected data probe materials collected data probe materials. A transducer transmits the ultrasonic waves into the surface of the target material the incident wave propagates through the first material until it encounters a defect. Figure 12 illustrates this concept and defines several characteristic equations. The term acoustic impedance, Z, characterizes how readily a material transmits an acoustic wave and is a function of material density and longitudinal velocity. If the wave travels through the subject material and encounters a defect, in this case, glass beads, copper, or air, a portion of the incident wave is reflected to the transducer and a remaining amount continues being transmitted past this boundary. The sum of the transmitted and reflect signals is equal to the initial incident wave. The strength of the return is dictated by the acoustic mismatch of the two mediums. Equation (3) of Figure 12 defines the reflection coefficient that is a measure of this mismatch. A higher reflection coefficient correlates with a more acoustically dissimilar material and thus a larger reflection. It then follows that probability of detection is increased.

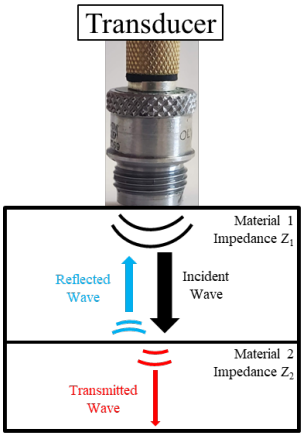

(1) $I = R + T$

(2) $Z = \rho V_L$

I = Incident Signal
R = Reflected signal
T = Transmitted signal

Z = Acoustic Impedance
V_L = Longitudinal Velocity
ρ = Material Density

(3) $R_c = [(Z_2 - Z_1) / (Z_2 + Z_1)]^2$

R_c = Reflection Coefficient
Z_1 = Acoustic Impedance of 1st material
Z_2 = Acoustic Impedance of 2nd Material

Figure 12. Depiction of ultrasound traveling through two mediums and governing equations. Adapted from [155,156].

For the three defect materials chosen the acoustic impedance and reflection coefficient were calculated in Table 5. The reflection coefficients of the materials would indicate that the glass beads would be most difficult to detect, followed by copper, and air (holes).

Table 5. Acoustic properties of samples (average) and introduced defects.

Material	**V_L** Longitudinal Velocity [m/s]	**ρ** Density [kg/m^3]	**Z** Acoustic Impedance [kg/m^2s]	**R_c** Reflection Coefficient $[(Z_2 - Z_1) / (Z_2 + Z_1)]^2$
EA9396 w/CNT	2883	1115	3214710	-
Glass Bead	5540	2230	12398800	0.3460
Copper	5010	8960	44889600	0.7506
Air	343	1.204	399	0.9995

Note: EA 9396 w/CNT V_L and ρ an average of values measured across all loadings. Other material properties were obtained from: [157]

B. EXPERIMENTAL METHODS

1. Samples

Five samples were created for this study. Pure EA9396, without CNT loading, produced at two different curing temperatures, and 0.014%, 0.2%, and 0.75 wt% CNT loadings. Samples were created via the CNT dispersion and curing method specified in Section V.B.1 with two deviations. First, the room temperature (RT) cured sample was cured at room temperature (25 °C for 3–5 days). The second deviation is that prior to curing, the defects were introduced to the sample piece while in the mold and then placed in the oven. Sample thickness varied from approximately ~ 5–25 mm for 25 °C, accelerated (66 °C) cure, and the 0.014 wt% CNT samples. For 0.2 and 0.75 wt%, CNT sample thickness varied from 6–8 mm due to increased porosity issues resulting from increased thickness and CNT loading discussed later in the results section.

Artificial defects were introduced to determine if ultrasonic testing could identify their presence. A control was created out of 25 °C cured and 66 °C cured EA 9396 (w/o

CNTs). Three defect mediums, intentionally concentrated CNTs, glass beads, copper wire, and air (holes), were chosen for their differing acoustic properties and feasibility for producing different size defects. A contact transducer was then used on the sample to search for the artificial flaw.

2. Density Determination

An Ohaus PA224 Analytical balance with density determination kit was utilized to measure the density of Nanocomposites with various wt% CNT loading. The kit is pictured in Figure 13. Determining sample density requires two mass measurements, one in air, and a second while fully submerged. With this data and temperature-adjusted densities of water and air, the density can then be computed via the equation in Figure 13.

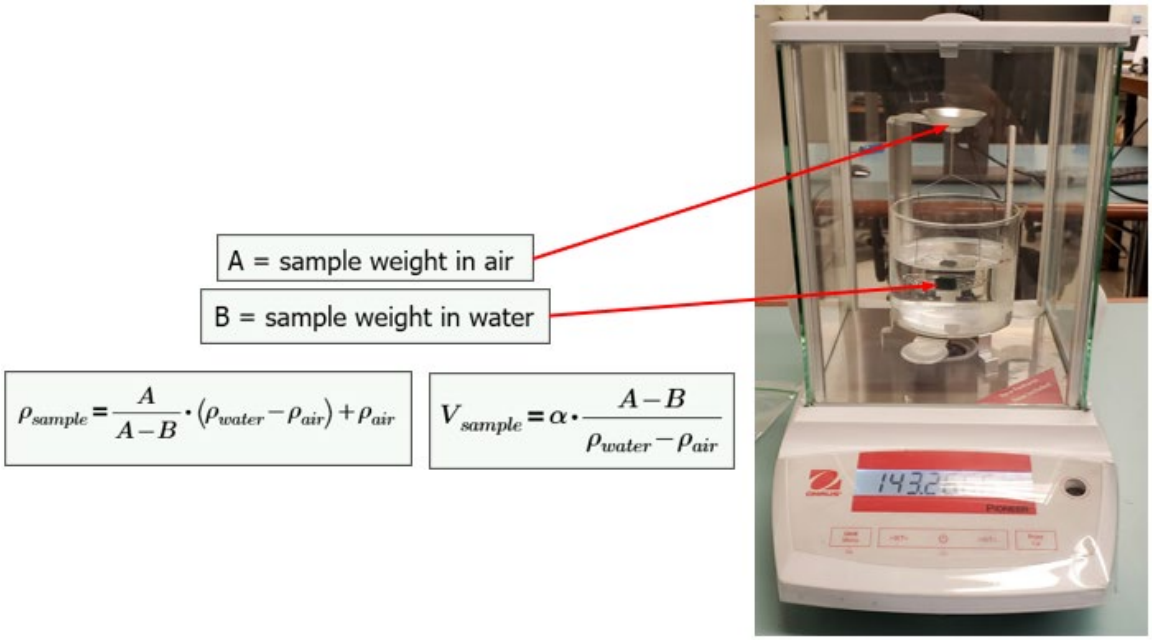

Figure 13. Ohaus PA 224 Analytical balance with density determination kit and equation for determining sample density.

3. UT Testing

Ultrasonic Flaw detection was done using an Olympus EPOCH 650 (Figure 14). The detector is capable of 2–10 kHz A-scans. This was paired with a 0.25” diameter

A543S-SM contact transducer with a 5 MHz operating frequency (Figure 14). The device was calibrated on a sample of known thickness using the manufacturer-provided protocol prior to any measurements being taken.

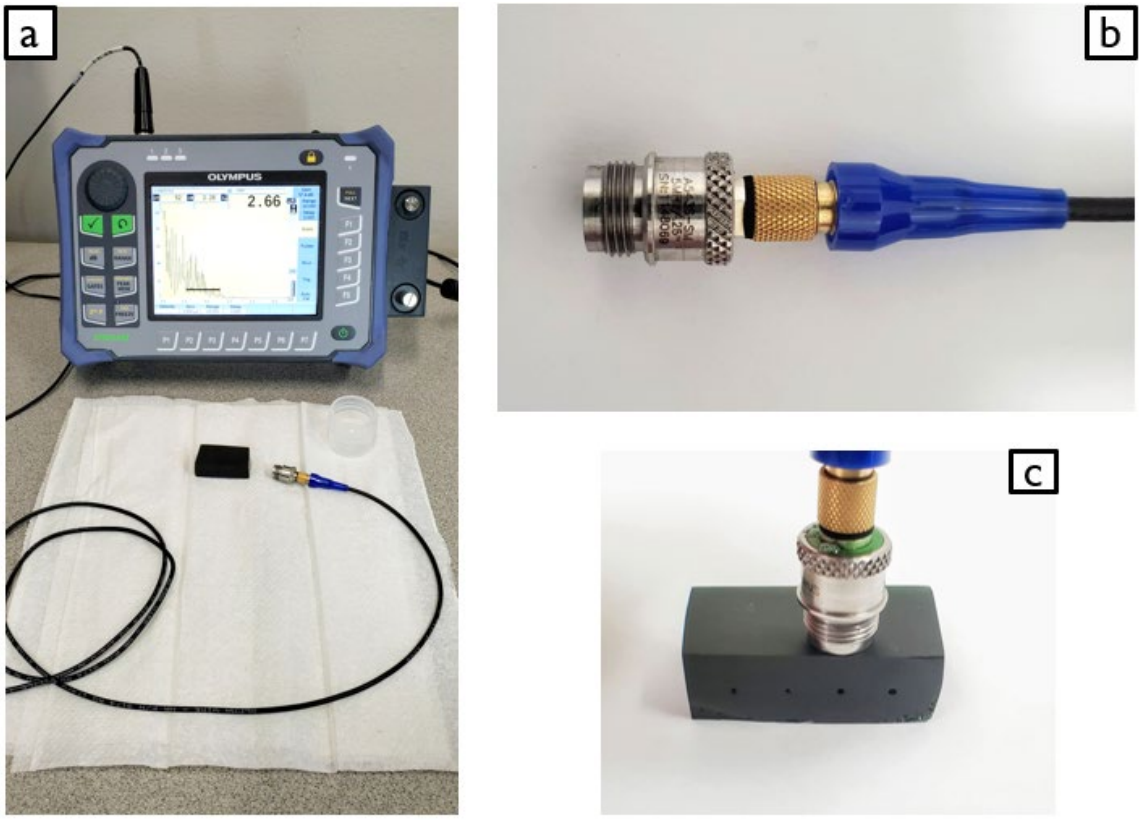

Figure 14. a) Olympus EPOCH 650 Ultrasonic Flaw detector, b) A543S-SM transducer and c) example transducer/sample configuration for flaw detection.

The transducer is used in conjunction with a coupling medium, here vegetable glycerin was used. Placing the transducer against the sample piece and monitoring for signal peak allows for measurement of the time-of-flight, i.e., the time it takes a sound wave to travel from the transducer through the sample and back. When done with a sample of known thickness, the characteristic longitudinal velocity can be backed out. This concept and the equation used are illustrated in Figure 15. Determination of the longitudinal velocity was made from series of ten measurements on each sample.

(1) $V_L = 2x/t$

V_L = longitudinal velocity
x = known sample thickness
t = time of flight

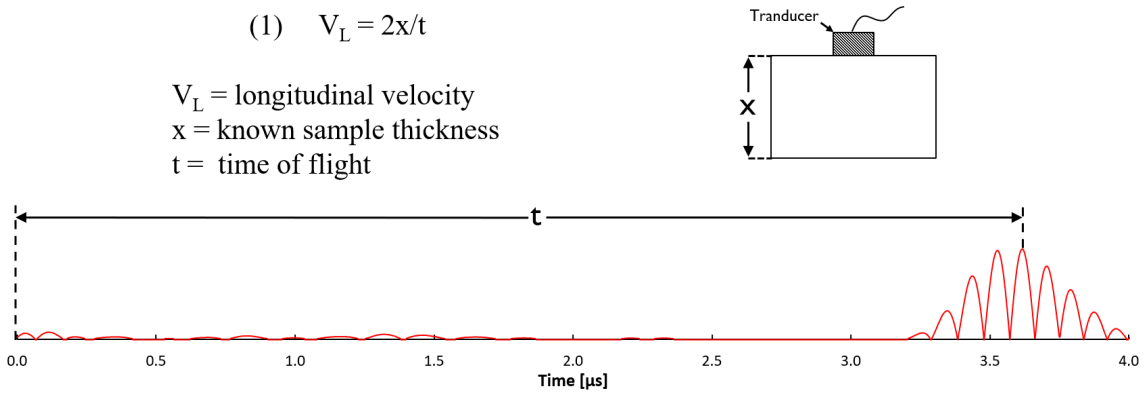

Figure 15. Example signal from the UT system and governing equation for determining longitudinal velocity on a sample of known thickness.

Steel samples of a known thickness (Figure 16) were also tested to ensure proper device operation and for potential comparison of signal quality. The peak moves right indicating a longer time-of-flight (correlating to thicker sample) and decreased amplitude resulting from more attenuation caused by the increased travel distance.

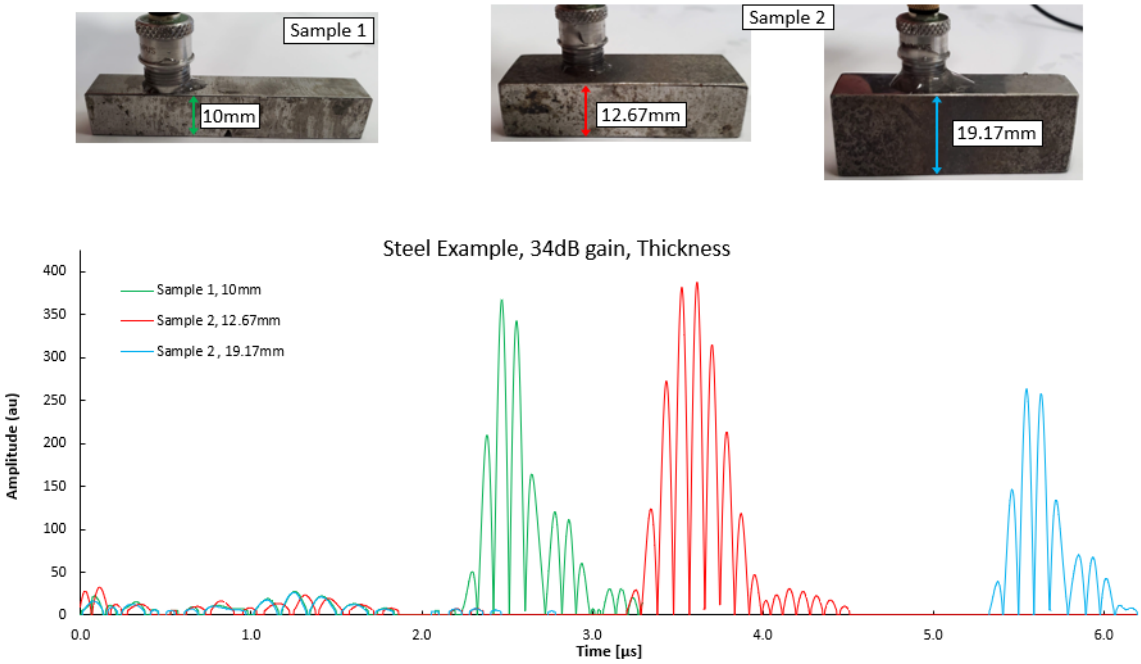

Figure 16. Example ultrasonic signal from three different steel samples. Peaks represent back surface and correspond to the thickness of the sample.

C. RESULTS

The density effects of CNT loadings had not been characterized before this study. Unpublished studies, conducted internal to the research group, have that different curing temperatures produce differences in porosity. Namely, when comparing 25 °C curing and 66 °C cure temperatures, a marked decrease porosity has been documented in those cured at the elevated temperature. Additionally, macroscopic qualitative assessment of samples featuring various CNT loading have resulted in the determination that increased CNT loading results in increased porosity. Acoustic properties, namely longitudinal velocity, exhibit a density dependence that is well documented for many other epoxy resins and plastics. These assessments give context and support the findings from density and acoustic property measurements presented below

1. Density

The results of density and longitudinal velocity testing are presented together in Table 6. The 25 °C cured sample, while partially transparent, is cloudy and more opaque than the transparent, fast-cured sample under background illumination. Optical microscopy reveals that this is caused by the 25 °C curing process resulting in increased numbers of microscopic bubbles than the faster-cured sample which while porous, develops larger bubbles more sparsely dispersed. The measured density correlates well with the porosity differences between the curing methodologies discussed earlier

Table 6. Measured longitudinal velocity and density of various samples.

Material	Longitudinal Velocity [cm/µs]	Measured Density [g/cm^3]
EA9396 w/ 0.75%wt CNT	0.273	0.9950
EA9396 w/ 0.2%wt CNT	0.282	1.0492
EA9396 w/ 0.014%wt CNT	0.291	1.1766
EA9396 (25 °C Cure)	0.293	1.1771
EA9396 (66 °C Cure)	0.302	1.1782

Increasing CNT loading results in drastic changes in the uncured mixture's viscosity. Comparing the viscosity of pre-cured 0.75 wt% CNT epoxy to 0.014 wt% CNT epoxy is analogous to comparing honey to water. To minimize air bubbles, any entrained air must escape prior to the epoxy curing or the sample suffers from increased porosity. Higher viscosity means a more tortuous escape path for entrained air. Maintaining a vacuum during the mixing process mitigates these effects to some degree by aiding in air removal. However, it still poses a significant issue, and particular caution must be taken to ensure sample quality remains as consistent as possible batch-to-batch. However, some of this is unavoidable and explains this inverse relationship between sample density and CNT loading.

A source of error was discovered during this analysis. Due to the porosity of the samples, void spaces cross-sectioned during sample preparation create a textured surface for air to attach to. Agitation of the sample and scraping with a brush only able to remove the largest bubbles, leaving some attached to the sample and creating artificial buoyancy. This results in the samples with higher CNT loading having a density that is lower than reality. Improvements in measurements could be made through the employment of a gas pycnometer.

2. Longitudinal Velocity

Ten measurements were taken for each sample to determine the speed of sound in the media/material employed. The thicknesses of each location are tabulated in Table 7. Differences in thickness of higher loadings, 0.2% and above, are of note. The increased porosity of higher-loaded CNT samples, 0.2% and 0.75%, resulted in a weaker ultrasonic signal, likely attributed to an increased density of air bubbles (mechanism discussed later). To properly determine the longitudinal velocity in these samples, the thickness was reduced to ensure signal fidelity and an accurate measurement.

Table 7. Thicknesses of the locations used to determine longitudinal velocity for each sample.

Location	25°C Cure	66°C Cure	0.014 wt%	0.2 wt%	0.75 wt%
1	6.20	12.8	11.0	6.19	6.26
2	5.60	11.3	10.6	6.20	6.05
3	5.80	11.4	10.5	8.99	6.30
4	10.8	11.5	10.2	9.01	6.03
5	12.5	11.6	9.60	6.36	6.29
6	11.7	9.10	11.3	6.24	6.12
7	11.5	10.8	11.1	6.18	5.88
8	13.1	10.3	7.60	6.22	5.76
9	7.30	7.10	7.40	6.15	5.85
10	25.1	6.40	24.9	6.38	5.94
Average Thickness	11.0	10.2	11.4	6.79	6.05

The calculated longitudinal velocity is presented alongside density in Table 6 and graphically with standard deviation in Figure 17. In general, decreasing longitudinal velocity is observed with increased carbon nanotube loading. Similarly, this trend is seen when comparing the 66°C cured and 25°C cured samples.

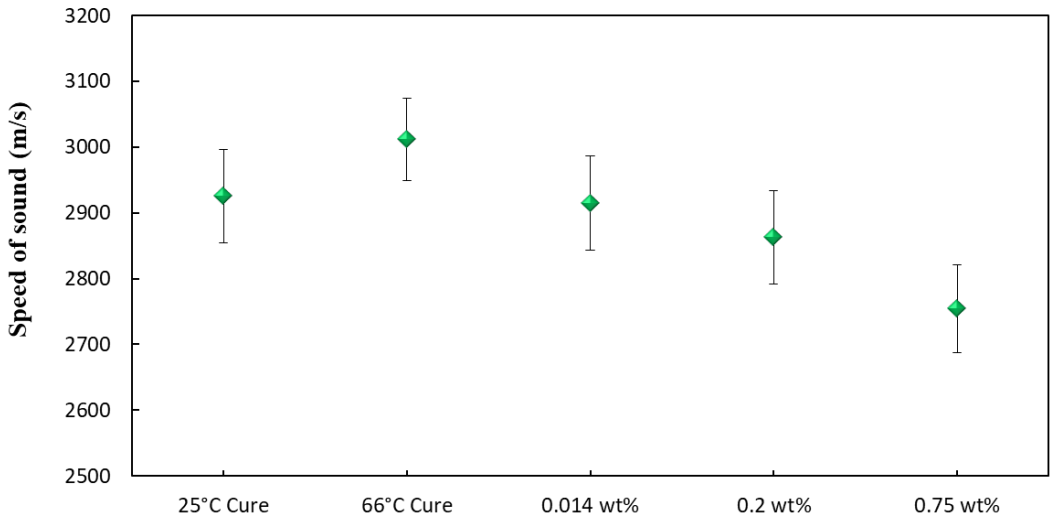

Figure 17. Longitudinal velocity over different samples. 25 and 66°C samples are pure EA 9396 w/o CNT.

For reasons discussed earlier and verified through optical analysis and density determination, increased CNT loading results in larger porosity. For larger-scale composites, e.g., carbon fiber reinforced polymers (CFRP), many groups have concluded decreased longitudinal [147,158,159] velocity result as void density increases. This is attributed to the fact that the empty voids are excellent scatterers of ultrasonic waves. For this reason longitudinal speed and has even been proposed as a standalone NDE metric for porosity [148]. In [158], it was concluded that fiber content had little effect on longitudinal velocity. Carbon nanotubes are several orders of magnitude smaller than conventional carbon fiber, and concomitantly far smaller than the acoustic wavelengths used in this ultrasonic testing. Like the optical limits of microscopy being limited by the visible spectrum, ultrasonic inspection wavelengths vastly larger than interior features result in the material behaving like a continuous solid. Here, the transducer frequency of 5 MHz, equates to roughly a 0.6mm wavelength. With CNTs orders of magnitude smaller, and existing studies finding much larger carbon fiber has limited impact on V_L, it's a reasonable to conclude that CNT have a minimal impact on longitudinal velocity directly. Rather, it is likely that viscosity increases due to additional CNT loading, and the associated porosity, are responsible for the measured decrease in longitudinal velocity.

Figure 18 compares CNT composite samples to common plastics, resins, and phenolics already in wide-spread use. The measured density is expected to be lower than the actual value due to small air bubbles remaining on the sample during the measurement process. Every effort was made to minimize this effect but tiny, microscopic bubbles. This was particularly obvious on 0.2 wt% and 0.75 wt% CNTs samples where surface pores were most prominent.

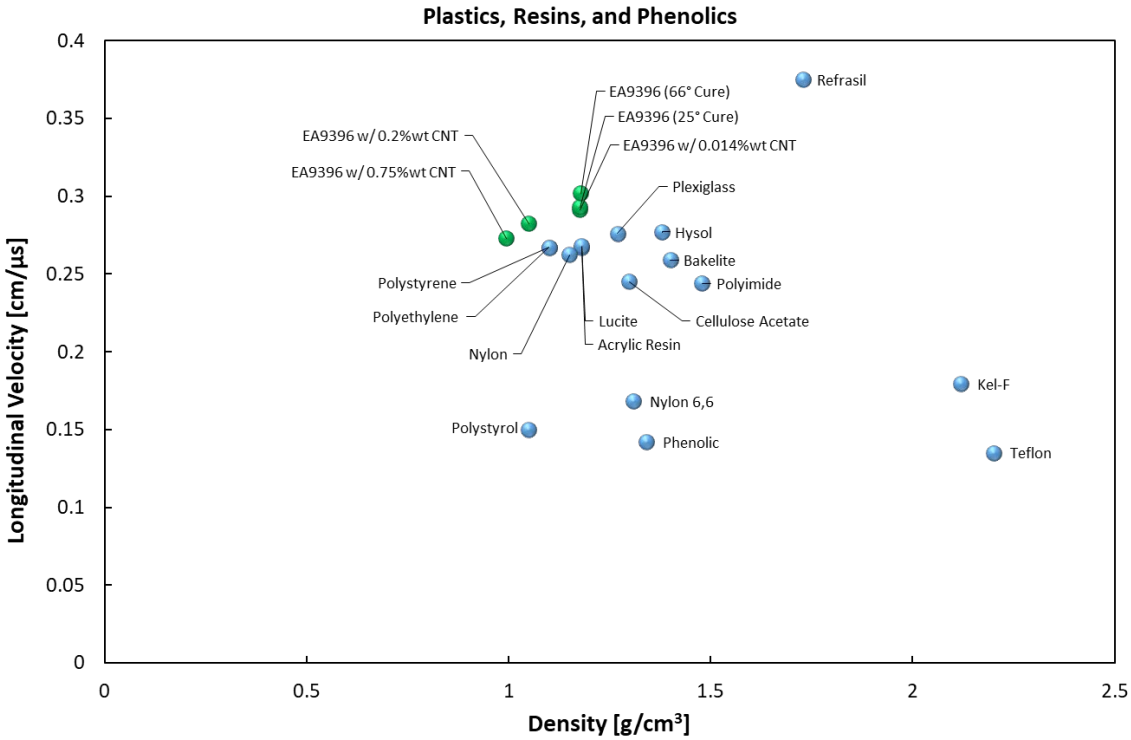

Figure 18. Speed of sound vs. density for common plastics, resins, and phenolics. Adapted from [160].

3. Flaw Detection

a. Concentrated CNTs

A concentrated CNT epoxy mixture was inserted into a bare EA 9396 by layering the CNT mixture with bare EA 9396 in the mold prior to curing. The concentrated portion was ~ 5% CNT by weight representing 1–3 orders of magnitude change over typical formulations. The sample and results of the ultrasonic testing are shown in Figure 19. The agglomeration of CNT bundles was unable to be detected. Slight differences from the baseline signal were seen, most notably the reduced amplitude of the background peak however objectively there is not a significant defect peak. Other areas were tried and resulted in similar results.

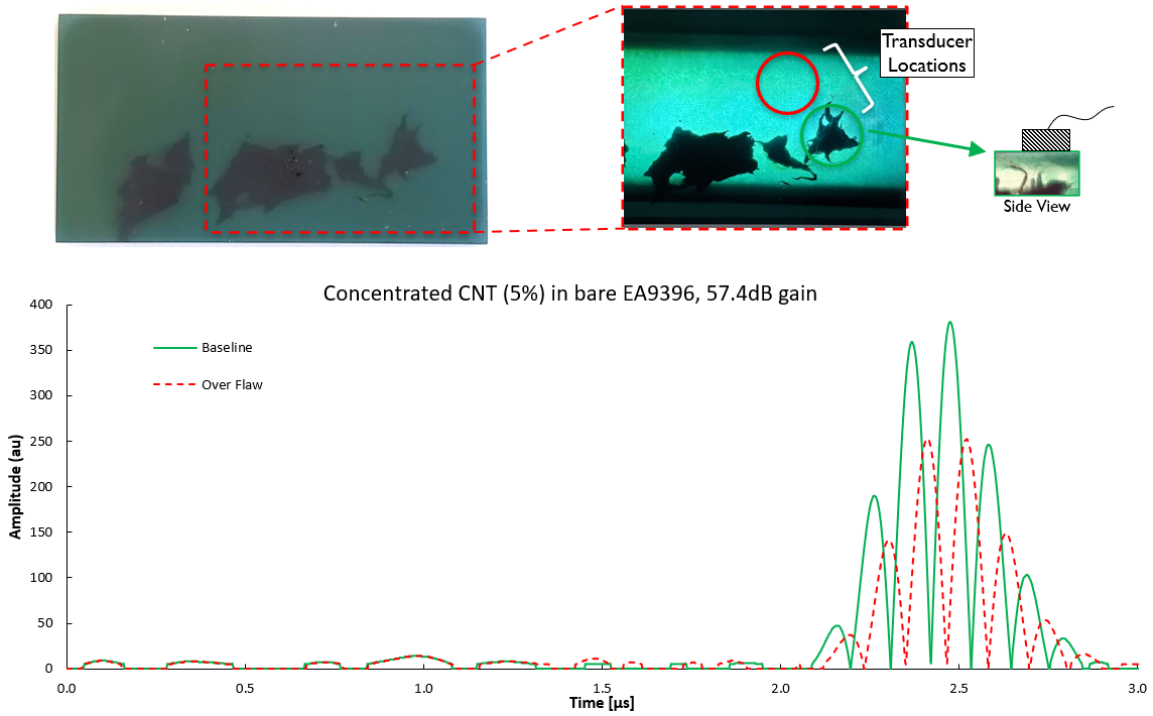

Figure 19. Top: pure EA9396 sample with concentrated CNT areas and transducer locations identified. Bottom: signals from two different transducer locations.

b. Glass Beads

Fast cured, 66° C, EA9396 and 0.014% CNT EA9396 were the samples chosen for insertion of ~ 2–3 mm glass bead defects. The samples with lowest porosity were used to make detection most likely. Figure 20 and Figure 21 show the samples used, the transducer locations, and a color matched graph with the baseline measurement and signal while over the defect. Comparing signatures between samples reveals the effect of porosity on scattering of the ultrasonic wave. While both signals were obtained with the same gain value of 37.4 dB, the 0.014% results in a much noisier signal. In both cases, small differences result in the possible identification of the glass bead. However, the potential defect peak is below or close to the noise floor, and if the sample was not transparent and the flaw could not be visually identified, the signal would be easy to miss. This weak signal is the result of the glass bead and epoxy having the lowest impedance mismatch of all the defects tested. This is represented by the reflection coefficient of 0.346 in Table 5.

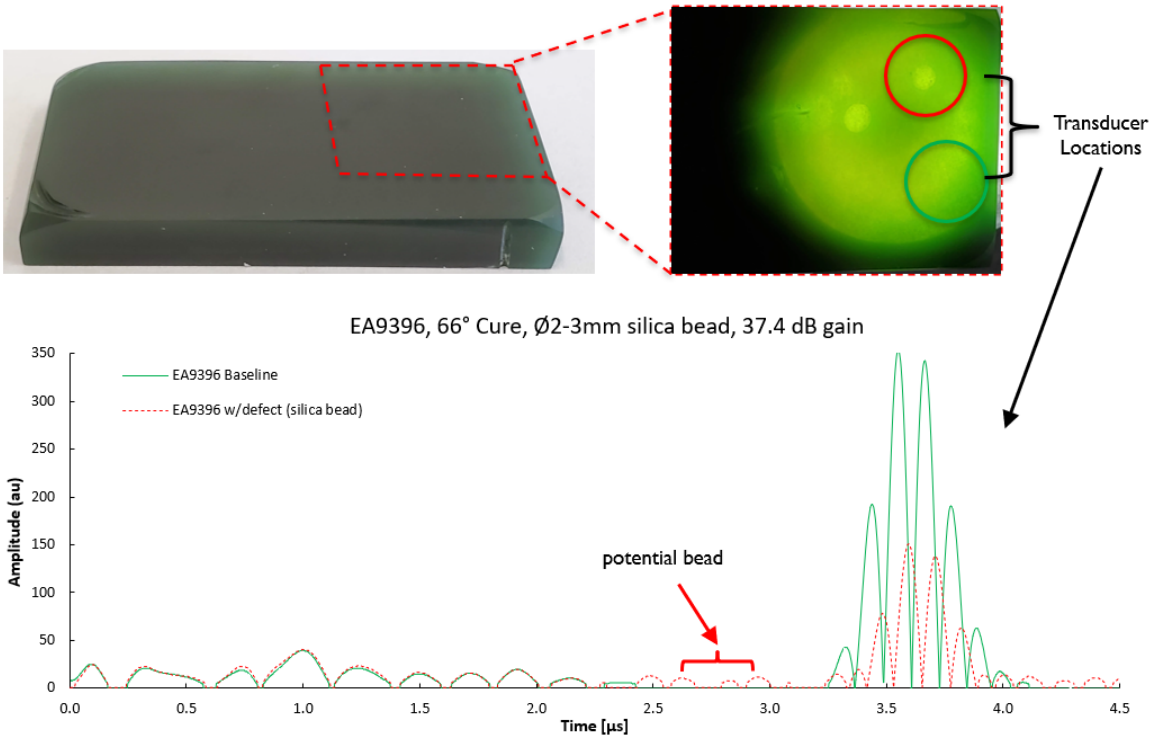

Figure 20. Top: pure EA9396 sample with glass bead defect and transducer locations. Bottom: signals from two different transducer locations and possible glass bead signal peak.

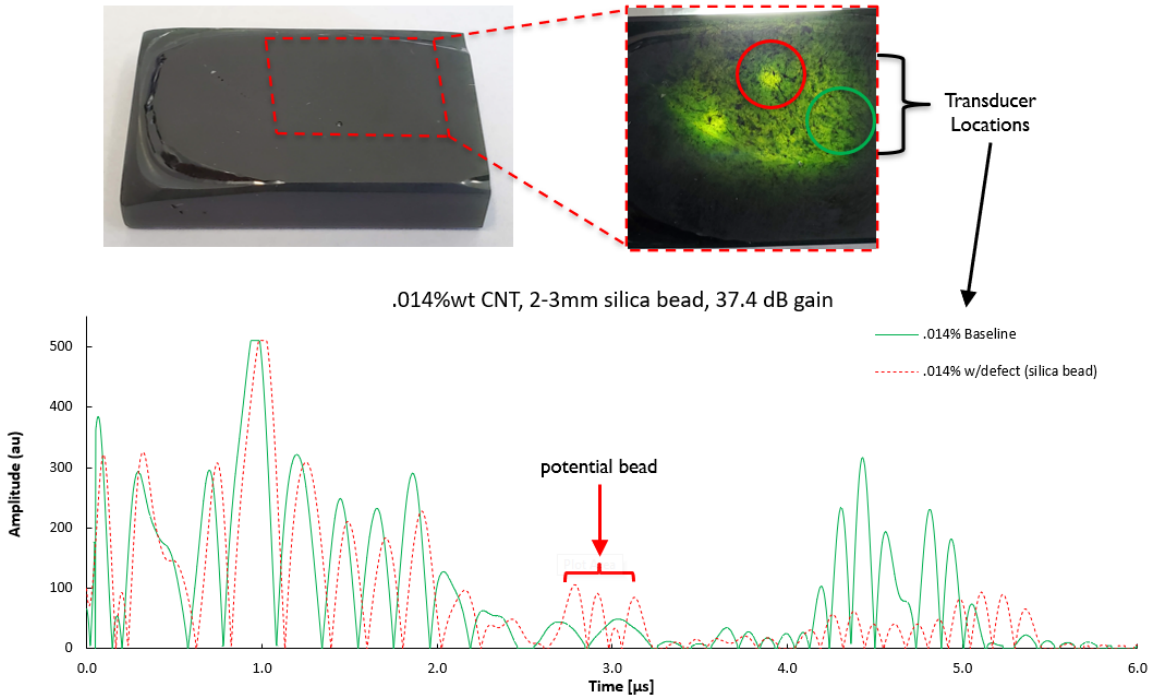

Figure 21. Top: 0.014 wt% CNT EA9396 sample with glass bead defect and transducer locations. Bottom: signals from two different transducer locations and possible glass bead signal peak.

c. Copper Wire

Copper wire was used in four diameters: 0.56mm, 0.38mm. 0.25mm., and 0.15mm. The wires were encased in pristine EA9396 and 0.014 wt% CNT loaded Epoxy. The wires migrated during the curing process from their original centerline location. As a result, the signal peaks are seen in different locations, corresponding to different depths, within the epoxy. The results are presented for the bare EA9396, and CNT loaded composite in Figure 22 and Figure 24, respectively. All wires were detected in the bare epoxy. The 0.014 wt% CNT composite had similar results with the exception that the smallest wire of 0.15 mm was unable to be detected. This would indicate a flaw limit of below 0.15 mm in bare epoxy and ~0.2 mm in the 0.014 wt% CNT sample. This correlates well with expectations. Due to the increased porosity in associated wave scattering increasing noise and signal attenuation decreased resolution is anticipated.

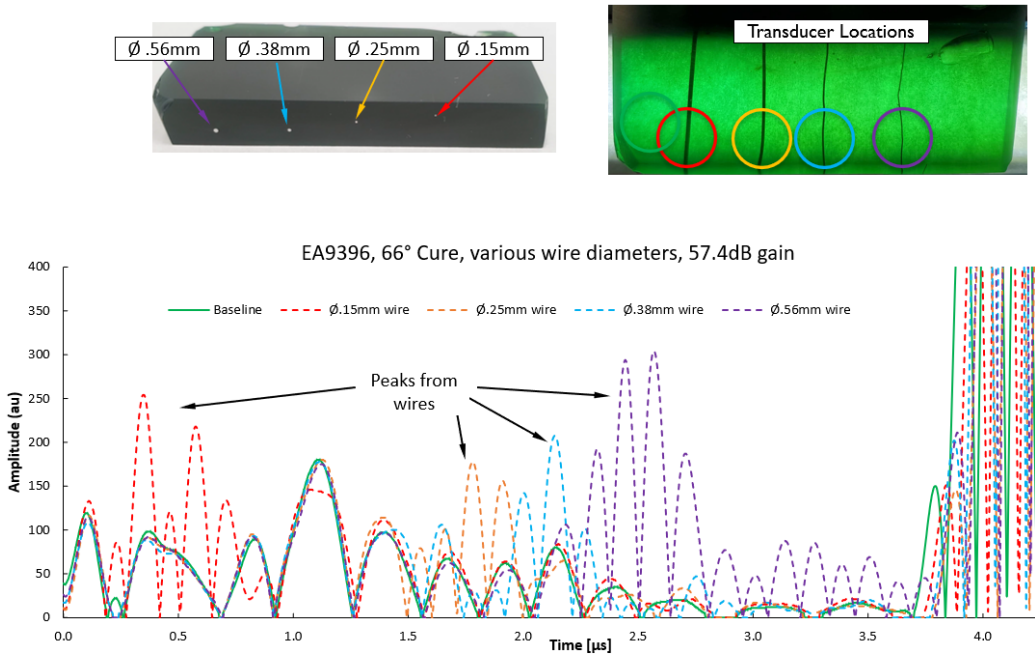

Figure 22. Top: pure EA9396 sample with copper wire defects. Bottom: signals from two different transducer locations and possible glass bead signal peak.

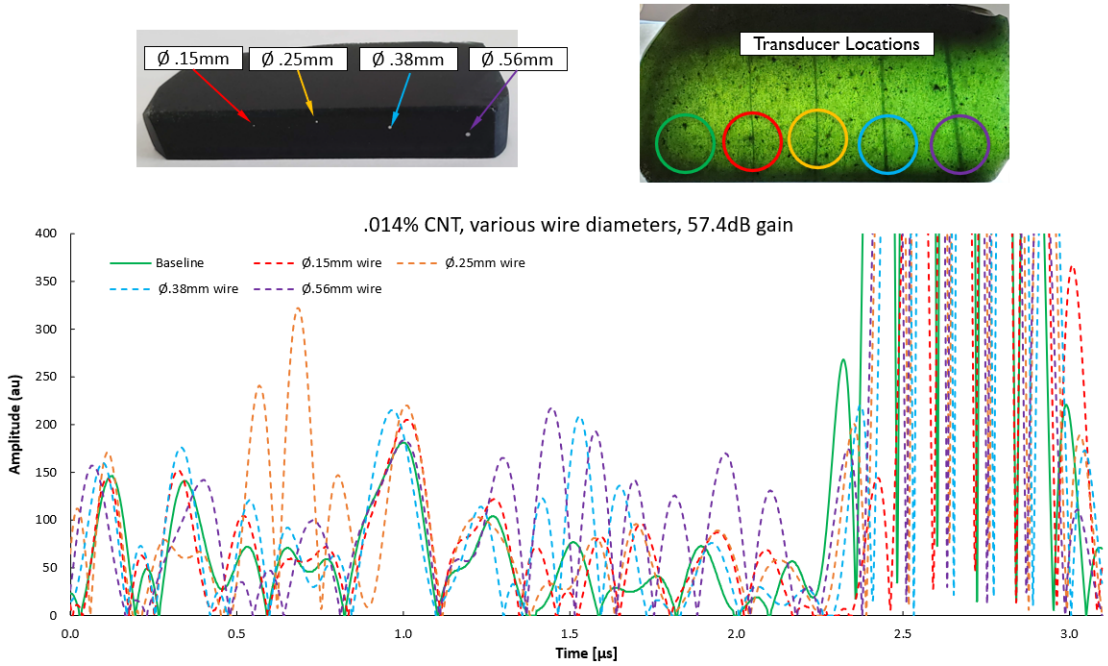

Figure 23. Top: 0.014 wt% CNT sample with copper wire defects. Bottom: signals from two different transducer locations and possible glass bead signal peak.

d. Holes

Holes were drilled with diameters ranging from 0.3429 - 0.8890mm in 0.014, 0.2, and 0.75 wt% CNT samples. Figure 24, Figure 25, and Figure 26 show the samples used, transducer locations, and corresponding signals for each defect and a specified baseline.

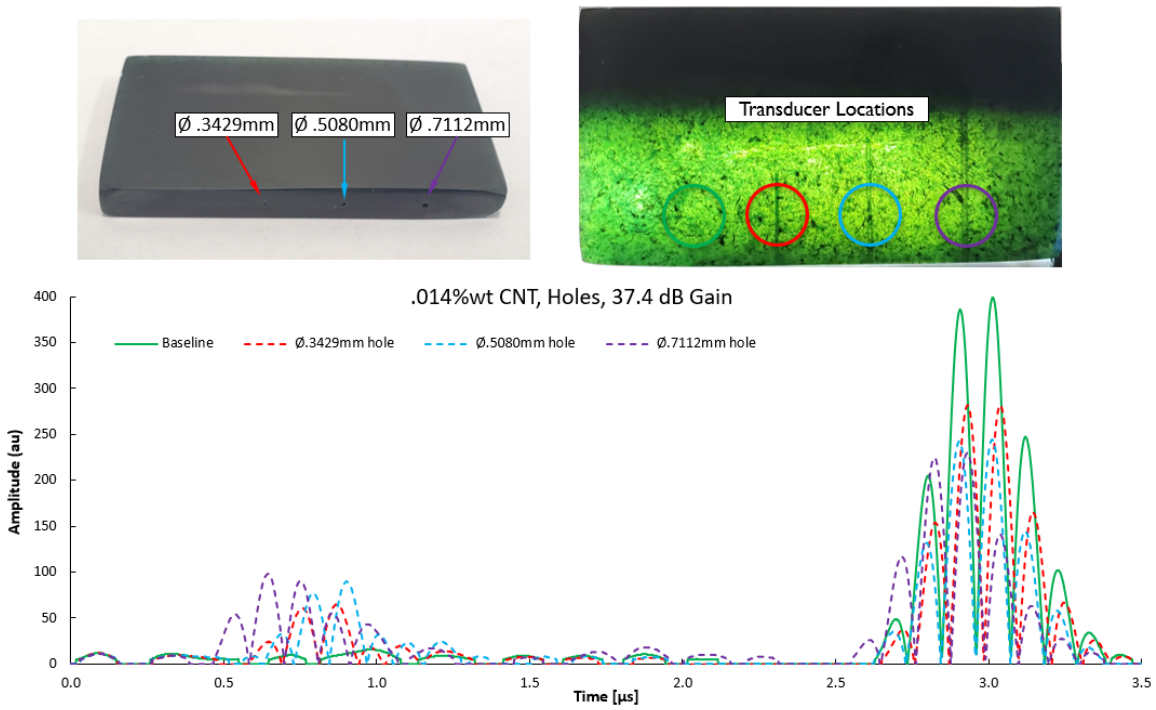

Figure 24. Top: 0.014 wt% CNT EA9396 sample with drilled holes. Bottom: resulting signals.

The 0.014% sample demonstrated the highest resolution of the 3 CNT loaded samples. All three holes, the smallest of which was 0.3429mm in diameter was easily identified by its distinct signal peak. The 0.2 wt% sample only resulted in identification of only the two larger holes, 0.0580 and 0.7112 mm. None of the four holes were able to be detected in the 0.75% sample.

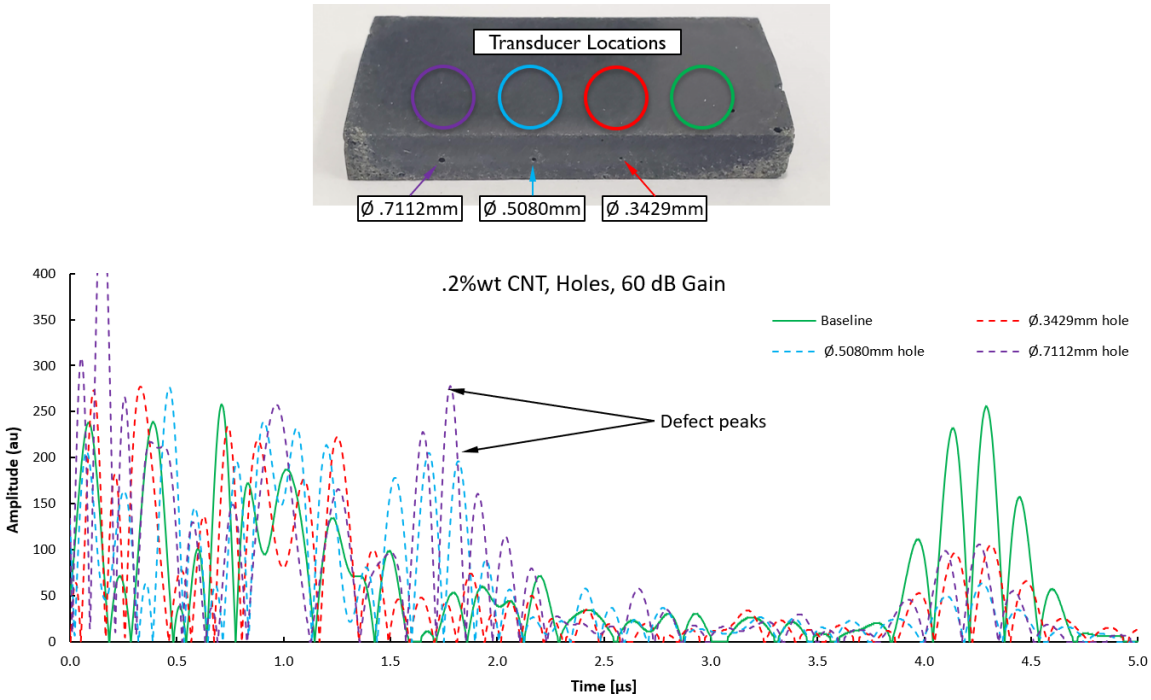

Figure 25. Top: 0.2 wt% CNT EA9396 sample with drilled holes. Bottom: resulting signals.

This was achieved a with a gain of 37.4 dB in the 0.014% vice 60 dB for 0.2 and 65 dB for 0.75%. Contrasting overall acoustic signatures with higher loadings of 0.2 and 0.75 wt% CNT a large difference in noise, particular shallow in the sample, i.e., left of 2 µs in the figures, is seen. This makes it more difficult to positively identify defect in this area. For example, in the 0.75% sample, there are many peaks that could potentially be defects, however, are not consistent nor distinct from the noise present. This, combined with a unique increase in the background peak, makes it impossible confirm a successful defect identification. In all other cases discussed here, the background peak of the baseline is the most prominent. This is expected (see Figure 12), however, with the 0.75% sample "defect" locations all resulting in a larger amplitude background. This is likely a product of the higher density of scattering pores resulting in an unreliable signal and supported by the increased noise throughout.

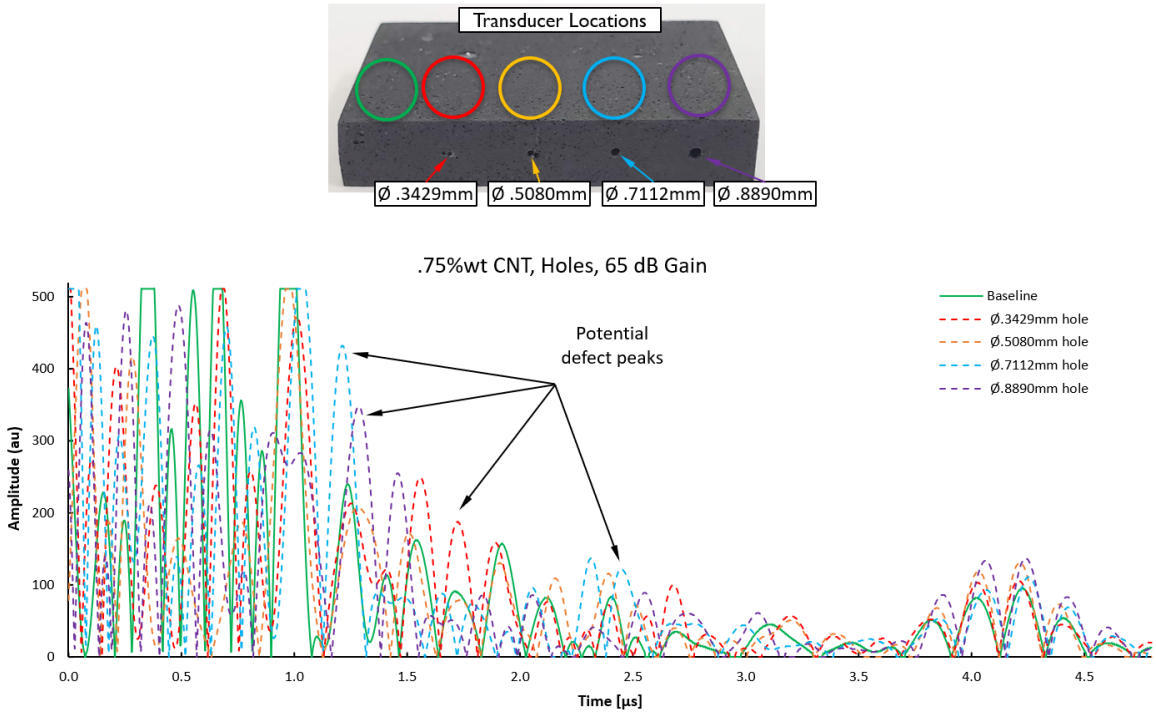

Figure 26. Top: 0.75 wt% CNT EA9396 sample with drilled holes. Bottom: resulting signals.

D. CONCLUSION

The longitudinal velocity and density of samples ranging from pure epoxy to that containing 0.75 wt% CNT was measured. Longitudinal velocity decreased with increasing CNT loading. The measured density decreased with increased CNT loading. Composite fabricated with 0.75wt% CNT resulted in the lowest density, 15.5% less than bare EA 9396. Density changes were likely the result of increased sample porosity caused by the increased CNT loading resulting in viscous mixtures that readily retain entrapped air during the vacuum dispersion and curing process.

In these samples, four different defects were introduced, ultrasonic testing as a method of flaw detection was characterized. A summary is provided in 0, where red color indicates failure of detection utilization UT methods and green indicates the flaw was detected. At least one of the studied flaws was detected at all loadings with the exception of the 0.75 wt% CNT sample, where not even large holes could be detected. Defects with lower reflectivity coefficients (less acoustic mismatch) resulted in decreased detection in

all cases (concentrated CNTs, Glass beads). Limits on flaw detection resolution were determined to be < 0.15 mm for bare EA9396, 0.25 mm for 0.014 wt% loading, 0.51 mm for 0.2 wt% CNT loading, and > 0.89 mm for 0.75 wt% loading. Decreases in resolution were determined to be the result of scattering of acoustic waves impinging on air bubbles formed through increased porosity. Controlling porosity of the composite would be critical in ensuring the success of any ultrasonic testing effort. As discussed in the introduction, resolution is limited to 100s of μm by the 5MHz operating frequency. Decreasing this level of sensitivity requires advanced methods like impulse acoustic microscopy that utilize higher frequencies.

Table 8. Summary of the outcome of defect detection in the presented samples.

Matrix Material	5% CNT	Glass Bead Dia.	Wire Dia.	Hole Dia.
EA9396 (66° Cure)	~Ø4mm, ~2mm thick	2-3mm	0.15mm	
			0.25mm	
			0.38mm	
			0.56mm	
EA9396 w/ 0.014wt% CNT		2-3mm	0.15mm	0.34mm
			0.25mm	0.51mm
			0.38mm	
			0.56mm	0.71mm
EA9396 w/ 0.2wt% CNT				0.34mm
				0.51mm
				0.71mm
EA9396 w/ 0.75wt% CNT				0.34mm
				0.51mm
				0.71mm
				0.89mm
			Defect detected	Defect not found

THIS PAGE INTENTIONALLY LEFT BLANK

IV. INTRODUCTION OF RARE-EARTH OXIDE NANOPARTICLES IN CNT-BASED NANOCOMPOSITES FOR IMPROVED DETECTION OF UNDERLYING CNT NETWORK

A. BACKGROUND

This chapter was previously published in the carbon-based nanocomposites special issue of the journal *Nanomaterials* by Multidisciplinary Digital Publishing Institute (MDPI) [111]. Minor edits and additions have been made to adapt the text to the current manuscript.

Nanoscale composites utilizing carbon nanotube (CNT) filler allow for significant reductions in resistivity of an otherwise highly insulating matrix material while requiring extremely low CNT loadings [107]. These improved conductivities result in an attractive material with extensive applications in diverse industries, but particularly for electrostatic discharge (ESD) and electromagnetic interference (EMI) prevention [7,10,78,103–106,161–163]. These enhancements are heavily dependent on nanofiller dispersion in the matrix material. Dispersion control becomes essential to ensuring uniform properties throughout the composite and eliminating hotspots that could affect reliability or performance.

Validation of uniform dispersion is difficult due to minimal contrast differences between CNTs and the surrounding matrix, making conventional imaging techniques difficult. Existing high-resolution methods include thermography in the infrared (IR) range [19] and voltage-contrast imaging with scanning electron microscopy (SEM) [5,20,21,108–110]. Both have been used to understand dispersion and nanostructures but are limited by the processing time and low fields-of-view. Thermography techniques are depth limited as the subsurface information is extrapolated.

Nondestructive evaluation (NDE) techniques that make the differences in the dispersion of the nanofiller or the porosity of the surrounding matrix readily apparent would be useful as the industrial use of these composites increases. This work aimed to improve the contrast of the CNT network through the addition of rare-earth oxides, specifically europium doped yttria, to the CNT surface. Europium doped yttria has been

found to emit red light under stimulation by deep ultraviolet (DUV) wavelengths [164,165]. Since its discovery, Eu:Y_2O_3 has become a common red phosphor material due its narrow emission peak, easy stimulation under DUV radiation, and high quantum efficiency [166–169]. Efforts to exploit the demonstrated luminescence for increased visibility in bioimaging have been explored through the use of Eu:Y_2O_3 nanorods [170] and nanoparticles incorporated into CNT cavities [171]. Coincidently, rare-earth elements are heavier than those present in a conventional CNT composite, e.g., iron, carbon, and polymer chains. These heavier elements facilitate the compositional contrast through backscatter electron production in SEM imaging. By collocating Eu:Y_2O_3 nanoparticles and CNTs (hereafter Eu:Y_2O_3-CNT), the detection of red-emissions or the detection of heavy elements, yttrium and europium, can reveal the location of an underlying CNT network and make bulk dispersion determinations of the CNT filler easier to visualize and at greater depths.

B. EXPERIMENTAL METHODS

1. Materials

The CNT pulp that served as substrate for the Eu:Y_2O_3 nanoparticle synthesis, and for the epoxy composite fabrication, was a multiwall carbon nanotube (MWCNT) product provided by Nanocomp Technologies Inc. (Huntsman Corporation, Merrimack, NH, USA). This nanofiller is produced as CNT sheets via a chemical vapor deposition (CVD) process facilitated by an iron (Fe) catalyst and subsequently reduced to a pulp by employing a Hollander Beater and industrial burr [172]. The pulp consists of MWCNT bundles approximately 0.05 mm in diameter and 1mm in length with individual CNT diameter in the order of 30 nm. The pulp used throughout this research comes from a single production run (Lot C) and is contrasted later with CNTs from past batches (Lot A,B).

Yttrium (III) and europium (III) nitrate hexahydrate obtained from Sigma Aldrich (St. Louis, MO, USA) with a purity of 99.8% and 99.99%, respectively, were used as precursors and dissolved in a > 99.5% pure ethanol also obtained from Sigma Aldrich.

2. Carbon Nanotube Preparation and Eu:Y_2O_3 Nanoparticle Synthesis

Sample generation consisted of a three-step process where CNTs were (1) activated, (2) Eu:Y_2O_3 synthesized along tube walls, and (3) the resulting pulp dispersed into an epoxy matrix to form the nanocomposite.

The CNT pulp was first activated to facilitate the nucleation of rare-earth oxides at activation sites. CNTs were placed in an alumina boat and thermally activated by heating them to 500 °C in a tube furnace (Thermo Scientific Lindberg/Blue M model TF55035A-1, Waltham, MA, USA) for either 1, 2, or 2.5 h in an air atmosphere. The europium and yttrium nitrates were mixed into the activated CNT bundles via wet impregnation aided by the sonication technique illustrated in Figure 27a. Yttrium (III) and europium (III) nitrate hexahydrate and the activated CNT pulp were weighed to achieve europium substitution within the Y_2O_3 with a targeted stoichiometry of $(Y_{0.85}Eu_{0.15})_2O_3$ and a 5%wt of Eu:Y_2O_3 in the CNT pulp. The nitrates were dissolved in 10 mL of ethanol and the resulting solution poured over the CNT pulp and agitated in an ultrasonic bath for several seconds. The saturated CNT bundles were dried at 50 °C for 2 h in a convection oven (Binder GmbH, Tuttlingen, Germany). Once dried, the remaining pulp and the alumina boat were placed in the tube furnace and purged with argon for 30 min. The mixture was calcinated in an ultrahigh purity argon atmosphere for 2.5h at 850 °C. The pulp was allowed to cool to room temperature over ~3h under Ar.

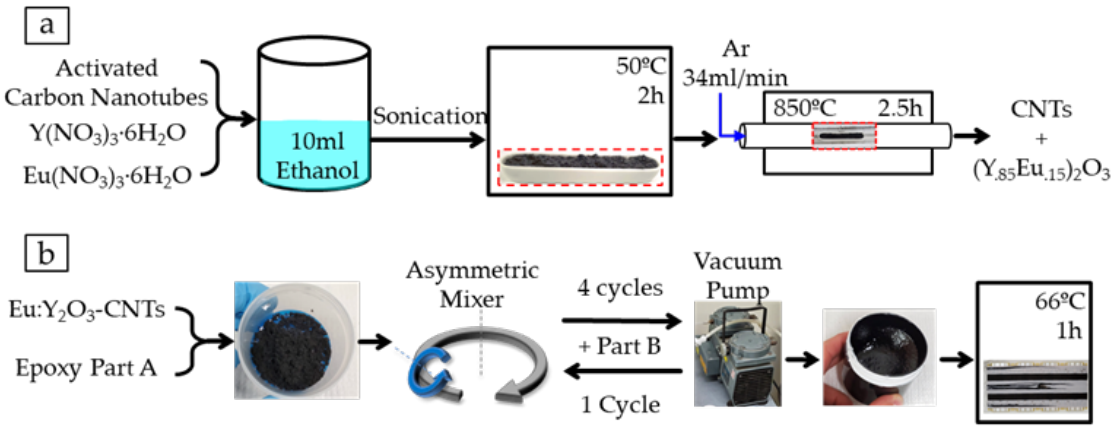

Figure 27. Depiction of the processes for a) synthesizing Eu:Y_2O_3 nanoparticles to CNT walls; b) fabrication of composite electrical boards and samples from epoxy and CNT pulp.

3. Nanocomposite Fabrication

The nanocomposites used throughout this study were synthesized using the CNT pulp described in Section 2.1 and a two-part aerospace-grade epoxy matrix, Loctite Hysol EA 9396 (Henkel Corporation, Dusseldorf, Germany). The two-part epoxy was employed at a ratio of 100:30 by weight (part A:part B). All samples were cured at 66 °C for 1 h. The base epoxy mixture had a reported electrical resistivity of 2.14×10^{15} Ohm-cm, tensile strength of 35.2 MPa, and lap shear strength of 27.6 MPa at 25 °C [56].

The CNT dispersion and electrical board fabrication is illustrated in Figure 27b. The epoxy and CNTs were weighed to generate the desired loading (0.75%wt) and then dispersed by mixing in a FlackTek asymmetric speed mixer (Landrum, SC, USA). The mixer was operated for 3 min at lower speeds followed by three 1 min higher-speed cycles with Part B added before the final cycle. A vacuum pump was used to evacuate the air from the hermetic vessel where the samples were contained (low vacuum range) throughout the mixing process. The mixture was then applied to prefabricated electrical boards and, separately, poured into molds for curing. A convection oven (Binder GmbH, Tuttlingen, Germany) was used for the 66 °C curing process.

4. Thermo-Gravimetric Analysis

Untreated CNT pulp was analyzed in a simultaneous thermal analyzer (STA) 449 Jupiter F1 (Netzsch GmbH & Co. Holding KG, Selb, Germany) to determine initial iron catalyst content. Data was collected during a temperature-programmed oxidation, heating the CNTs under a 20% O_2 80% N_2 environment analogous to sea-level atmosphere composition, at a rate of 15 °C/min from room temperature to 850 °C.

5. Material Characterization and Imaging

A benchtop powder X-ray diffraction (XRD) Rigaku Miniflex 600 (Woodlands, TX, USA) with a Cu-Source was used to determine crystalline phases throughout the process of activation and Eu:Y_2O_3 inclusion.

An optical metallurgical microscope Nikon Epiphot 200 (Melville, NY, USA) was employed for low magnification observation of the CNT dispersions within the epoxy matrix.

A Zeiss Neon 40 (Zeiss, Oberkochen, Germany) Dual Beam SEM operating from 2 to 20 KV was utilized to investigate microstructural features of untreated CNT and Eu:Y_2O_3-CNT bundles and the resulting CNT epoxy composites. Secondary electron (SE) and backscattered electron (BSE) images were collected.

High-resolution transmission electron microscopy (HRTEM) images were acquired using a FEI Tecnai Osiris TEM (Hillsboro, OR, USA). TEM bright-field images were captured with an accelerating voltage of 200 kV, a second condenser aperture of 50 µm, and an objective aperture of 40 µm. Scanning TEM (STEM) was used in conjunction with a high angle annular dark-field (HAADF) detector for energy dispersive X-ray (EDX) spectroscopy studies, the TEM's coupled Super-X system.

Micro-computed tomography (micro-CT) was utilized on two composite samples to determine if improvements in network detection were possible with Eu:Y_2O_3-CNT samples. The analysis was performed with a Zeiss Xradia 520 Versa (Zeiss, Oberkochen, Germany). Scan parameters were 100 kV source voltage, 9W power, and 10x optical magnification. The source and detector distances were adjusted to achieve a voxel size of

approximately 0.7 µm3 and 1601 projections through 360 degrees were collected with an exposure time of 1s. Three-dimensional (3D) tomograms were rendered using tomviz freeware [173].

6. Deep Ultraviolet Fluorescence

Photoluminescence measurements of Eu:Y_2O_3-CNT composite samples were conducted using a LabRAM HR Raman Microscope (Horiba Scientific, Kyoto, Japan). A deep ultraviolet (DUV) source with an emission wavelength of 229nm was used with a 600 gr/nm grating. Source power was limited to 100 µW due to sample degradation resulting in broadening of spectra peaks at higher intensities.

7. Conductivity Characterization

All electrical measurements were done by analyzing the prefabricated eight-point circuit boards with a 2400 Keithley source meter (Tektronix, Inc., Beaverton, OR, USA) operating as a current source and can be seen in Figure 28. A separate digital multimeter (DMM) was used to measure the voltage drop across the 1 cm wide epoxy section. One spot location was sectioned, and the thickness was measured via a Nikon Epiphot 200 reflective optical microscope (Nikon, Tokyo, Japan) to determine an average film thickness. The electrical resistivity was then derived using Equation (ii) in Figure 28.

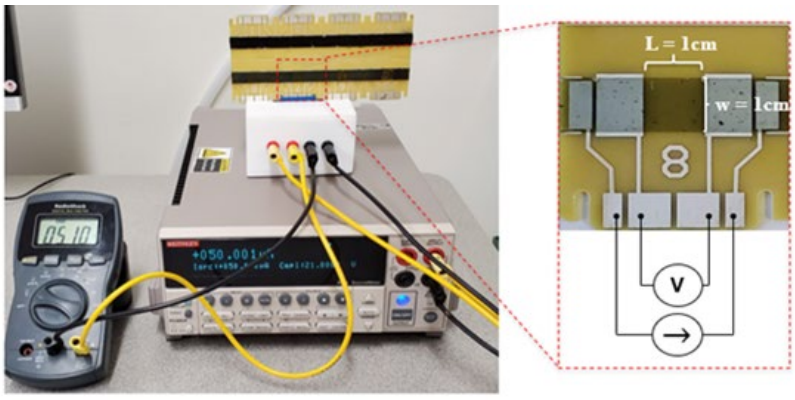

i) $V = IR \Rightarrow R = \frac{V}{I}$ ii) $\rho = \frac{RA}{L} = \frac{Rwt}{L} = Rt$

Figure 28. Experimental setup for measuring electrical resistivity and governing equations.

C. RESULTS AND DISCUSSION

1. Characterization of CNT Pulp and Synthesized Eu:Y_2O_3 Nanoparticles

Scanning electron microscopy observations of untreated, activated, and Eu:Y_2O_3-CNT pulp were conducted and are shown in Figure 29. The untreated pulp shown in Figure 29a consisted of tight bundles of CNTs, in contrast with Figure 29b, where the loosely packed bundles of CNTs activated for 2.5 h can be seen. Figure 29c shows a section of the Eu:Y_2O_3-CNT pulp that exemplified a feature observed in all sample locations; increased laxity of the bundle structure. This progressive breakdown of the bundled CNTs results from the mechanical agitation associated with handling and sonication during the activation and Eu:Y_2O_3 nanoparticle synthesis.

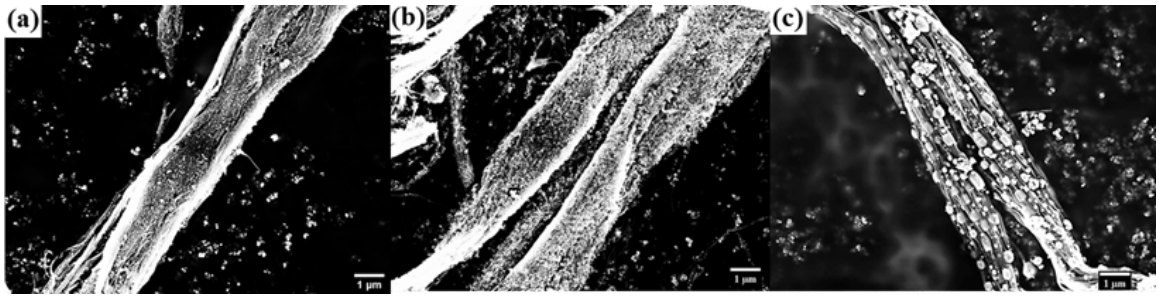

Figure 29. SEM imaging of CNT bundles at 10kX magnification: a) untreated CNT bundles, b) activated bundles, and c) Eu:Y_2O_3-CNT bundles.

HRTEM analysis was conducted to determine the location of the synthesized Eu:Y_2O_3. In all cases, the rare-earth oxides were found adhered to CNT bundles or to surrounding Fe particulates, never as individual particulates. CNT bundles were found to have Eu:Y_2O_3 nanoparticles of approximate diameters from 3 to 20 nm adhered to the tube or Fe surface despite the use of sonication to disperse the sample for observation. HRTEM analysis with the corresponding EDX elemental maps for Fe, Y, Eu, and oxygen are presented in Figure 30. Figure 31 shows a study performed in a different section of the sample and is included to point out that the Eu:Y_2O_3 distribution in the samples occurred throughout the CNT network, to include both the Fe catalyst and bare CNT surfaces.

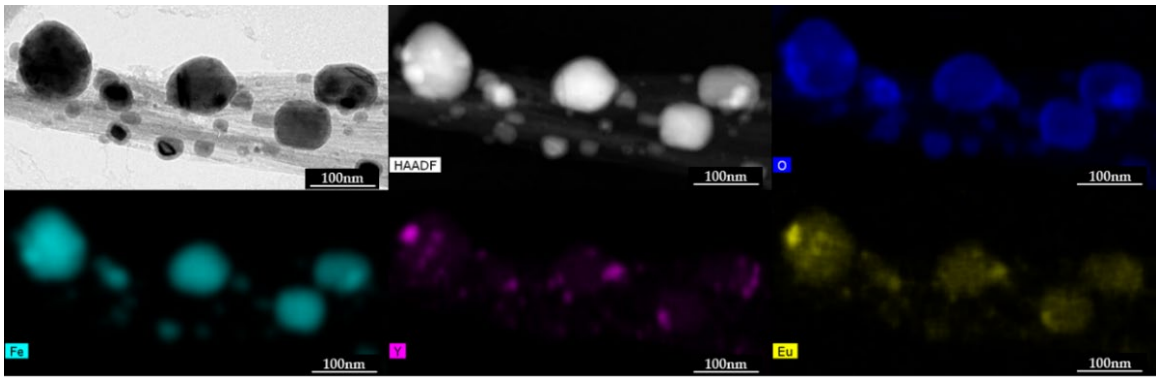

Figure 30. HRTEM, HAADF, imaging and EDX mapping of CNT bundles showing elemental distribution.

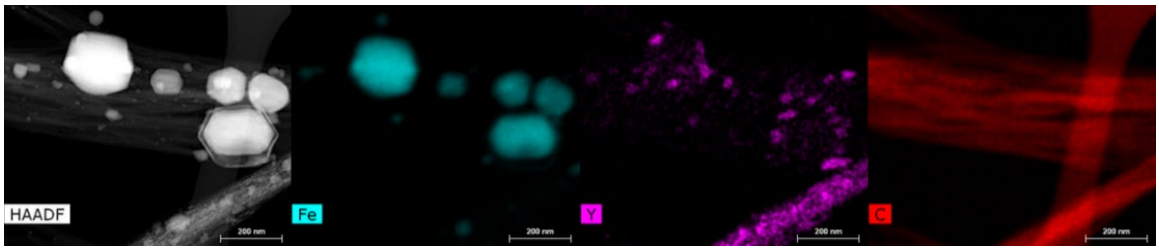

Figure 31. HAADF imaging and EDX mapping of CNT bundles showing the Yttria distribution on CNT wall.

Iron particles, internal and external to the CNTs, with diameters between 10 and 120 nm, could be seen in all the sections analyzed and are a remnant of the CNT growth process that utilized iron as a catalyst. Larger iron particles> 30 nm were found on the tube surface and were surrounded by an oxide shell of approximately 5–8 nm in thickness. Synthesized europium-yttrium oxide particulates were distributed throughout the CNT and Fe surfaces and as agglomerated nodules reaching 20 nm in diameter on larger iron particles. This colocation of Eu:Y_2O_3 nanoparticles along the tube walls ensures that their detection indicates the presence of an underlying CNT bundle. It is worth noting that some of the Fe particulates appeared to sinter during the step meant to decompose the nitrates, conducted at 850 °C and described in B.3.

X-ray diffraction was conducted with untreated CNTs, CNT pulp activated for 2.5 h, and the final product of 5wt% Eu:Y_2O_3-CNT pulp. Figure 32 presents the three samples with significant phases identified.

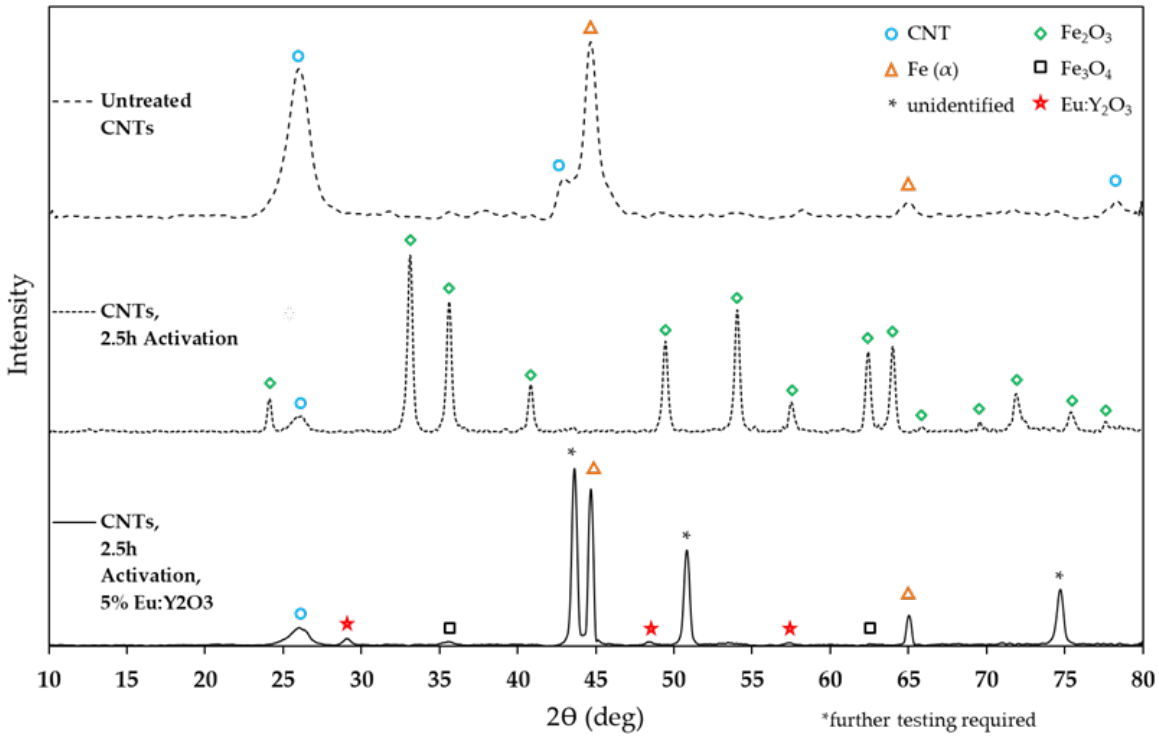

Figure 32. XRD analysis of untreated, activated, and Eu:Y_2O_3-CNT pulp with corresponding phases identified.

Untreated CNT pulp contained the ferritic iron used as a catalyst during the growth process and was left in place. Subsequent TGA analysis on the same pulp determined the iron content to be 25.6% by weight. Activation of the untreated pulp resulted in complete oxidation of the iron to form iron (III) oxide, Fe_2O_3. The Eu:Y_2O_3-CNT pulp sample exhibited iron and a new iron oxide phase, Fe_3O_4. The Eu:Y_2O_3 synthesis process introduced europium and yttrium nitrate hydrate and required calcination. These precursors underwent thermal decomposition of the hydrates and off-gassing of oxynitrates in various stages before eventually decomposing into the target oxides between 600 and 700 °C [174,175]. This same process results in the reduction of Fe_2O_3 to Fe_3O_4 and iron. The peaks identified as Eu:Y_2O_3 are consistent with JCPDS #058-0800 where similar Eu doping of the Y_2O_3 lattice was conducted as $(Y_{0.8}Eu_{0.2})_2O_3$.

A phase was also identified in the completed Eu:Y_2O_3, marked in Figure 32 by an asterisk symbol. Two potential candidates were identified, iron nitrides with stoichiometric

close to FeN_x (with $0.03 < x < 0.09$) or a carbon allotrope referred to as n-diamond (new-diamond). Previous studies have cataloged peaks with these iron nitrides [176]. However, data has suggested that pure single phases where $x < 0.2$ have not been observed and are energetically unfavorable [177]. N-diamond was discovered by Hirai and Kondo [178] at high temperatures and pressures and has since been synthesized by numerous groups in varying conditions [179]. The most relevant by Wen et al. using iron-catalyzed CNTs at atmospheric pressures and temperatures as low as 800 °C [180] at the sacrifice of the degradation of the CNT structure—something not seen here. Further analyses are required to unequivocally differentiate the phase that gives origin to these peaks.

In sum, the XRD analysis confirmed the presence of Eu:Y_2O_3 and TEM identified it as collocated with the CNT network.

The Eu^{3+} doping of yttria produces known photoluminescence in the visible spectrum. Figure 33 shows the emission spectra of Eu:Y_2O_3-CNTs under an excitation wavelength of 229 nm. The peak at 611 nm is the characteristic spectra indicative of Eu^{3+} transition from 5D¬0 → 7F2 that results in the desired red luminescence [164,165,168] and confirms the successful introduction of Eu3+ ions into the host Y2O3 lattice

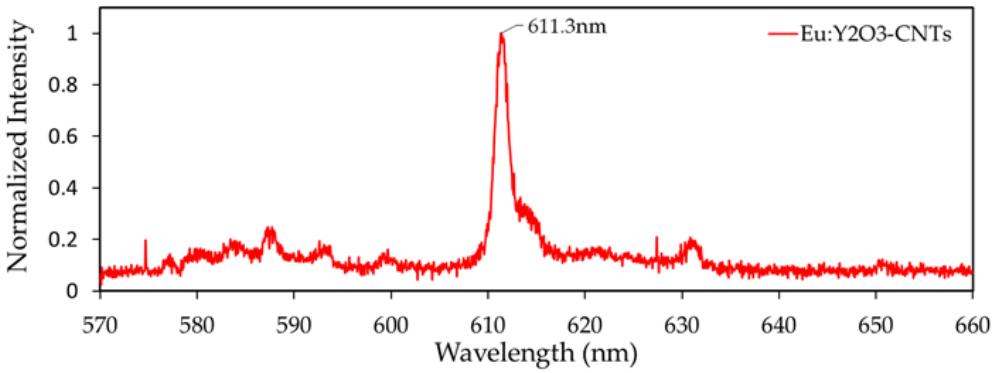

Figure 33. Photoluminescent spectra resulting from 229 nm excitation of 5 wt% Eu:Y_2O_3 CNTs that had been activated for 2.5 h.

2. Characterization of the CNT and Eu:Y_2O_3-CNT Composites and Their Electrical Performance

Optical microscopy observations of epoxy nanocomposite films can be seen in Figure 33. The three-dimensional network of CNT bundles is comprised of bundles of increasingly smaller diameter and length at each step of the Eu:Y_2O_3-CNT production process. Under SEM imaging, the CNT pulp in Figure 29 exhibited laxation of the CNT bundle due to mechanical agitation. Dispersing the CNT pulp in the epoxy was done via a dual asymmetric mixer. It is suspected that the shear forces resulting from mixing in epoxy further separate the CNT bundles. Through inspection of Figure 34, the process the CNT pulp goes through seems to result in a smaller mean bundle size. When comparing the untreated CNT pulp, with that activated, and finally that of synthesized and calcined Eu:Y_2O_3 nanoparticles, the overall width and length of CNT bundles seems to decrease, resulting in a less robust network.

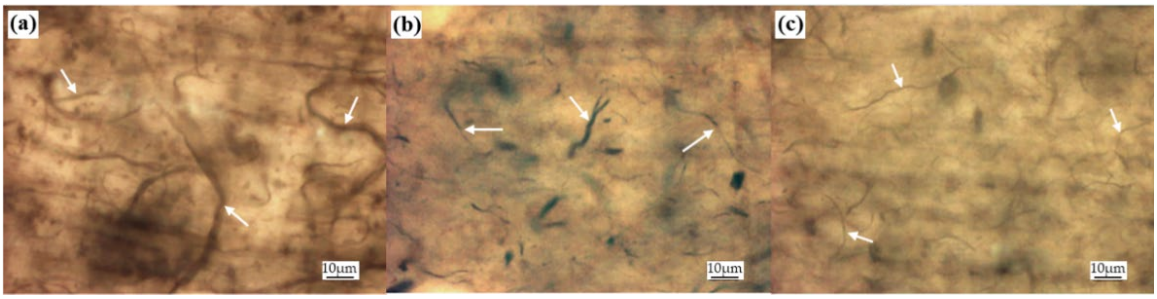

Figure 34. Magnification microscope 50X images revealing CNT bundles, indicated by white arrows, in nanocomposites created from: a) untreated CNT pulp, b) 2.5 h activated CNT pulp, and c) Eu:Y_2O_3-CNTs.

Observationally, significant decreases in viscosities were seen between the uncured samples and support the previous discussion. The uncured epoxy with untreated CNT filler must be manually deposited into a mold and has a distinct texture, while the uncured Eu-Y_2O_3-CNTs epoxy is smooth and can be readily poured.

The electrical resistivity of the bulk nanocomposite must remain below 10–106 and 106–1011 Ohm-cm to maintain its applicability for EMI and ESD prevention applications,

respectively [11]. Figure 35 presents the measured electrical resistivity of the epoxy composite as a function of %wt CNT loading. The samples generated in the present study span a large portion of the usable range for EMI and ESD applications. The composites based on 2.5 h activated CNTs had a resistivity roughly equal to past 0.014%wt CNT loadings of inactivated CNTs. However, once Eu:Y_2O_3 was included in the CNT epoxy, those values diminished, that is, the electrical conductivity increased.

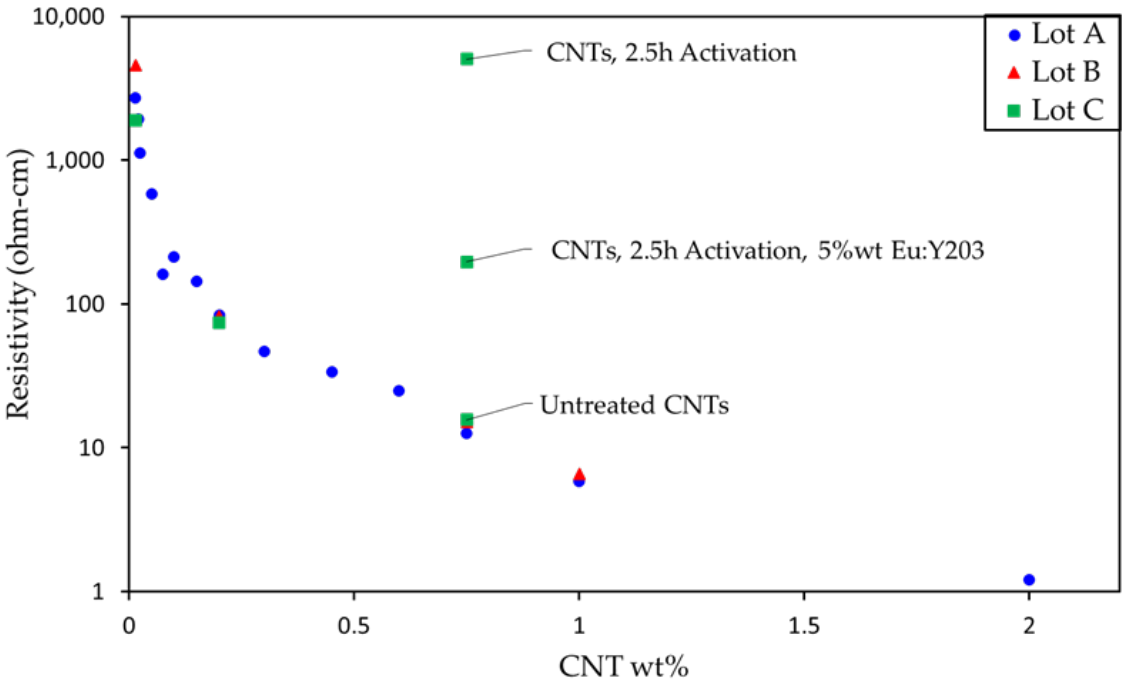

Figure 35. Measured electrical resistivity of current CNT pulp (Lot C) contrasted with past production runs (Lot A,B) with an applied current of 400 µA.

Different activation times were explored, with each activated pulp subsequently subjected to synthesis of the Eu:Y_2O_3 nanoparticles. The resulting resistivity is plotted in Figure 36. The composite fabricated from untreated CNTs (0h activation), 1, 2, and 2.5 h activation times resulted in resistivities of 15.67, 60.47, 982.7, and 5058 Ω-cm, respectively. After synthesizing Eu:Y_2O_3, the untreated, 1 h, 2 h, and 2.5 h activated samples measured resistivities of 12.40, 18.14, 79.29, and 196.4 Ω-cm. Increases in resistivity during activation are attributed to the oxidation of the iron catalyst remaining

from the CNT growth process into iron (III) oxide, a known electrical insulator [38]. Further, the activation process results in oxygen containing species in the form of ether C-O-C and quinone C=O groups along the CNT surface and likely plays a role in this decrease [118]. The resistivity improvements seen during the subsequent calcination are attributed to the reduction of the iron (III) oxide to small amounts of iron (II oxide) and iron. This is supported by the phase analysis presented in Figure 32.

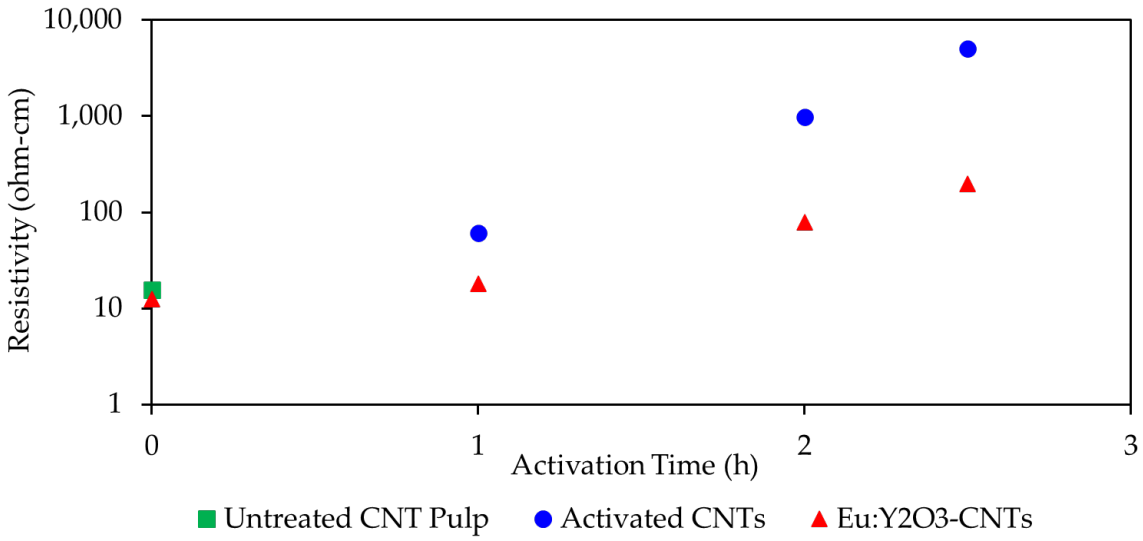

Figure 36. Effects of activation and inclusion of Eu:Y_2O_3 particles on electrical resistivity on nanocomposite samples with 0.75 wt% CNT loading.

Figure 37 presents the resistivity as a function of applied current. Standard deviation across samples is stable at ~5–10% of measured resistivity. Decreasing resistivity under increased current application was seen for the activated CNT composite. A resistivity reduction of 9.4% across the full current range was recorded. The drop across the full scale in the untreated and Eu:Y_2O_3-CNT samples was <1%. Past research has documented similar behavior -at the high resistivities associated with 0.014%wt CNT composites. This current dependence with increasing current application is ascribed to temperature increases due to resistive heating and irreversibility in the conductive path within the composite. Further discussion can be found in [107]. Notably, a reduction in resistivity (increased conductivity) is a positive attribute for the proposed applications.

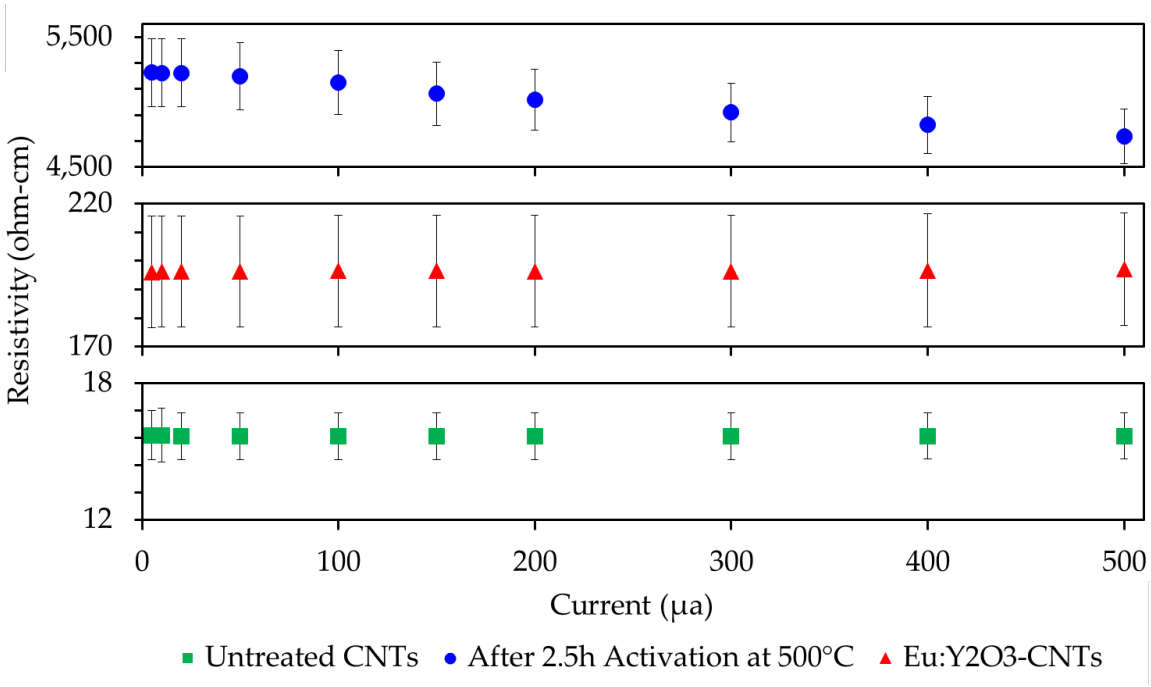

Figure 37. Electrical resistivity as a function of applied current for composites made with 0.75 wt% CNTs at different phases of the preparing and Eu:Y_2O_3 synthesis process.

3. Scanning Electron Microscopy and Micro-Computed Tomography

SEM imaging was conducted on untreated CNT pulp, Eu:Y_2O_3-CNT, and nanocomposites fabricated from those two samples. SE and BSE images of CNT pulp (no epoxy) and epoxy CNT nanocomposites are compared in Figure 38 and Figure 39.

For CNT pulp, the addition of Eu:Y_2O_3 results in easier identification of individual tubes due to the increased contrast of the collocated CNT, the sintered Fe particulates and the Eu:Y_2O_3 when conducting SE imaging (Figure 38a vs. c). The larger particulates observed in Figure 38c correspond to the sintered Fe, while the Eu:Y_2O_3 is finely dispersed. BSE detection is improved with the addition of the Eu:Y_2O_3 oxide nanoparticles due to both the presence of heavier elements absent from the bare CNT pulp and that the Fe particulates remained at smaller sizes in the untreated CNT pulp. The contrast between Figure 38b,d is remarkable; Figure 38d shows a brighter tone for the Eu:Y_2O_3, previously identified by TEM as the finely dispersed particles, than for Fe. The CNT network is barely

distinguishable in the background. BSE imaging of the untreated CNT bundles results in poor contrast.

Epoxy nanocomposites fabricated from untreated CNT pulp allow the visualization of a well-dispersed CNT network via SE electron imaging. BSE imaging results in poor contrast between the epoxy matrix and the CNT network in the same sample (Figure 39a,b). Eu:Y_2O_3-CNT nanocomposites show increased contrast in both imaging modes.

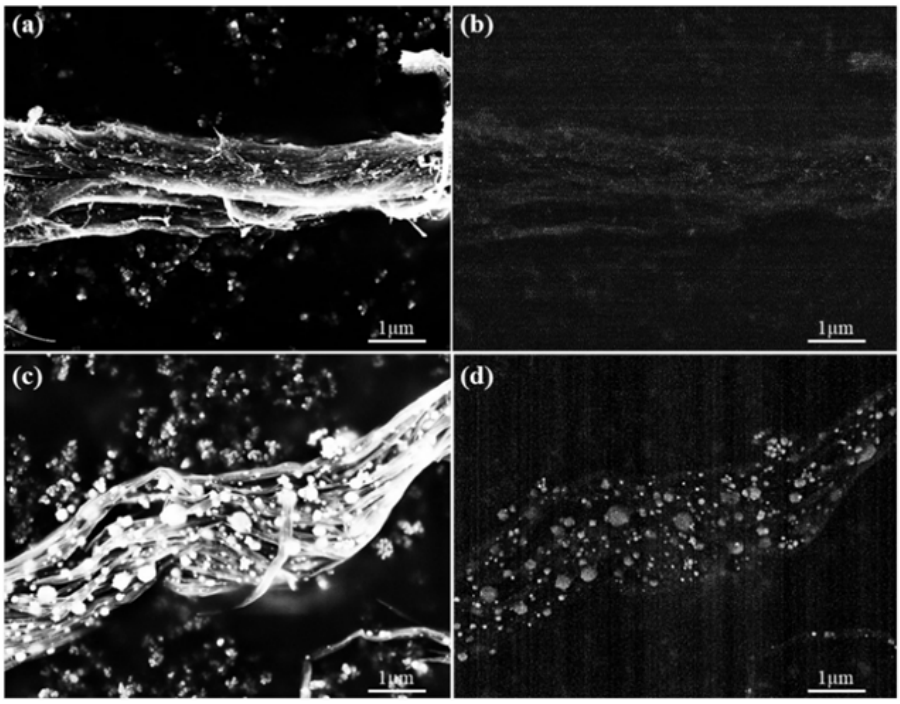

Figure 38. SEM imaging of CNT pulp: a) SE image, b) BSE image of untreated CNT pulp, c) SE image, and d) BSE of Eu:Y_2O_3-CNT CNT pulp.

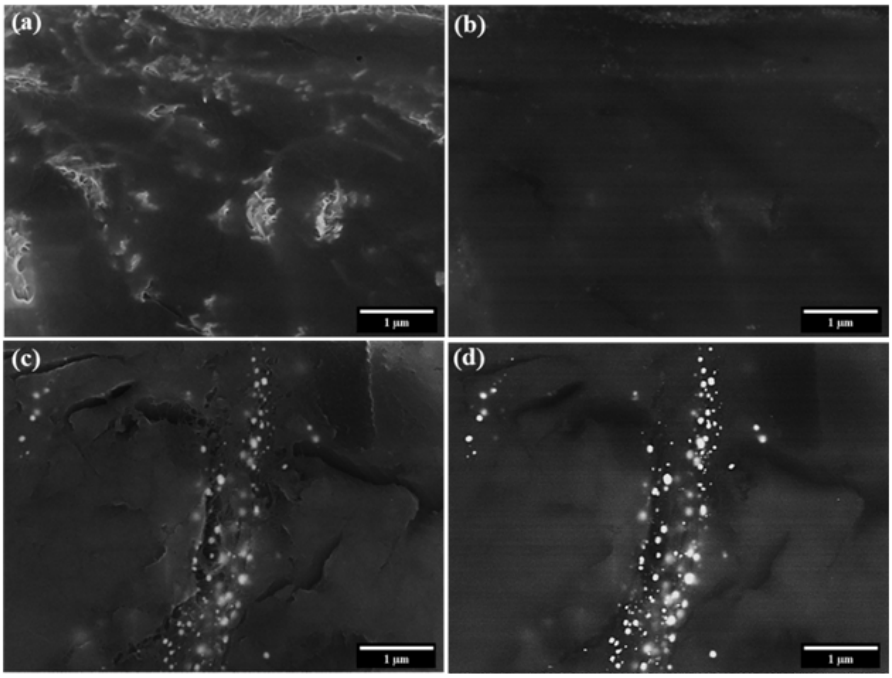

Figure 39. SEM imaging of 0.75 wt% CNT nanocomposites made from: untreated CNTs a) SE image, b) BSE image Eu:Y_2O_3-CNTs, c) SE image, and d) BSE image.

Micro-CT analysis was conducted on nanocomposites made from untreated CNTs and Eu:Y_2O_3 and generated 3D tomograms of internal porosity and CNT network. Videos featuring the 3D tomograms can be found online as supplementary files Video S1 and Video S2 for this publication . A plane-view of the captured volumes is presented in Figure 40. CNT loading was 0.75wt% in each case however, stark differences were seen between the composite with untreated CNT filler and the Eu:Y_2O_3-CNT composite (Figure 40a,b). CNT bundles were detected more readily in the Eu:Y_2O_3 sample and porosity differences were clear with average pore diameters of 113 nm and 50.2 nm for the untreated and Eu:Y_2O_3-CNTs, respectively. Image processing in Figure 40c,d allowed the pore outlines to drop out, making CNT bundle detection differences clearer. The contrast seen in the micro-CT scans corresponds to X-ray attenuation, which indicates the fraction of X-rays absorbed or scattered at each voxel. High atomic number elements such as Eu and Y attenuate X-rays more intensely compared to the epoxy matrix. Therefore, Eu:Y_2O_3-CNT manifest as high-contrast bright spots while pores in the matrix are shown as a circular outline with less intensity.

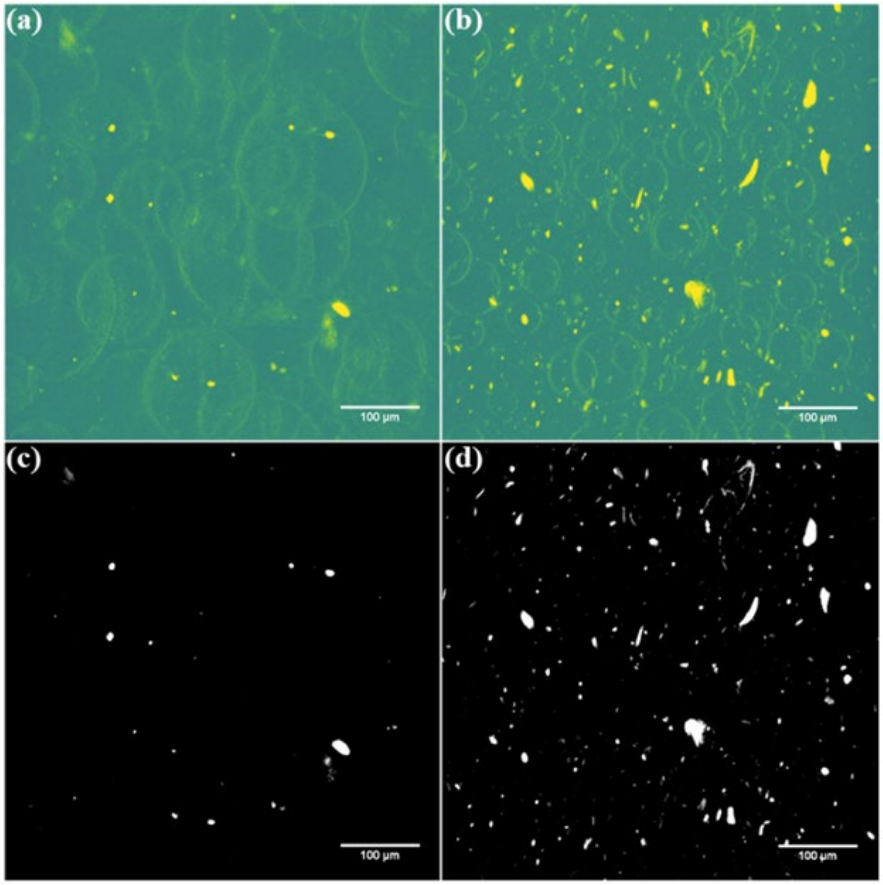

Figure 40. Micro-CT tomograms in high-contrast color revealing CNT network and pores and greyscale depicting only the CNT network: a), c) untreated CNT nanocomposite, and b), d) Eu:Y_2O_3-CNT nanocomposite.

D. CONCLUSIONS

Eu:Y_2O_3 was synthesized as distinct particles attached to CNT walls. The addition of Eu:Y_2O_3 indirectly resulted in an increase in bulk resistivity when compared to the untreated state. However, nanocomposite resistivity remained well within the required limits for its intended EMI and ESD applications.

Photoluminescence of the Eu:Y_2O_3-CNTs under DUV excitation was documented with a resulting red-orange emission wavelength of 611 nm. The utility of luminescence in relation to the Eu:Y_2O_3-CNT nanocomposite was not tested. Future work could focus on developing imaging and nondestructive techniques exploiting the photoluminescence within a cured composite.

Through this presence of heavier rare-earth elements, i.e., yttrium and europium, significant contrast improvements were realized in the SEM BSE imaging, potentially allowing the detection of tube bundles more readily and at greater depths. Similarly, the micro-CT scans benefited from Eu:Y_2O_3 inclusion and improvements to three-dimensional visualization of the CNT network through the reconstructed images resulted.

V. ELECTRICAL BEHAVIOR OF CNT EPOXY COMPOSITES UNDER IN-SITU SIMULATED SPACE ENVIRONMENTS

A. BACKGROUND

This chapter was previously published in the carbon-based nanocomposites special issue of the journal *Composites Part B: Engineering* by Elsevier [181]. The text and figures have been modified for better applicability within the chapter. All TVAC data was produced by a previous PhD candidate, CDR Brian Earp, and is included in this study for comparison.

The properties of carbon nanotube (CNT) composites have been the subject of a very large number of studies and reports. The scientific community has explored many aspects of these enthralling materials, from measuring and modeling their mechanical, optical, thermal, and electrical properties [104,163,182,183], to providing a proof of concept for a vast list of applications that could be fulfilled by their use. CNT composites could be employed as structural materials, batteries, sensors, membranes, and antennas, among others [6–9,103–105,161,163,184,185]. Due to their light weight, one of the thrust areas that is rapidly developing is the use of CNT composites in space structures and systems. Their specific strength [18], fracture toughness [12,13], fatigue resistance [14–16,186], and potentially favorable coefficient of thermal expansion [17], make them ideal candidates for space components [6–8,185]. CNT composites could also be used in charge dissipation systems and to protect against electromagnetic interference (EMI) [6–10].

The property changes that the composite materials suffer after they are exposed to actual or simulated space environments have been the subject of multiple reports. Low earth orbit (LEO) is of particular importance as the region of space where the International Space Station (ISS) and the Hubble space telescope reside [187,188], as well as a growing commercial space economy that in includes the Iridium constellation of 66 satellites [189]. The StarLink proposed constellation of 42,000 satellites [190] and Planet Labs, Inc.'s more than 150 active earth observation satellites [191], are among other future and current systems located in LEO.

Conditions found in space environments that are known to modify CNT materials include high vacuum, thermal cycles, exposure to atomic oxygen (AO), ultraviolet (UV) and other types of electromagnetic radiation, charged particles and debris [25–27]. LEO, in particular, exposes materials to AO and higher populations of debris [192]. Some of the consequences of exposure include, but are not limited to, surface erosion, fatigue cracking, loss of volatile components, and delamination [27,193]. For applications focused on charge dissipation and EMI, the changes in electrical properties of the CNT composites are of vital importance. However, reports that focus on these property changes due exposure to the space environment are scarce and do not show, to the best of our knowledge, what instantaneous variations could be expected.

The literature regarding CNT exposure to LEO includes reports for both direct and simulated space environments. Hopkins et al. [194] exposed bare CNT yarns to LEO for more than 2 years by placing samples on the exterior of ISS as part of the Materials International Space Station Experiment (MISSE-8). Their observations include chemical changes and yarn erosion in the outer 1% of the yarn but no catastrophic damage. The study found that the electrical resistivity of the samples was increased by 26.1 and 28.5% depending on the specimen's locations in the ISS. Ishikawa et al. [195] reported similar damage to the CNT yarns after being exposed to the space environment surrounding the ISS and also featured ground-based comparison tests. For the ground-based experiments, the most significant changes in the yarn's performance were related to AO exposure and the substantial reduction in material tensile strength. The electrical conductivity was not modified by exposure to UV or electron beam; however, the team did observe a decrease in resistivity, presumably associated to re-deposition of carbon species. In samples exposed to space, AO irradiation caused significant yarn damage with impacting mechanical properties, however, only minor changes were detected in electrical properties of thick yarns. CNT acid-spun yarns were treated under simulated LEO conditions by Kemnitz et al. [196]. Their observations indicate that UVC radiation did not significantly affect mechanical strength or conductivity but enhanced the piezoresistive effect. In contrast, they observed that AO severely degraded mechanical properties, with a 63.9% decrease in the yarn tensile strength and 56.3% decrease in the strain at failure. AO mildly degraded

electrical properties, causing the conductivity to decrease by 22.0%. The mechanical and electrical properties of CNT sheets treated under UVC and vacuum, as simulated LEO conditions, by Cobb et al. [197], confirmed that the effects of UVC exposure on the specimens' microstructure were minimal. In sum, it could be concluded that AO has the potential to increase resistivity of bare CNTs by 20–30%, while the absence of AO, is expected to cause only minor modifications or leave the material unaffected.

Once that the CNT are used as fillers in composites, the outlook of how their properties change as result of LEO exposure is quite different. For example, Jiao et al. [28] studied the AO exposure behavior of CNT epoxy composites, finding that CNT bundles tend to collapse and that porous CNT films present higher levels of erosion than dense counterparts. They also report a decrease in the material tensile strength (16.3% reduction) and electrical conductivity (approx. 30% reduction). The adverse effects of diverse environments, including LEO, in CNT/polymer interfaces were also studied by Prusty et al. [29] The behavior of other carbon composites, such as graphite/epoxy, under simulated LEO settings have shown similar results; the work by Han et al. [198] showed considerable damage to the surface of the composites along mass erosion and reduction of tensile strength due not only to AO, but to the synergistic effects of LEO space environment constituents (AO, UV radiation, thermal cycling).

Reports regarding CNT composites includes work aimed to improve the materials resistance to degradation under LEO conditions. For example, Awaja et al. [199] performed simulated LEO treatments in various carbon epoxy composites, including CNT, and determined the effects that using different reinforcements had on the surface degradation mechanisms of the materials. The experimental conditions used included high vacuum, UV radiation and thermal cycling, the latter employing a halogen lamp and AO generated by a radio frequency power source. The main findings relate to samples with fillers presenting higher oxygen levels and less erosion than the bare epoxy resin. No electrical properties were examined. Atar et al. [200] fabricated flexible and electrically conductive polyimide nanocomposite films using CNT sheets. Their study shows that the incorporation of polyhedral oligomeric silsesquioxane monomer increases the durability of the composites

exposed to ground-based AO environments without compromising their electrical conductivity.

The present study focused on characterizing the instantaneous changes in electrical properties of epoxy composite specimens containing 0.014, 0.2 and 0.75 wt% of CNT while the samples were subjected to the temperatures, pressures and sunlight exposure that will be expected in LEO conditions. Each of the CNT loadings selected present a different order of magnitude resistivity, thus, prompting an independent in-situ analysis. The increasing number of systems located in LEO, and our dependence on their functionalities for advanced communications, global internet services, and earth observations, among others [201], make the subject of this manuscript significant since the results presented inform the community of their expected behavior.

B. EXPERIMENTAL METHODS

1. CNT Composite Fabrication

The composites studied herein were generated using multiwall carbon nanotubes (MWCNT) acquired from Nanocomp Technologies Inc (Huntsman Corporation, Merrimack, NH, USA) and Henkel Loctite Hysol EA9396 Aero Epoxy (Henkel Corporation, Dusseldorf, Germany). A chemical vapor deposition process using Fe as catalyst was employed to generate large CNT sheets. The sheets, presenting electrical conductivities in the order of 3.2×10^4 S/m (resistivity of 3.125×10^3 Ohm-cm) [202], were then converted into a pulp using a Hollander Beater and industrial burr mill [203]. The CNT were used as received, as pulp/bundles of approximately 0.05 mm diameter and 1 mm in length, with individual nanotube diameter of approximately 30 nm and Fe catalyst nanoparticles dispersed throughout the sample.

The epoxy resin used was a two-part system consisting of resin and hardener, in a manufacturer's recommended mixing ratio of 100:30 by weight. The epoxy system employed is known to have a tensile lap shear strength of 27.6 MPa and a tensile strength of 35.2 MPa at 25 °C when cured for 1 h at 66 °C. The viscosity of the epoxy at 25 °C is 700 Poise for Part A, 0.9 Poise for Part B and 35 Poise for their mixture. The electrical resistivity of the base epoxy mixture is reported to be 2.14×10^{15} Ohm-cm [56].

The resin and the proper amount of CNT to generate the loadings of interest (0.014, 0.2 and 0.75 wt% CNT), were mixed using a FlackTek (Landrum, SC, USA) asymmetric speed mixer operating at 1200 rpm in the first 2 min mixing cycle, at 2500 rpm for 1 min and three subsequent 1 min cycles at 3000 rpm. Vacuum was applied in between mixing cycles to remove air pockets and minimize porosity. The application of vacuum in between mixing cycles also served as a cooling period since the mixing cycles cause the specimen's temperature to increase. Once the CNTs were dispersed in the resin, the hardener was added in a single mixing step. While still in a viscous state, the resin-CNT-hardener mixtures were deposited in an electric board that had a prefabricated pattern of 4 conductive traces to later conduct the electrical measurements. The samples were cured at 66 °C for 1 h using a Binder convection oven (Binder GmbH, Tuttlingen, Germany).

2. Simulated Space Environment

The CNT epoxy composites were exposed to three different environments while their electrical resistivity was measured: a) Tenney thermal vacuum (TVAC) chamber, b) solar simulator and c) convection oven. The first experiment, conducted in the TVAC chamber, was meant to provide similar pressure and temperature conditions to the ones encountered in LEO. The solar simulator was used to mimic the exposure of the specimens to sunlight; thus, the samples electrical properties were measured as a function of irradiance and the temperature increase associated with it. The third set of experiments were conducted inside a convection oven as an attempt to understand the isolated effects of temperature on the composite's resistivity without the influence of pressure or light featured in the other two sets of experiments.

3. Tenney Thermal Vacuum Chamber (TVAC)

A TVAC chamber Model 3.5D3-LN2-VTV-G (Tenney Environmental, New Columbia, PA, USA) was employed to subject the CNT composites to pressures and temperatures close to those normally encountered by space systems in LEO. The TVAC system consisted of a stainless-steel vessel operating under high vacuum, with pressures down to 1×10^{-7} Torr [1.3×10^{5} Pa]. Liquid nitrogen was employed to allow the samples to be cooled, thus, enabling experiments to be carried out in temperatures from -60 °C to

150 °C. Connector pass-through cables were used to collect electrical resistivity data, as shown in Figure 41. Each of the CNT composites studied (0.014, 0.2 and 0.75 wt% CNT) were tested independently. Two of the loadings were measured twice to verify the run-to-run variation. Resistivity data for multiple temperature points was collected using currents from 5 to 500 μA. For reference and comparison, the pressures encountered at diverse elevations are included in Table 9 [204].

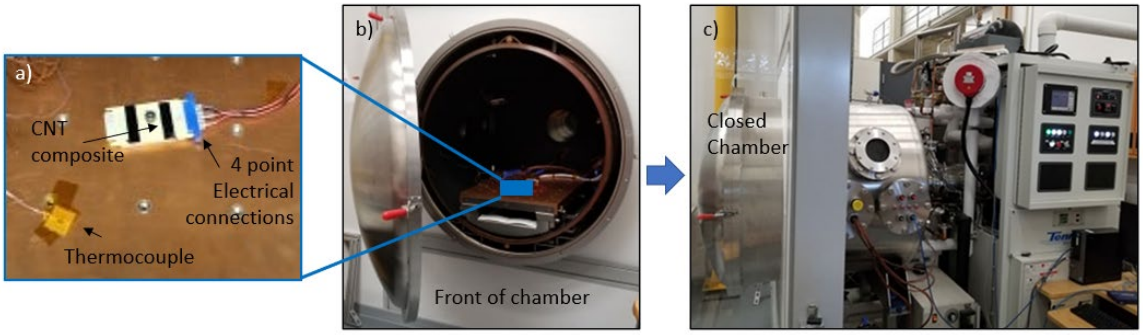

Figure 41. TVAC configuration, a) CNT composite electric board and thermocouple, b) front of the chamber and sample placement, and c) exterior side-view.

Table 9. Altitude pressure conversion. Adapted from [204].

Altitude (Feet)	Sea	1000	5000	50,000	100,000	200,000	300,000	500,000	600,000	700,000
(km)	Level	0.3	1.5	15.2	30.5	61.0	91.4	152.4	182.9	213.4
Pressure (Torr)	760	733.0	632.5	87.38	8.28	0.169	7.99E-4	1.35E-5	1.76E-6	9.02E-7
(Pa)	1.0E5	9.8E4	8.4E4	1.2E4	1.1E3	2.3E1	1.1E-1	1.8E-3	2.3E-4	1.2E-4

4. Solar Simulator Exposure

An OAI TriSOL 300 mm class AAA solar simulator (Optical Associates Inc., Milpitas, CA, USA) was employed to produce similar conditions than the ones encountered by direct sunlight exposure. Solar simulation light sources of the type employed produce an intense, uniform, collimated beam of broad band energy. The instrument uses a xenon arc lamp to produce the radiation, which is collected by a reflector and directed to an aluminum mirror. The beam then converges onto the optical integrator and the exit beam

diverges through the open shutter to the second mirror, where it is reflected through the collimating lens onto the exposure plane. The xenon lamp provides standard sunlight simulation from UV to infrared (IR) in accordance with ASTM E927-5 and ASTM E490. Figure 42 presents the irradiance graph taken for the instrument covering wavelengths from 330 to 1800 nm; the measurement was performed at 1000 W/m^2 at 25 °C with a lamp current of 82 A. The spectral irradiance wavelength distribution for air mass at global spectrum and zero atmosphere, (AM1.5G and AM0, respectively) are also plotted for reference.

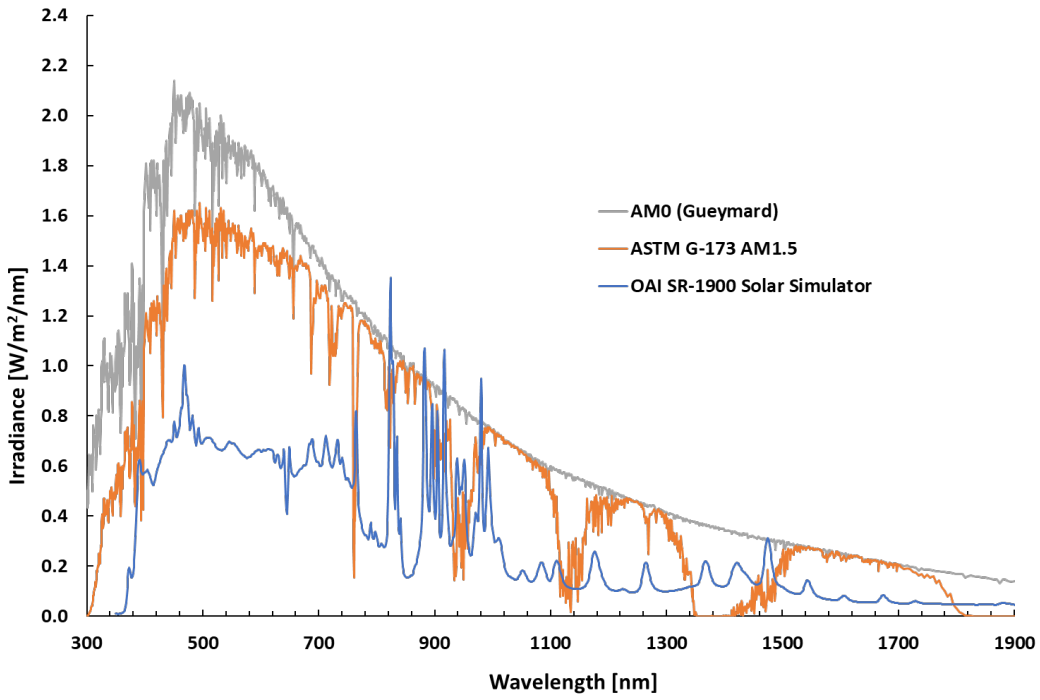

Figure 42. Measured irradiance for the solar simulator instrument employed in the study with irradiances AM0 and AM1.5 shown for comparison. Adapted from [205–207].

An OAI 306 UV Power meter (Optical Associates Inc. Milpitas, CA, USA) was used to determine irradiance in mW/cm2 received by the composite specimens for the duration of every experiment. These values are plotted on the secondary axis in the results section (Figure 48). Figure 43 shows the physical arrangement of the samples for the test. Figure 43a illustrates the placement of the sample in the central region of the simulator

exposure plane. It is worth noting that 2 strips of composite are exposed while only one has been soldered to the set of 4 cables for the 4-point resistivity measurements. The source meter was placed at a separate table, its description is included in Section 2.4. Two T-type thermocouples (Omega Engineering, Inc. Norwalk, Connecticut, USA) were employed to measure temperature, one placed on top of the composite and one in direct contact with the high-performance laminar flow isolator that served as substrate. The power meter was located within an inch of the composite's electric board (see Figure 43b). Figure 43c shows the simulator during operation, with an open shutter.

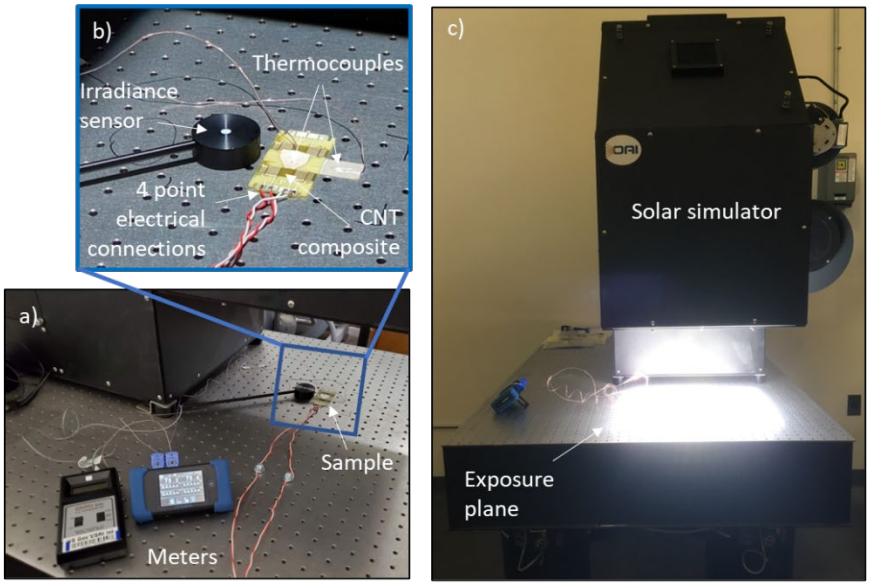

Figure 43. Solar simulator setup, a) sample placement, b) meters employed, and c) image of the exposure plane and instrument with shutter open.

5. Convection Oven

The electrical properties of the CNT specimens were also measured inside a convection oven under two different conditions to replicate the temperature range and heating rates experienced by the TVAC and solar simulator datasets. For the TVAC comparison, oven temperatures varied from 25 to 150 °C in 10 °C intervals with dwell stabilizing periods in between each step increase. To compare with the solar simulator data, heating in the oven took place from 25 to 90 °C, using a continuous temperature increase

until the sample reached the maximum temperature. The same Binder convection oven (Binder GmbH, Tuttlingen, Germany) used for curing the specimens was employed to collect resistivity data as the sample was heated. Figure 44 shows the sample placement and the experimental setup.

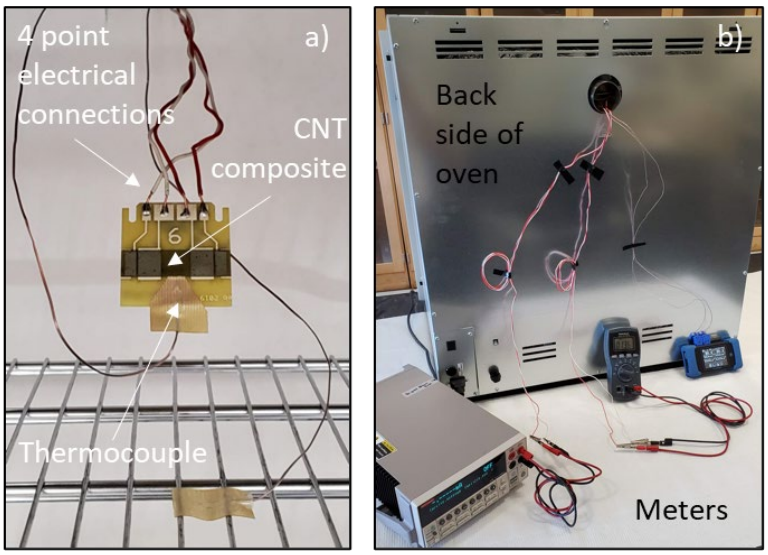

Figure 44. a) CNT composite board location inside oven and b) meters and cables employed to conduct 4-point resistivity measurement and corroborate temperature at the board.

6. Materials Thermal and Microstructure Characterization

The cured CNT epoxy samples were analyzed in a Simultaneous Thermal Analyzer (STA) 449 Jupiter F1 (Netzsch GmbH & Co. Holding KG, (Selb, Germany) to determine if the specimens suffered changes in mass as the temperature increased. The data was collected from room temperature to 150 ◦C with a heating rate of 1◦/min under ultra-high purity Argon atmosphere (Ar-UHP) flowing at 100 ml/min. A Zeiss Neon 40 (Zeiss, Oberkochen, Germany) Dual Beam Scanning Electron Microscope (SEM) operating between 1 and 20 KV was used to determine the microstructural features of the CNT bundles and the distribution of the same along the Fe catalyst in the epoxy resin. A Nikon Epiphot 200 reflective optical microscope (Nikon, Tokyo, Japan) was employed to observe the surface porosity of the cured composite samples.

7. Electrical Measurements

The four-point circuit boards were analyzed using a 2400 Keithley Source Meter (Tektronix, Inc., Beaverton, OR, USA) as the current source and a digital multi-meter to measure the voltage drop across each sample for various applied currents. Using sample thickness, the resistivity of each sample was calculated. For the data reported herein, we focused on the resistivity that resulted from the application of 400 μA. To determine if the electrical properties effects observed in the samples were permanent or what changes could be expected when the specimens get exposed again to atmospheric conditions, their resistivity was measured immediately after each test, after one day and after multiple days from the time when the original experiment was conducted.

C. RESULTS

1. Electrical and Microstructural Analysis of CNT and CNT Composites under Atmospheric Conditions

To understand the significance of the changes in the electrical data observed under simulated LEO conditions for each of the CNT loadings studied, it is indispensable to first describe their microstructures at the nanometer level and the relationship of those with their electrical conductivity at atmospheric settings. The CNT loadings employed were targeted to include extremely low amounts of CNT (0.014 wt%) and a couple of compositions with low loadings (0.2 and 0.75 wt%). Such selection allowed the characterization of the behavior of specimens below and above electrical conductivity percolation limits, respectively, observed in prior work [5,107]. The resistivity of the CNT epoxy composites at 760 torr and 25 °C, is expected to be in the 2×10^3 to 10×10^3 Ohm-cm range for 0.014 wt% CNT, 50 to 200 Ohm-cm for 0.2 wt% CNT and 16 Ohm-cm or less for 0.75 wt% CNT. The standard deviation in the data presented in the figure was calculated from the analysis of 8 different electric board samples. The resistivity range mentioned includes the lot-to-lot variability. Figure 45 presents the electrical resistivity for composites with CNT loadings from 0.014 to 2 wt%. Some of the resistivity trends below 300 Ohm-cm could be appreciated in the inset graph. The SEM observation of the microstructural features for two compositions (0.014 and 0.75 CNT wt%), acquired from the epoxy-CNT composites

polished surfaces, is presented as well, along a schematic representation of the conductive networks identified. For the SEM images, the bright areas correspond to the CNT embedded bundles. In the accompanying pictogram, the grey areas represent the locations of the composite densely populated by CNT, where electrons are expected to have high mobilities, while the blue regions represent insulating areas, where the epoxy is devoid of CNT. It is worth noting that the scale bar for each image is quite different: 10 μm for the 0.014 CNT wt% sample and 1 μm for the 0.75 CNT % specimen. The striking differences in resistivity as a function of filler loading are associated with the microstructural features: The absence of a conductive network in samples with 0.014 wt% CNT promotes a capacitor-like behavior. In contrast, the samples with 0.2 and 0.75 wt% CNT, despite containing regions devoid of CNT, form a tridimensional web of interconnected nanotube conductors within the non-conductive polymeric matrix, thus, exhibiting the expected resistor behavior. Detailed analysis of the conductive mechanisms in these composites, and some of the variables that influence them, can be found in [50,51].

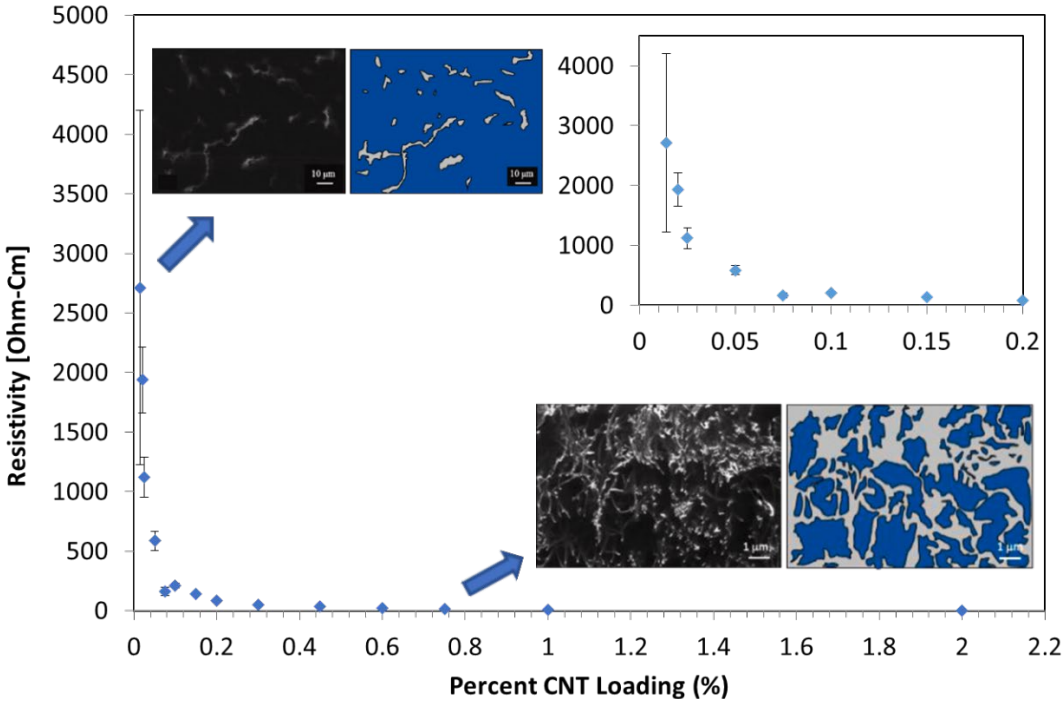

Figure 45. Epoxy - CNT composite resistivity as a function of CNT loading in wt% along with SEM micrographs taken from two samples with CNT regions marked in white on the corresponding pictogram.

Figure 46 presents SEM micrographs in which bare CNT bundles could be appreciated (6a) and where the individual diameter and presence of Fe catalyst nanoparticles is evident (Figure 46b). Figure 46c and d illustrate the microstructure of the 0.75 wt% CNT epoxy composite, showing the CNT distribution within the polymer at 10,000x and 20,000x, respectively. It is worth noting that these images show CNT at the surface of the composite as well as CNT strands that are embedded in the matrix, forming a connected network that extends in all directions. As previously mentioned, it is believed that the existence of such intertwined CNT web is responsible for the electrical conductivity of the composite.

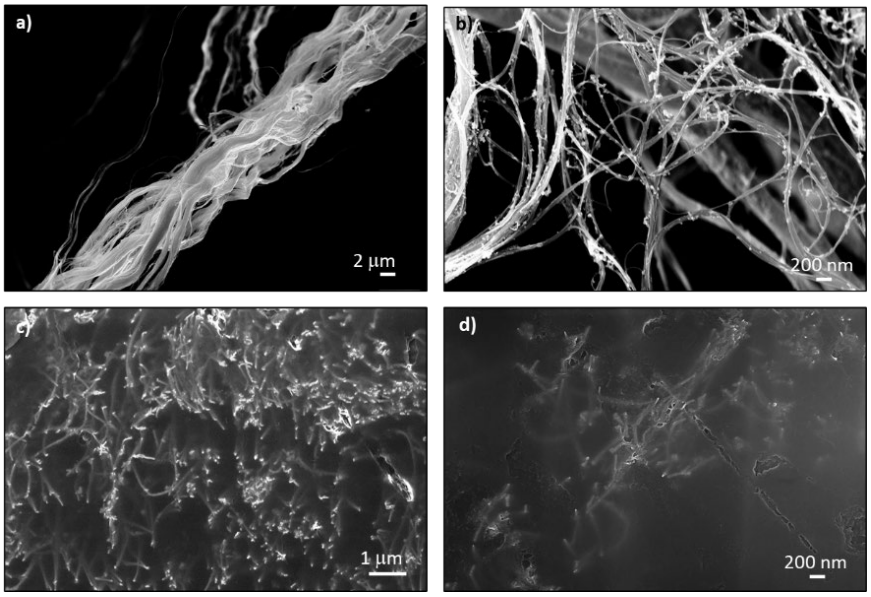

Figure 46. a) and b) SEM micrographs of CNT pulp at different magnifications, c) and d) distribution of CNT network within the epoxy composite for a specimen containing 0.75 wt% loading showing the conductive CNT tridimensional network.

2. TVAC Environmental Chamber

The resistivities observed as function of the low pressure and temperatures of the TVAC are presented in Figure 47. The electrical behavior of the samples for the three loadings seemed practically unaffected at sub-ambient temperatures combined with low pressure. The graph presented in Figure 47a shows an almost constant value of resistivity

as the samples transition from -60 to 25 °C. The order of magnitude of the resistivity for each sample was within the expected values reported in Section 3.1. All the specimens exhibit a slight resistivity uptake followed by a significant reduction after the temperature surpasses 40 °C, with larger changes occurring between 70 and 110 °C and higher temperatures. Figure 47b presents the normalized resistivity, assuming that the original reading for each filler loading is equal to 1. The samples with the lower loadings, 0.014 and 0.2 wt% CNT suffer the largest alteration, with reduction in resistivity of approximately 40% of their original values. The sample with 0.75 wt % displays only a reduction of 20%. Since most of the interest in these materials in space systems derives from their electrical conduction, the trends observed here are not expected to compromise their functionality but to improve their behavior.

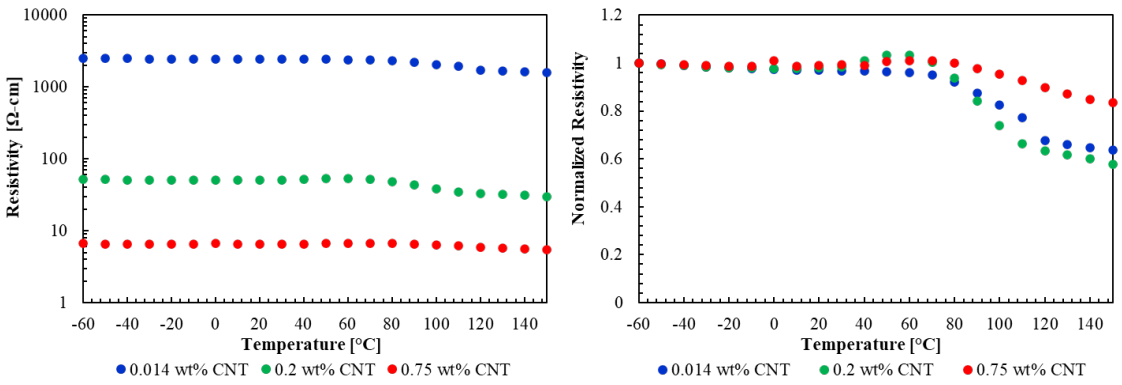

Figure 47. TVAC measured resistivity, a) logarithmic scale, and b) normalized for comparison of change within CNT loading regimes.

3. Effects of UV Radiation (Solar Simulator)

The exposure of the samples to light produced by the solar simulator showed similar electrical behavior tendencies than the one observed for the TVAC experiment; an overall reduction in resistivity is observed as the time of exposure and temperature increased. The magnitude of the changes in resistivity in this case, is quite significant, with reductions of 48, 58 and 41% for the samples with 0.014, 0.2 and 0.75 wt% CNT, respectively. It is worth noting that the temperature of the samples increases asymptotically over time once the irradiance stabilizes as illustrated in Figure 48.

In addition to the temperature effects, these samples experienced the exposure to electromagnetic radiation, which is known to produce an increase in the number of charge carriers, with the associated decrease in resistivity. The observed changes in the resistivity of the composites during their exposure to radiation in the UV, visible light, and IR ranges, does not seem to follow a trend with respect to the CNT loading. The samples seem to be more susceptible to the level of porosity and surface characteristics than to loading, as the mass loss analysis presented in Section D.1 will further address.

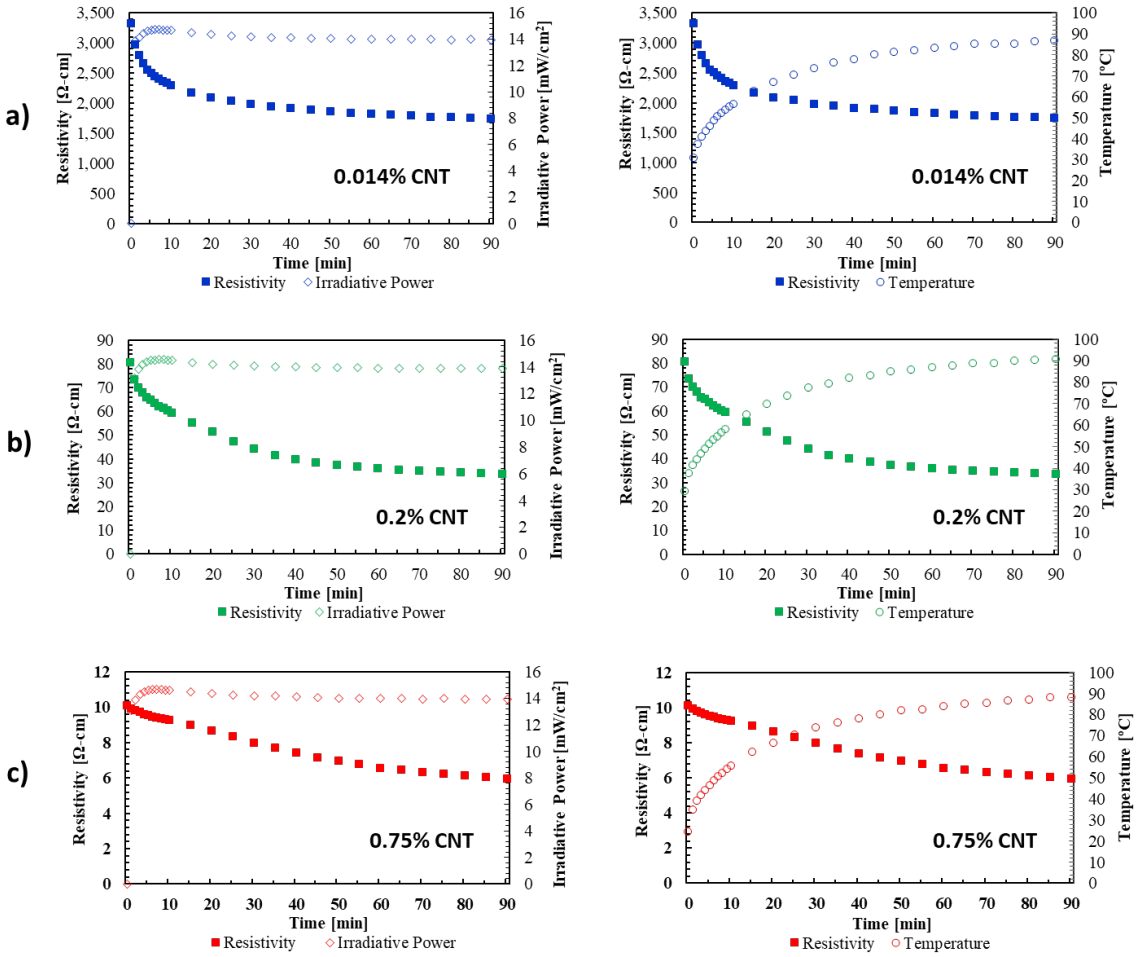

Figure 48. Resistivity as a function of time exposed to simulated sunlight for a) 0.014, b) 0.2, and c) 0.75 wt% CNT loadings. Left: including irradiance measured during exposure. Right: including the increase in temperature generated as result of the sunlight exposure.

4. Thermal Effects (Convection Oven)

As previously mentioned, the experiments in the convection oven were meant to isolate the effect that temperature, as a single variable, had in the composite material's electrical properties. The curves generated are presented in Figure 49. The resistivity of the samples seems to stay at the original value until the samples reach approximately 70 °C. After that, the temperature tends to increase logarithmically while the resistivity experiences exponential decay. It is worth noting that a small reduction of resistivity is still observed after the samples reach the maximum temperature. The specimens undergo a resistivity reduction of 21.4, 40.87 and 26.3% for samples with 0.014, 0.2 and 0.75 wt% CNT loadings, respectively. Thus, the oven samples suffered modest changes when compared to those seen for irradiance exposure over time in the solar simulator. In contrast, the electrical properties recorded in the oven from room temperature to 150 °C at atmospheric pressure, are similar to those experienced in the TVAC under high vacuum and up to 150 °C. Only the oven sample with 0.2 wt% CNT shows a more dramatic change. The mechanisms suspected of affecting composite resistivity are further discussed in the next section.

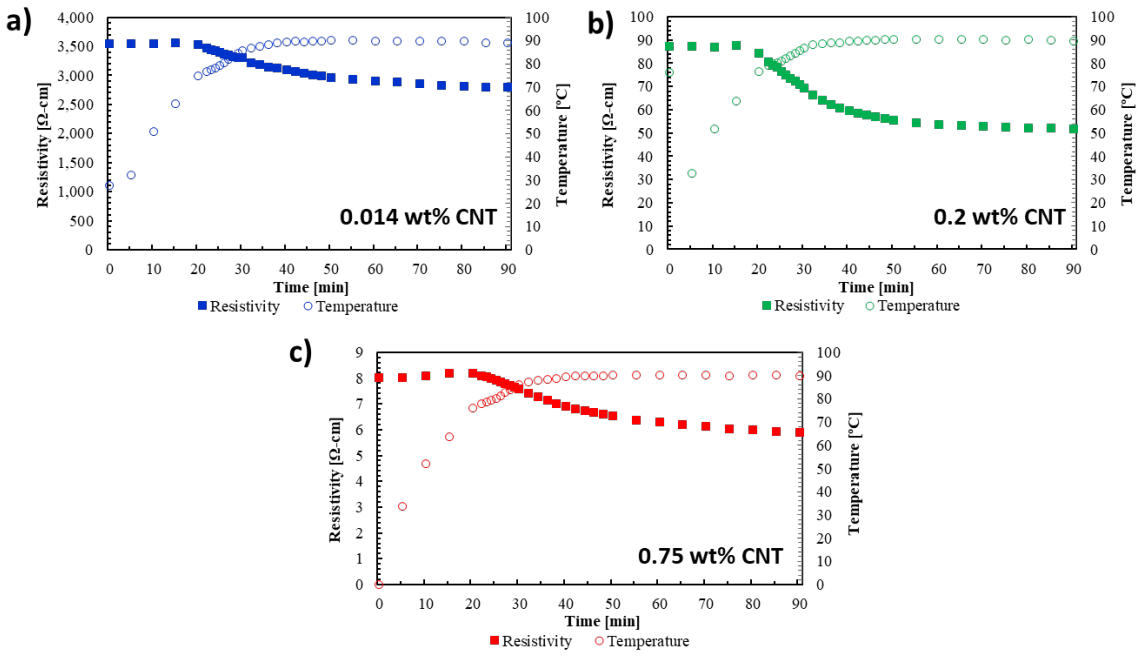

Figure 49. Resistivity and temperature as a function of time when heated to 90 °C for a) 0.014, b) 0.2, and c) 0.75 wt% CNT loadings.

5. Long-term Low-Vacuum Exposure

As a parallel study, pristine composites were stored at sub-ambient pressures (114.76 Torr) in a Pelco 2251 vacuum desiccator chamber (Ted Pella Inc. Redding, CA, USA) and their resistivities recorded over time. Resistivity reductions were negligible for the first day, however, the effect of the low pressure becomes more evident with time, reaching reductions of 0.20, 24.6 and 5.67 % for the 0.014, 0.2 and 0.75 wt% CNT composites, respectively, after 20 days. Such results demonstrate that not only high vacuum, but simple sub-ambient pressures, are enough to produce a change in properties and serves as evidence that loss of moisture and other absorbed gases or volatile components from the epoxy resin might be occurring. The differences between the desiccator and TVAC indicate that outgassing of moisture absorbed by the CNT and/or the epoxy matrix could occur to a small extent under pressures below atmospheric and be exacerbated as the temperature increases or pressure decreases. Section 4 below includes the thermogravimetric analysis and further discusses the root cause of the electrical properties' fluctuations detected.

D. DISCUSSION

1. Electrical Properties Measured In-situ

Figure 50 presents a comparison of the magnitude of the changes in the composites resistivity for each setting described. The data has been normalized, for all loadings studied, to the resistivity value at starting temperature for a) oven and solar simulator and b) TVAC chamber. It is worth noting that each graph contains convection oven data and that each experiment used a different heating rate to mimic, to the extent possible, the conditions imposed by the solar simulator or the TVAC. When the effects of temperature in oven are contrasted with those of the combined temperature and exposure to simulated sunlight in Figure 50a, it becomes evident that the combined irradiance and concomitant surge in temperature have the greater influence in the instantaneous changes in resistivity than temperature by itself. For TVAC (Figure 50b), low temperatures (-60 to 25 °C) and low pressures (up to $1 \times 10–^{7}$ Torr) did not seem to modify the electrical performance (see Figure 47), only higher temperatures result in significant resistivity reductions, thus the data here is only compared from 25 to 150 °C. From Figure 50b, the oven experiment rendered a larger change in the resistivity than the TVAC. The location of the thermocouples in each experiment might provide a possible explanation; In the convection oven, the composite, and the overall volume of air inside the oven is at the setpoint temperature, while in the TVAC it is only the platen what is being heated. That is, the temperature imposed by the TVAC must travel from the platen that acts as substrate, to the electric board (with thermally insulating backing) and finally to the composite. Thus, it is believed that in the oven, the samples experience a more consistent heating process, which might produce higher localized temperatures, exacerbating its effects. Another observation from Figure 50a and b, is that the 0.2% sample exhibits larger variation than other loadings under all conditions.

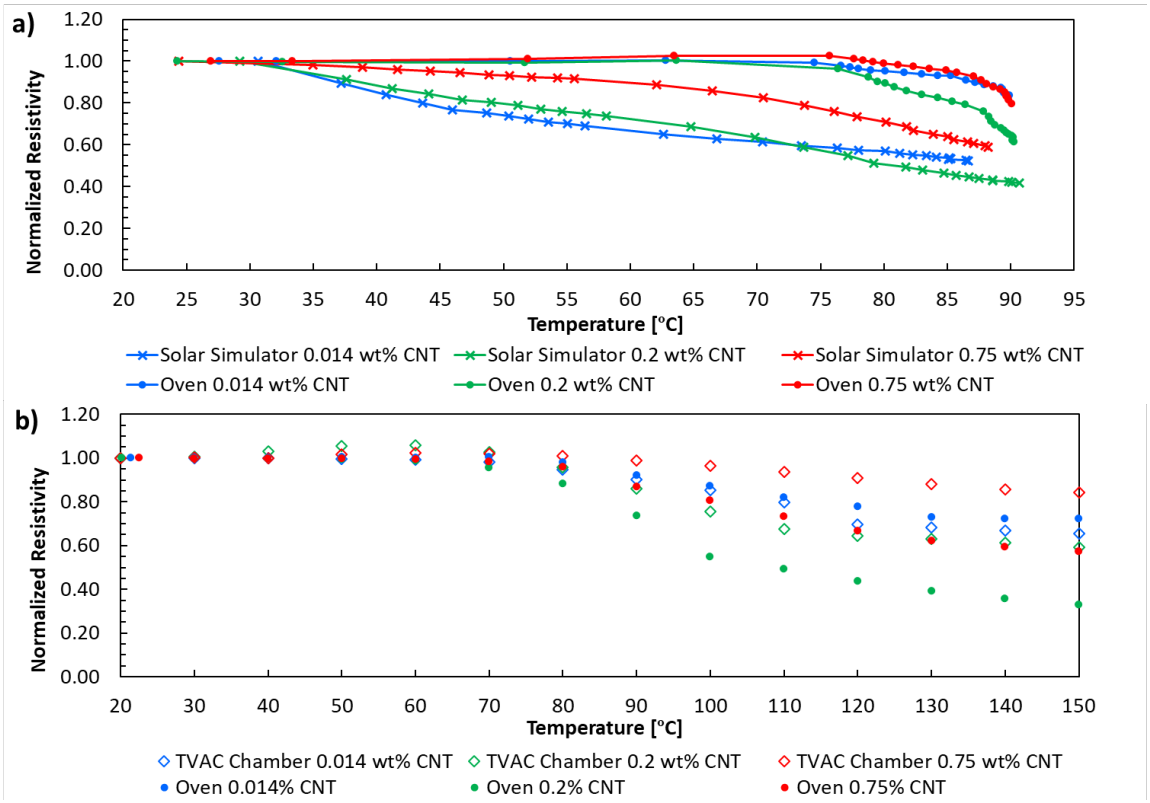

Figure 50. Comparison of resistivity response to temperature changes caused by a) Simulated sunlight exposure vs. convection oven and b) TVAC chamber vs. convection oven.

In all cases, the in-situ changes measured showed a significant decrease in the samples resistivity (increased conductivity), a factor that should be acknowledged as systems containing these composites are exposed to LEO conditions.

Several factors have been shown to impact electrical conduction in CNT composites at elevated temperatures. These include temperature dependent properties of the composite matrix material, differences in thermal expansion of components making up the matrix, thermal activation of charge carriers at elevated temperatures/thermal fluctuation induced tunneling, and interactions with the atmosphere [208,209]. The data collected and presented here seems to follow a similar tendency as those studies and puts in evidence that the property changes result from the instantaneous exposure and continue over time. Thermal induced tunneling proposed by Sanli et al. [210] and Sheng et al. [211], could apply to samples above percolation limit (0.2 and 0.75 wt% CNT in this work),

however, it won't be responsible for the temperature effects seen in the 0.014 wt% CNT sample, where the separation between CNT strands is in the micrometer range. The exposure to light might have an independent effect since the overall magnitude of the changes in the solar simulator seem to be greater than those observed at the same or even greater temperatures in the TVAC or in the oven experiments. Light effects in semiconductors are similar to heat effects. In both cases, free electrons are generated with the concurrent reduction in resistivity. Reducing the pressure or increasing temperature seem to also produce outgassing. The analyses of the samples by thermogravimetry confirms that the application of temperature is accompanied by a reduction in mass as shown in Figure 51. The 0.014, 0.2 and 0.75 wt% CNT epoxy composites show 2.51, 5.23 and 3.01% mass reduction, respectively. The bare epoxy (no CNT), Aero 9396 Loctite, recommended for space applications due to low off gassing, showed a mass loss of only 1.26%. The bare CNT pulp employed, containing still the Fe catalyst, showed a mass loss of 4.56%.

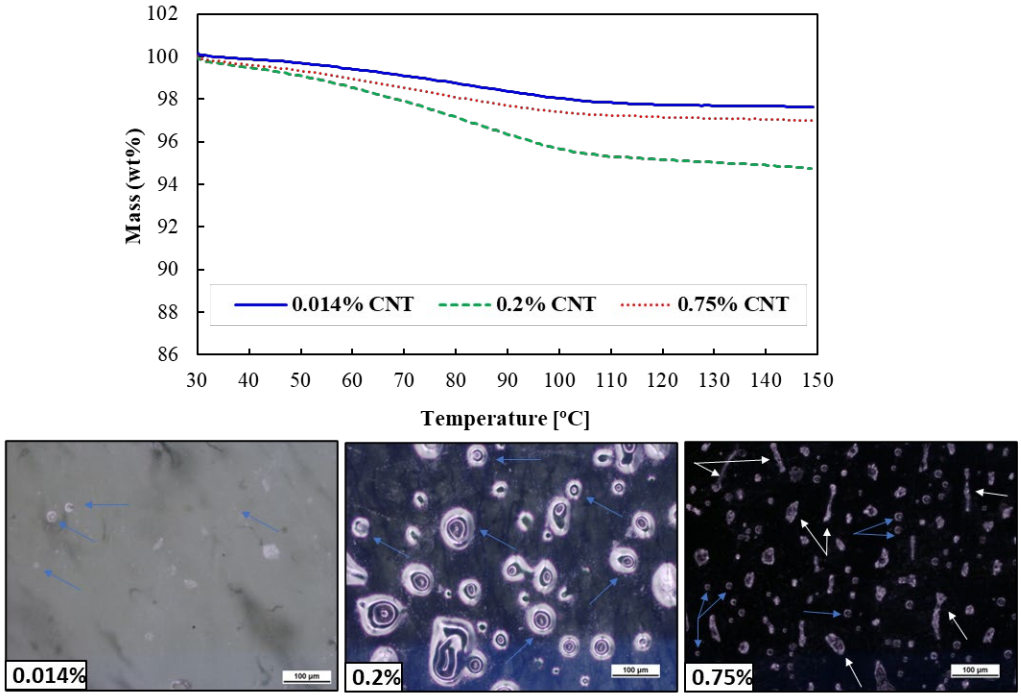

Note: scale in images 100 µm.

Figure 51. Top: TGA analysis of the 3 composites studied. Bottom: optical microscopy images illustrating differences in porosity.

To understand why the sample with 0.2 wt% CNT lost more weight, the surface characteristics of all the composites were studied under an optical microscope. Despite all samples being produced under similar conditions, the sample with 0.2 wt% CNT presents a large amount of surface pores (Figure 51b), not only are those of much larger dimensions (up to 100 µm) than the ones observed in the other two samples (Figure 51a and c), their number far exceeds that of the other samples. The larger surface area produced by the porous surface could explain a greater tendency to absorb moisture that is lost during the heating cycles. In the images presented in Figure 51 exemplary pores are marked with blue arrows. The white arrows in the sample that contains 0.75 wt % CNT represent areas of the sample where CNTs are located at the surface. The pores take on a spherical shape in all cases, while the CNTs are shown as strings or irregular shapes and are only notable in the 0.75 wt% sample. Differences in the composite fabrication process, such as the level of applied vacuum prior to curing, possible air inclusion during addition of hardener, and time employed to create the conductive film could result in microstructural differences of the

resulting epoxy. Larger loading percentages are prone to porosity issues due to the increased mixture viscosity and are especially susceptible to slight differences in preparation technique. Density differences of as much as 4.1% have been found for the same loadings due to differences in preparation procedures and could account for the differences seen via thermogravimetric analysis and optical microscopy.

2. Recovery of Electrical Properties in Atmospheric Conditions

Since the current study focused on the instantaneous electrical behavior of CNT epoxy composites during their exposure to LEO approximate temperatures, pressures and sunlight, no data is presented regarding their behavior after prolonged periods of exposure. However, there was still interest on what the immediate changes will be if the composites were returned to atmospheric conditions. The samples were stored in polyethylene vials at room temperature and pressure and their resistivity measured on the days following removal from the test environment. Figure 52 presents the data collected before, after, and 20 days following temperature and UV testing.

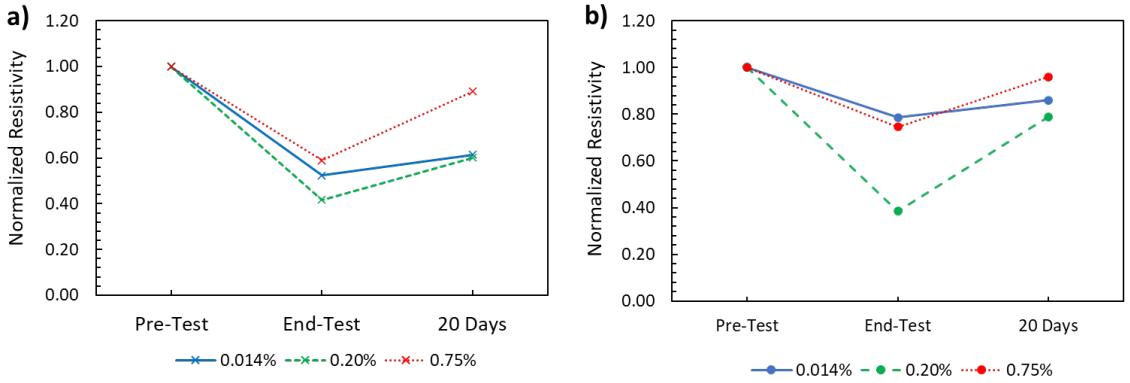

Figure 52. a) resistivity values pre- and post-solar simulator exposure, and b) resistivity values pre-and post-convection oven experiment.

As described in detail in previous sections, a resistivity decrease (conductivity increase) is observed for all the environments studied for all the CNT loadings. The resistivity after one day back to atmospheric conditions tends to remain at the same decreased values or suffer a minor increase. Mohiuddin et al. also noted lower resistance

values in samples that were previously been subject to high temperatures, as reported in their study of the electrical resistance with increasing temperature for CNT-polyether ether ketone composites with CNT loadings between 8 and 10 wt% [212]. In the present study, after one week of the original experiments, the resistivity is greater but not quite back at the values recorded before the experiments under simulated environments were conducted. The result is significant since it shows that the species that originally outgassed from the samples, could be easily re-absorbed after a few days and that the temperature effects are, until a certain extent, reversible.

Such upturn in resistivity was also confirmed by heating pristine samples in the convection oven at a set temperature for 4 h and exposing them back to the laboratory atmosphere (see Figure 53). The figure illustrates how the magnitude of resistivity reductions are proportional to the heating temperature for the same time of treatment. Those heated only to 50 ◦C had modest changes, while the samples heated at higher temperatures present a more significant relative change. Both the 0.014 and 0.75 wt% CNT samples showed resistivity values trending back to their original state after one week in atmospheric conditions. When comparing the trends between Figure 52 and Figure 53, it is clear that the samples that were simply heated using the oven returned to the original values much faster than those that were also exposed to sunlight.

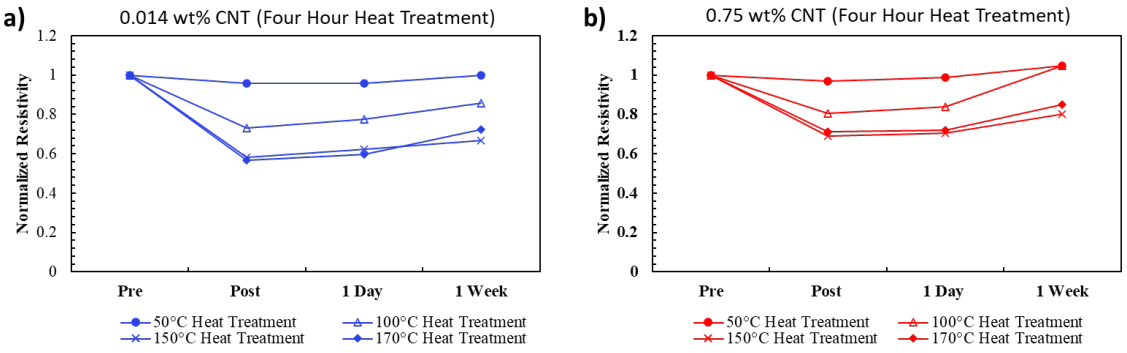

Figure 53. Pre- and post-heat treatment resistivity values for a) 0.014 and b) 0.75 wt% CNT.

It is expected that if the systems that contain these composites are exposed back to atmospheric conditions, as is the case in the reuse of some of the systems, their electrical properties will experience some level of recovery, as seen herein. A possible explanation of why the original values were not completely reached, might be that not all the volatiles initially lost are present in the atmosphere, some might be associated with the polymeric matrix components and thus, can't be reabsorbed by the sample surface. Moreover, the composite surface finishing will also have an impact on the extent of the changes observed.

E. CONCLUSIONS

The instantaneous changes in electrical properties of CNT epoxy composites containing low CNT loadings (less than 1%) were measured while the specimens were exposed to diverse simulated space conditions. A thermal vacuum chamber, solar simulator, and a convection oven were employed to produce approximate pressures, temperatures, and light conditions associated with low earth orbit. Increasing temperature above 60 °C under high vacuum will produce an instant reduction in resistivity of at least 20%. Exposure to simulated sunlight can have major impacts in the electrical behavior, promoting a surge in temperature and causing resistivity reduction up to almost 60% of the original values. All observations are consistent with mass loss due to volatile species outgassing, and the generation of extra charge carriers as result of UV/visible/IR light exposure. Surface porosity plays a critical role in the specimen's resistivity under all conditions studied. The latter seems to be more impactful than loading values when the CNT content is less than 1%. To a large extent, the changes in electrical properties observed were reversed after the specimens were returned to atmospheric conditions.

THIS PAGE INTENTIONALLY LEFT BLANK

VI. SUMMARY AND CONCLUSIONS

This section reestablishes the objective for this accumulative body of work and summarizes the results of preceding studies by answering questions were proposed at the beginning of the dissertation.

The objective of the research contained in this dissertation was to further the understanding of the electrical properties of CNT-based epoxy nanocomposites and how these properties change through production, can be validated after formation, and respond under operating conditions. These materials are targeted for EMI and ESD applications within the aerospace industry where the composite's electrical resistivity is in the range of 10–10^{11} ohm-cm. The aerospace epoxy utilized in this study has a reported resistivity on the order of 10^{15} ohm-cm and cannot function toward this end without the addition of the CNT nanofiller. Through the addition of low amounts of MWCNT, 0.014 – 0.75 wt%, epoxy-CNT composites were fabricated with electrical conductivities that could be utilized for EMI and ESD applications.

1. Could the electrical properties of a CNT polymeric mixture be determined prior to curing and related to those of finished nanocomposite?

Electrical resistivity was measured from the viscous mixtures and cured composite with different wt% CNT loadings and different thermal activation times. Measurements were taken under uniform conditions. Resistivity of uncured mixtures was found to mirror behavior of the cured composites but with resistivity values ~30 to 100 times greater. These results suggest that the electrical resistivity of an uncured mixture, barring abnormal curing conditions, could be utilized to extrapolate the anticipated performance of the subsequent composite with reasonable precision. This suggests that the uncured resistivity could be a useful quality metric during production.

2. How does thermal activation effect the rheology of an uncured mixture and does this functionalization technique affect the electrical properties of the finished nanocomposite?

Thermal activation was used to change the resistivity and viscosity of the studied CNT composites. This process was performed at 500 ºC with exposure time of 1, 2, and 2.5 h. Thermal activation was found to increase resistivity of both the mixture and composite by as much as 3 orders of magnitude. Increased activation time resulted in increased resistivity. These changes in electrical properties were attributed to two factors. XRD analysis indicated a more complete oxidation of the iron catalyst as activation time was lengthened. The second, confirmed via optical analysis of the CNT network, revealed drastic changes to CNT bundle length, and consequently their aspect ratio and connectedness of the CNT network. Thermal activation appreciably affects the resistivity of a composite fabricated from this CNT pulp. For the three loadings under investigation, 0.2 wt% and 0.75 wt% still presented electrical properties suitable for the intended application at the most extreme 2.5 h activation time, 1.89×10^4 and 5.23×10^3 ohm-cm respectively. Extremely low loading samples of 0.014% activated CNTs resulted in resistivities above what could be measured by the accessible equipment. This suggests a resistivity $> 10^6$ ohm-cm and brings EMI applicability into question for that particular composition, however, the specimens will still be suitable for ESD.

This viscosity the uncured samples were also analyzed. Viscosity demonstrated strong dependence on CNT loading and applied strain. Increased activation time was found to significantly reduce the viscosity of the uncured mixture and surface profile of cured composite films. Two possible mechanisms were discussed, decreased interaction and binding within the CNT network, supported by optical microscopy findings, or increased dispersion due to functionalization of tube walls, supported by similar findings reported by other research groups. Within wt% regimes, a decreasing viscosity correlated to increased resistivity in both the mixture and cured composite.

In sum, an inverse relationship between uncured viscosity was identified. Additionally, resistivity of uncured mixtures, activated and unactivated, remained closely related to that of the cured composite. Uncured viscosity and resistivity as an in-line parameter during production would be useful for ensuring cured composite properties are consistent and predictable.

3. Can existing NDE technology be utilized to investigate epoxy-CNT composites effectively?

Ultrasonic testing of EA9496 epoxy, various wt% CNT loadings, and manufactured defects was explored. The increased CNT loading was found to reduce overall density as well as the measured longitudinal velocity. Across three distinct wt% CNT loadings defects were introduced in the form of CNT-dense agglomerations, silica beads, copper wire, and air gaps (drilled holes). Detection probability decreased with increased CNT loading; UT employed on 0.75 wt% CNT samples was unable to distinguish any of the defects introduced. Nanocomposite constructed from what is consider extremely low loading (.014 wt% CNT) demonstrated a minimum detectable flaw size of ~ 250 μm. CNT dense regions calculated to be close to 5 wt%, significantly higher than other mixtures tested here, were undetectable in a matrix of pure EA9396 epoxy. These findings dictate that ultrasonic inspection of CNT epoxy composites would not be of value when analysis flaws in the dispersion of CNTs in a composite. Alternative methods, such as SEM and micro-CT analysis, when paired with the contrast improvements discussed in Chapter IV, offer higher resolution and are likely better suited for analysis of these nanocomposites.

4. Can methods of visualizing a CNT network within the nanocomposite be improved while maintaining the required electrical properties for EMI and applications?

Nanoparticles of Eu:Y_2O_3 were synthesized by an approach that enabled their attachment to the CNT surface for the purpose of increasing the contrast between their network and the surrounding polymeric matrix. The particle's adherence to the exterior tube walls was documented via transmission electron microscopy. SEM and micro-CT analyses of Eu:Y_2O_3-CNTs were conducted on samples fabricated from CNT pulp as received from the manufacturer, and Eu:Y_2O_3-CNTs under similar conditions. Nucleation of Eu:Y_2O_3 resulting in significant improvements contrast and detection of CNT network in a cured composite. Additionally, ultraviolet-induced fluorescence of the Eu:Y_2O_3-CNT was documented at ~ 612 nm. Further development of this technique could allow utilization and automation opportunities in the CNT industry.

5. How does an extreme operating condition like, vacuum, UV irradiation, and temperature effect the electrical performance of the composite in real-time? Are these changes detrimental and permanent?

Composites with three different CNT loadings were analyzed in a simulated LEO environment. Reductions in resistivity as high as 40% were observed under vacuum and elevated temperature produced by the TVAC. De-coupling these effects through exposure to temperature only produced similar results. Simulated sunlight exposure, and the associated temperature increase, resulted in decreases as high as 58%. The effects of low vacuum generated from were a vacuum desiccation chamber kept at constant temperature were also found to produce reductions of up to 24.6%. Increased mobility of charge carriers due to thermal activation or light effects were discussed as possible mechanisms for this conductivity enhancement. Excess porosity in 0.2 wt% samples were suspected of exacerbating changes through increased retention of volatiles and subsequent off-gassing under vacuum and elevated temperatures. This was supported with thermogravimetric analysis and highlights the importance of controlling the fabrication process, and thus, porosity of the thin film composites. In all cases, the net effect was a reduction of resistivity (increased conductivity), and not detrimental to the intended function of EMI or ESD.

It is essential that the techniques and processes employed while fabricating and employing CNT epoxy composites do not increase the resistivity of the material outside the range of applicability for its intended use – ESD and EMI. In Chapter I, Table 2, the electrical resistivity measurements collected by many different research groups were present. Now, Figure 54 plots this data, along with the resistivity measurements documented throughout this course of study. The minimum electrical resistivity required for EMI and ESD applications is shown on the right side of the graph. Through inspection of this figure it then becomes apparent that while certain treatments, thermal activation and Eu:Y_2O_3 synthesis, and extreme conditions, simulated LEO, impacted electrical resistivity, they are still within the required range.

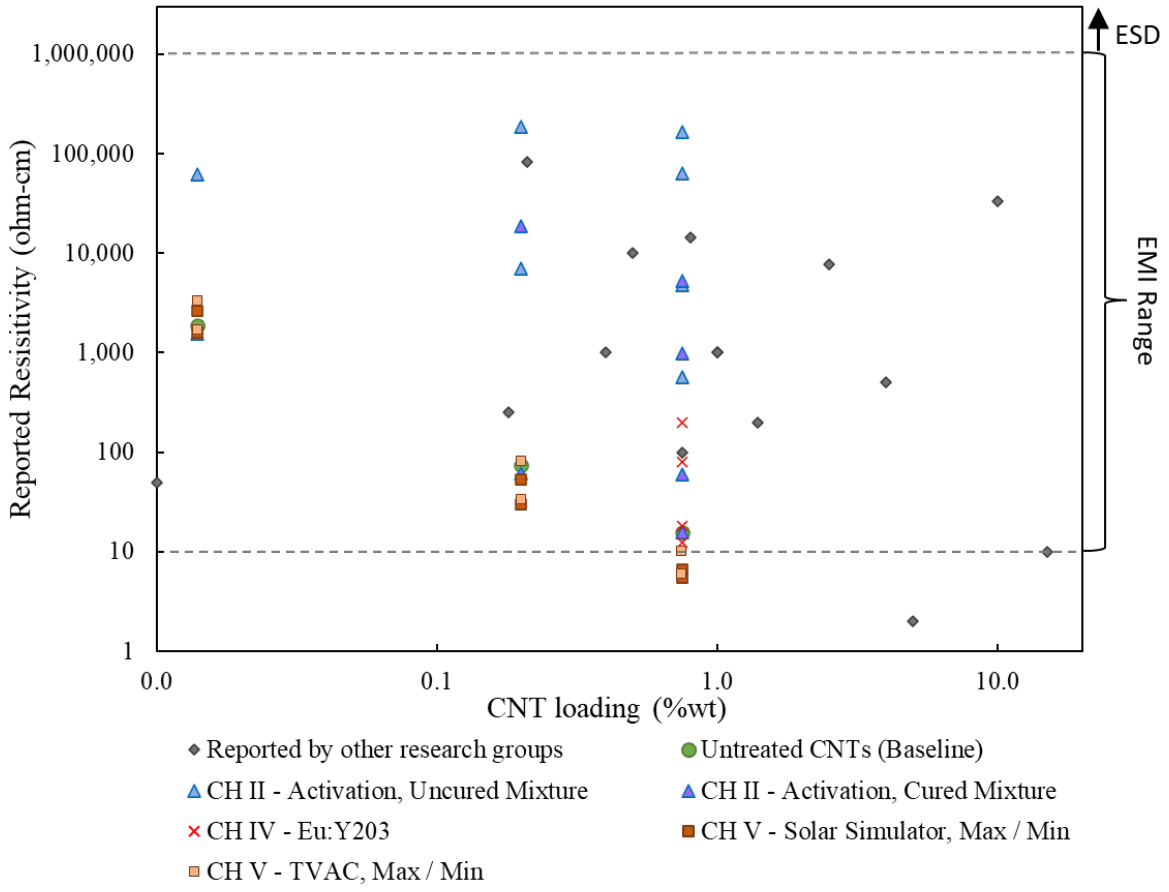

Figure 54. Comparison of epoxy-CNT composite resistivity collected by other groups and those collected in this study.

The objectives of this research were prompted by the increased adoption of epoxy-CNT composites and the need to better understand their electrical properties and mechanisms during production, evaluation, testing, and use. These objectives, and associated research questions were successfully answered through this course of study. As a result of the study highlighting the relationship between uncured and cured properties, quality can potentially be evaluated and ensured throughout production. Improvements to SEM and micro-CT visualization can enhance visualization of the CNT network and facilitate a better understanding of their mechanisms. Understanding the transient nature of environmental conditions on electrical performance allows for better design while highlighting the importance of production controls to eliminate excess porosity. The novelty of these studies was established by publication in peer review journals and

contribute to the existing base of knowledge surrounding the electrical properties of epoxy-CNT composites while supporting their target functionality– applications for EMI and ESD in the aerospace industry. As a result, future research and industry efforts could begin with a deeper understanding of the electrical behavior of epoxy-CNT composites potentially expediting efforts in adoption and commercialization.

VII. FUTURE WORK

During the course of this research studying epoxy-CNT composite and their electrical properties several opportunities were identified for future work that would contribute to an improved understanding of these materials.

1. Conduct a parametric study of uncured resistivity and viscosity and cured composite resistivity. This data could then be utilized as the basis of a model for production of cured composite resistivity

2. Seek industry partnerships to further technical readiness level (TRL) of the red fluorescence of Eu:Y_2O_3-CNTs. Chapter IV demonstrated the potential to utilize the DUV florescence granted by Eu:Y_2O_3 to for the evaluation of dispersion and the underlying CNT network. Partnering with a capable industry player would is the next logical progression.

3. Ensure fabrication protocols utilize vacuum and elevated temperatures to reduce air entrapment in viscous mixtures and ultimately reduce porosity of the composite. Porosity, particularly at higher wt% CNT loadings, presented significant problems during production, evaluating finished samples, and was a noted source of error in the 0.2 wt% sample analyzed under in-situ LEO conditions. Additionally, the viscosity of the resin is such that entrained air can't break surface tension, thicker samples have a propensity to cure with a foam-like top layer. Heating epoxy to 80 C has resulted in reduced viscosities in epoxy-CNT mixtures [133] and has been used in conjunction with vacuum [61] for the purpose of reducing entrained air.

4. Characterize the impact of porosity on electrical performance across all loading regimes. This could have secondary benefits for using porosity as a quality metric.

THIS PAGE INTENTIONALLY LEFT BLANK

LIST OF REFERENCES

[1] Dresselhaus, M. S., Dresselhaus, G., and Avouris, P., eds., 2001, *Carbon Nanotubes: Synthesis, Structure, Properties, and Applications*, Springer-Verlag, Berlin Heidelberg.

[2] Dresselhaus, M. S., Dresselhaus, G., Charlier, J. C., and Hernández, E., 2004, "Electronic, Thermal and Mechanical Properties of Carbon Nanotubes," *Philosophical Transactions: Mathematical, Physical and Engineering Sciences*, 362(1823), pp. 2065–2098.

[3] Kinloch, I. A., Suhr, J., Lou, J., Young, R. J., and Ajayan, P. M., 2018, "Composites with Carbon Nanotubes and Graphene: An Outlook," *Science*, 362(6414), pp. 547–553.

[4] "Finally, the First Mass Market Adoption of a Nanocarbon, Discusses IDTechEx" [Online]. Available: https://www.yahoo.com/now/finally-first-mass-market-adoption-182800861.html. [Accessed: 22-Mar-2022].

[5] Earp, B., Simpson, J., Phillips, J., Grbovic, D., Vidmar, S., McCarthy, J., and Luhrs, C., 2019, "Electrically Conductive CNT Composites at Loadings below Theoretical Percolation Values," *Nanomaterials*, 9(4), p. 491.

[6] Watson, K. A., and Connell, J. W., 2006, "Chapter 19 - Polymer and Carbon Nanotube Composites for Space Applications," *Carbon Nanotechnology*, L. Dai, ed., Elsevier, Amsterdam, pp. 677–698.

[7] Bellucci, S., Balasubramanian, C., Micciulla, F., and Rinaldi, G., 2007, "CNT Composites for Aerospace Applications," *Journal of Experimental Nanoscience*, 2, pp. 193–206.

[8] Yadav, R., Tirumali, M., Wang, X., Naebe, M., and Kandasubramanian, B., 2020, "Polymer Composite for Antistatic Application in Aerospace," *Defence Technology*, 16, pp. 107–118.

[9] Smith, J., Connell, J. W., Delozier, D. M., Lillehei, P., Watson, K. A., Lin, Y., Zhou, B., and Sun, Y., 2004, "Space Durable Polymer/Carbon Nanotube Films for Electrostatic Charge Mitigation," *Polymer*, 45, pp. 825–836.

[10] Kumar, P., Maiti, U. N., Sikdar, A., Das, T. K., Kumar, A., and Sudarsan, V., 2019, "Recent Advances in Polymer and Polymer Composites for Electromagnetic Interference Shielding: Review and Future Prospects," *Polymer Reviews*, 59(4), pp. 687–738.

[11] Pang, H., Xu, L., Yan, D.-X., and Li, Z.-M., 2014, "Conductive Polymer Composites with Segregated Structures," *Progress in Polymer Science*, 39(11), pp. 1908–1933.

[12] Zhang, X.-H., Zhang, Z.-H., Xu, W.-J., Chen, F.-C., Deng, J.-R., and Deng, X., 2008, "Toughening of Cycloaliphatic Epoxy Resin by Multiwalled Carbon Nanotubes," *Journal of Applied Polymer Science*, 110(3), pp. 1351–1357.

[13] Yokozeki, T., Iwahori, Y., Ishibashi, M., Yanagisawa, T., Imai, K., Arai, M., Takahashi, T., and Enomoto, K., 2009, "Fracture Toughness Improvement of CFRP Laminates by Dispersion of Cup-Stacked Carbon Nanotubes," *Composites Science and Technology*, 69(14), pp. 2268–2273.

[14] Loos, M. R., Yang, J., Feke, D. L., and Manas-Zloczower, I., 2012, "Enhanced Fatigue Life of Carbon Nanotube-Reinforced Epoxy Composites," *Polymer Engineering & Science*, 52(9), pp. 1882–1887.

[15] Jen, Y.-M., and Wang, Y.-C., 2012, "Stress Concentration Effect on the Fatigue Properties of Carbon Nanotube/Epoxy Composites," *Composites Part B: Engineering*, 43(4), pp. 1687–1694.

[16] Zhang, W., Picu, R. C., and Koratkar, N., 2007, "Suppression of Fatigue Crack Growth in Carbon Nanotube Composites," *Appl. Phys. Lett.*, 91(19), p. 193109.

[17] Deng, L., Young, R. J., Kinloch, I. A., Sun, R., Zhang, G., Noé, L., and Monthioux, M., 2014, "Coefficient of Thermal Expansion of Carbon Nanotubes Measured by Raman Spectroscopy," *Applied Physics Letters*, 104(5), p. 051907.

[18] Gojny, F. H., Wichmann, M. H. G., Köpke, U., Fiedler, B., and Schulte, K., 2004, "Carbon Nanotube-Reinforced Epoxy-Composites: Enhanced Stiffness and Fracture Toughness at Low Nanotube Content," *Composites Science and Technology*, 15(64), pp. 2363–2371.

[19] Pantano, A., Montinaro, N., Cerniglia, D., Micciulla, F., Bistarelli, S., Cataldo, A., and Bellucci, S., 2019, "Novel Non-Destructive Evaluation Technique for the Detection of Poor Dispersion of Carbon Nanotubes in Nanocomposites," *Composites Part B: Engineering*, 163, pp. 52–58.

[20] Loos, J., Alexeev, A., Grossiord, N., Koning, C. E., and Regev, O., 2005, "Visualization of Single-Wall Carbon Nanotube (SWNT) Networks in Conductive Polystyrene Nanocomposites by Charge Contrast Imaging," *Ultramicroscopy*, 104(2), pp. 160–167.

[21] Finnie, P., Kaminska, K., Homma, Y., Austing, D. G., and Lefebvre, J., 2008, "Charge Contrast Imaging of Suspended Nanotubes by Scanning Electron Microscopy," *Nanotechnology*, 19(33), p. 335202.

[22] Li, W., and Bauhofer, W., 2011, "Imaging of CNTs in a Polymer Matrix at Low Accelerating Voltages Using a SEM," *Carbon*, 49(12), pp. 3891–3898.

[23] Yue, L., Pircheraghi, G., Monemian, S. A., and Manas-Zloczower, I., 2014, "Epoxy Composites with Carbon Nanotubes and Graphene Nanoplatelets – Dispersion and Synergy Effects," *Carbon*, 78, pp. 268–278.

[24] Jang, H. G., Yang, B., Khil, M.-S., Kim, S. Y., and Kim, J., 2019, "Comprehensive Study of Effects of Filler Length on Mechanical, Electrical, and Thermal Properties of Multi-Walled Carbon Nanotube/Polyamide 6 Composites," *Composites Part A: Applied Science and Manufacturing*, 125, p. 105542.

[25] Micheli, D., Apollo, C., Pastore, R., Bueno Morles, R., Coluzzi, P., and Marchetti, M., 2012, "Temperature, Atomic Oxygen and Outgassing Effects on Dielectric Parameters and Electrical Properties of Nanostructured Composite Carbon-Based Materials," *Acta Astronautica*, 76, pp. 127–135.

[26] Tucci, V., Guadagno, L., Raimondo, M., Vittoria, V., Vertuccio, L., Naddeo, C., Russo, S., De vivo, B., Lamberti, P., and Spinelli, G., 2014, "Development of Epoxy Mixtures for Application in Aeronautics and Aerospace," *RSC Advances*, 4.

[27] Samwel, S., 2014, "Low Earth Orbital Atomic Oxygen Erosion Effect on Spacecraft Materials," *Space Research Journal*, 7, pp. 1–13.

[28] Jiao, L., Gu, Y., Wang, S., Yang, Z., Wang, H., Li, Q., li, M., and Zhang, Z., 2015, "Atomic Oxygen Exposure Behaviors of CVD-Grown Carbon Nanotube Film and Its Polymer Composite Film," *Composites Part A: Applied Science and Manufacturing*, 71, pp. 116–125.

[29] Prusty, R. K., Rathore, D. K., and Ray, B. C., 2017, "CNT/Polymer Interface in Polymeric Composites and Its Sensitivity Study at Different Environments," *Advances in Colloid and Interface Science*, 240, pp. 77–106.

[30] Iijima, S., 1991, "Helical Microtubules of Graphitic Carbon," *Nature*, 354(6348), pp. 56–58.

[31] O'Connell, M., ed., 2006, *Carbon Nanotubes: Properties and Applications*, CRC/ Taylor & Francis, Boca Raton, FL.

[32] Bacon, R., 1960, "Growth, Structure, and Properties of Graphite Whiskers," *Journal of Applied Physics*, 31(2), pp. 283–290.

[33] Oberlin, A., Endo, M., and Koyama, T., 1976, “High Resolution Electron Microscope Observations of Graphitized Carbon Fibers.”

[34] Oberlin, A., Endo, M., and Koyama, T., 1976, “Filamentous Growth of Carbon through Benzene Decomposition,” *Journal of Crystal Growth*, 32(3), pp. 335–349.

[35] Iijima, S., and Ichihashi, T., 1993, “Single-Shell Carbon Nanotubes of 1-Nm Diameter,” *Nature*, 363(6430), p. 603.

[36] Collins, P. G., and Avouris, P., “They Are Stronger than Steel, but the Most Important Uses for These Threadlike Macromolecules May Be in Faster, More Efficient and More Durable Electronic Devices,” p. 8.

[37] Liu, H., and Thostenson, E. T., 2018, “6.11 Conductive Nanocomposites for Multifunctional Sensing Applications,” *Comprehensive Composite Materials II*, P.W.R. Beaumont, and C.H. Zweben, eds., Elsevier, Oxford, pp. 315–351.

[38] Chen, C.-K., Perry, W., Xu, H., Jiang, Y., and Phillips, J., 2003, “Plasma Torch Production of Macroscopic Carbon Nanotube Structures.”

[39] Wang, J., Shen, B., Lan, M., Kang, D., and Wu, C., 2020, “Carbon Nanotubes (CNTs) Production from Catalytic Pyrolysis of Waste Plastics: The Influence of Catalyst and Reaction Pressure,” *Catalysis Today*, 351, pp. 50–57.

[40] Collins, P. G., Arnold, M. S., and Avouris, P., 2001, “Engineering Carbon Nanotubes and Nanotube Circuits Using Electrical Breakdown,” *Science*, 292(5517), pp. 706–709.

[41] Saito, R., Dresselhaus, G., and Dresselhaus, M. S., 1993, “Electronic Structure of Double-layer Graphene Tubules,” *Journal of Applied Physics*, 73(2), pp. 494–500.

[42] Xu, Z., Bai, X., Wang, Z. L., and Wang, E., 2006, “Multiwall Carbon Nanotubes Made of Monochirality Graphite Shells,” *J. Am. Chem. Soc.*, 128(4), pp. 1052–1053.

[43] Ruland, W., Schaper, A. K., Hou, H., and Greiner, A., 2003, “Multi-Wall Carbon Nanotubes with Uniform Chirality: Evidence for Scroll Structures,” *Carbon*, 41(3), pp. 423–427.

[44] Bandaru, P. R., 2007, “Electrical Properties and Applications of Carbon Nanotube Structures,” *J Nanosci Nanotechnol*, 7(4), pp. 1239–1267.

[45] Ying, Z., Wu, D., Zhang, M., and Qiu, Y., 2017, “Polylactide/Basalt Fiber Composites with Tailorable Mechanical Properties: Effect of Surface Treatment of Fibers and Annealing,” *Composite Structures*, 176, pp. 1020–1027.

[46] Menchhofer, P. A., Johnson, J. E., and Lindahl, J. M., 2016, *Carbon Nanotube Chopped Fiber for Enhanced Properties in Additive Manufacturincomg*, ORNL/ TM-2016/277, 1302927.

[47] Al-Saleh, M. H., Saadeh, W. H., and Sundararaj, U., 2013, "EMI Shielding Effectiveness of Carbon Based Nanostructured Polymeric Materials: A Comparative Study," *Carbon*, 60, pp. 146–156.

[48] Al-Saleh, M. H., and Sundararaj, U., 2009, "Electromagnetic Interference Shielding Mechanisms of CNT/Polymer Composites," *Carbon*, 47(7), pp. 1738–1746.

[49] Kasaliwal, G. R., Göldel, A., Pötschke, P., and Heinrich, G., 2011, "Influences of Polymer Matrix Melt Viscosity and Molecular Weight on MWCNT Agglomerate Dispersion," *Polymer*, 52(4), pp. 1027–1036.

[50] Socher, R., Krause, B., Müller, M. T., Boldt, R., and Pötschke, P., 2012, "The Influence of Matrix Viscosity on MWCNT Dispersion and Electrical Properties in Different Thermoplastic Nanocomposites," *Polymer*, 53(2), pp. 495–504.

[51] Krause, B., Pötschke, P., and Häußler, L., 2009, "Influence of Small Scale Melt Mixing Conditions on Electrical Resistivity of Carbon Nanotube-Polyamide Composites," *Composites Science and Technology*, 69(10), pp. 1505–1515.

[52] Pinto, V. C., Ramos, T., Alves, A. S. F., Xavier, J., Tavares, P. J., Moreira, P. M. G. P., and Guedes, R. M., 2017, "Dispersion and Failure Analysis of PLA, PLA/ GNP and PLA/CNT-COOH Biodegradable Nanocomposites by SEM and DIC Inspection," *Engineering Failure Analysis*, 71, pp. 63–71.

[53] Hua, J., Wang, Z., Xu, L., Wang, X., Zhao, J., and Li, F., 2013, "Preparation Polystyrene/Multiwalled Carbon Nanotubes Nanocomposites by Copolymerization of Styrene and Styryl-Functionalized Multiwalled Carbon Nanotubes," *Materials Chemistry and Physics*, 137(3), pp. 694–698.

[54] Askins, R., 1991, *Characterization of EA9396 Epoxy Resin for Composite Repair Applications*, University of Dayton Research Institute.

[55] Henkel Corporation. *Structural Adhesives Product Selector Guide*. Accessed March 18, 2022. Available: https://dm.henkel-am.com/is/content/henkel/brochure-structural-adhesives-product-selector-guide-.print.

[56] "LOCTITE 9396aero" [Online]. Available: https://www.henkel-adhesives.com/vn/en/product/adhesives/loctite_ea_9396_aero.html. [Accessed: 28-Jan-2021].

[57] "Henkel Loctite EA 9396 AERO, Part A, Part B SDS" [Online]. Available: https://www.ellsworth.com/products/adhesives/epoxy/henkel-loctite-hysol-ea-9396-epoxy-adhesive-1-qt-kit/. [Accessed: 18-Mar-2022].

[58] Stauffer, D., and Aharony, A., 2017, *Introduction To Percolation Theory: Second Edition*, Taylor & Francis, London.

[59] Sahini, M., and Sahimi, M., 2014, *Applications Of Percolation Theory*, CRC Press, London.

[60] Shehzad, K., Ahmad, M. N., Hussain, T., Mumtaz, M., Shah, A. T., Mujahid, A., Wang, C., Ellingsen, J., and Dang, Z.-M., 2014, "Influence of Carbon Nanotube Dimensions on the Percolation Characteristics of Carbon Nanotube/Polymer Composites," *Journal of Applied Physics*, 116(6), p. 064908.

[61] Song, Y. S., and Youn, J. R., 2005, "Influence of Dispersion States of Carbon Nanotubes on Physical Properties of Epoxy Nanocomposites," *Carbon*, 43(7), pp. 1378–1385.

[62] Bao, H.-D., Sun, Y., Xiong, Z.-Y., Guo, Z.-X., and Yu, J., 2013, "Effects of the Dispersion State and Aspect Ratio of Carbon Nanotubes on Their Electrical Percolation Threshold in a Polymer," *J. Appl. Polym. Sci.*, 128(1), pp. 735–740.

[63] Tarlton, T., Sullivan, E., Brown, J., and Derosa, P. A., 2017, "The Role of Agglomeration in the Conductivity of Carbon Nanotube Composites near Percolation," *Journal of Applied Physics*, 121(8), p. 085103.

[64] Sandler, J. K. W., Kirk, J. E., Kinloch, I. A., Shaffer, M. S. P., and Windle, A. H., 2003, "Ultra-Low Electrical Percolation Threshold in Carbon-Nanotube-Epoxy Composites," *Polymer*, 44(19), pp. 5893–5899.

[65] Munson-McGee, S. H., 1991, "Estimation of the Critical Concentration in an Anisotropic Percolation Network," *Phys. Rev. B*, 43(4), pp. 3331–3336.

[66] Celzard, A., McRae, E., Deleuze, C., Dufort, M., Furdin, G., and Marêché, J. F., 1996, "Critical Concentration in Percolating Systems Containing a High-Aspect-Ratio Filler," *Phys. Rev. B*, 53(10), pp. 6209–6214.

[67] Li, J., and Kim, J.-K., 2007, "Percolation Threshold of Conducting Polymer Composites Containing 3D Randomly Distributed Graphite Nanoplatelets," *Composites Science and Technology*, 67(10), pp. 2114–2120.

[68] Sandler, J., Shaffer, M. S. P., Prasse, T., Bauhofer, W., Schulte, K., and Windle, A. H., 1999, "Development of a Dispersion Process for Carbon Nanotubes in an Epoxy Matrix and the Resulting Electrical Properties," *Polymer*, 40(21), pp. 5967–5971.

[69] Kilbride, B. E., Coleman, J. N., Fraysse, J., Fournet, P., Cadek, M., Drury, A., Hutzler, S., Roth, S., and Blau, W. J., 2002, "Experimental Observation of Scaling Laws for Alternating Current and Direct Current Conductivity in Polymer-Carbon Nanotube Composite Thin Films," *Journal of Applied Physics*, 92(7), pp. 4024–4030.

[70] Mansor, M. R., Fadzullah, S. H. S. M., Masripan, N. A. B., Omar, G., and Akop, M. Z., 2019, "Chapter 9 - Comparison Between Functionalized Graphene and Carbon Nanotubes: Effect of Morphology and Surface Group on Mechanical, Electrical, and Thermal Properties of Nanocomposites," *Functionalized Graphene Nanocomposites and Their Derivatives*, M. Jawaid, R. Bouhfid, and A. el Kacem Qaiss, eds., Elsevier, pp. 177–204.

[71] Kirkpatrick, S., 1973, "Percolation and Conduction," *Rev. Mod. Phys.*, 45(4), pp. 574–588.

[72] Shante, V. K. S., and Kirkpatrick, S., 1971, "An Introduction to Percolation Theory," *Advances in Physics*, 20(85), pp. 325–357.

[73] Gerenrot, D., Berlyand, L., and Phillips, J., 2003, "Random Network Model for Heat Transfer in High Contrast Composite Materials," *IEEE Transactions on Advanced Packaging*, 26(4), pp. 410–416.

[74] Rahaman, M., Theravalappil, R., Bhandari, S., Nayak, L., and Bhagabati, P., 2022, "4 - Electrical Conductivity of Polymer-Graphene Composites," *Polymer Nanocomposites Containing Graphene*, M. Rahaman, L. Nayak, I.A. Hussein, and N.C. Das, eds., Woodhead Publishing, pp. 107–139.

[75] Marsden, A. J., Papageorgiou, D. G., Vallés, C., Liscio, A., Palermo, V., Bissett, M. A., Young, R. J., and Kinloch, I. A., 2018, "Electrical Percolation in Graphene–Polymer Composites," *2D Mater.*, 5(3), p. 032003.

[76] Nan, C.-W., Shen, Y., and Ma, J., 2010, "Physical Properties of Composites Near Percolation," *Annu. Rev. Mater. Res.*, 40(1), pp. 131–151.

[77] Ambrosetti, G., Grimaldi, C., Balberg, I., Maeder, T., Danani, A., and Ryser, P., 2010, "Solution of the Tunneling-Percolation Problem in the Nanocomposite Regime," *Phys. Rev. B*, 81(15), p. 155434.

[78] Spitalsky, Z., Tasis, D., Papagelis, K., and Galiotis, C., 2010, "Carbon Nanotube–Polymer Composites: Chemistry, Processing, Mechanical and Electrical Properties," *Progress in Polymer Science*, 35(3), pp. 357–401.

[79] Kim, B., Lee, J., and Yu, I., 2003, "Electrical Properties of Single-Wall Carbon Nanotube and Epoxy Composites," *Journal of Applied Physics*, 94(10), pp. 6724–6728.

[80] Barrau, S., Demont, P., Maraval, C., Bernes, A., and Lacabanne, C., 2005, "Glass Transition Temperature Depression at the Percolation Threshold in Carbon Nanotube-Epoxy Resin and Polypyrrole-Epoxy Resin Composites," *Macromolecular Rapid Communications*, 2(5), pp. 390–394.

[81] dos Santos, A. S., Leite, T. de O. N., Furtado, C. A., Welter, C., Pardini, L. C., and Silva, G. G., 2008, "Morphology, Thermal Expansion, and Electrical Conductivity of Multiwalled Carbon Nanotube/Epoxy Composites," *Journal of Applied Polymer Science*, 108(2), pp. 979–986.

[82] Gojny, F. H., Wichmann, M. H. G., Fiedler, B., Kinloch, I. A., Bauhofer, W., Windle, A. H., and Schulte, K., 2006, "Evaluation and Identification of Electrical and Thermal Conduction Mechanisms in Carbon Nanotube/Epoxy Composites," *Polymer*, 47(6), pp. 2036–2045.

[83] Peng, H., and Sun, X., 2009, "Highly Aligned Carbon Nanotube/Polymer Composites with Much Improved Electrical Conductivities," *Chemical Physics Letters*, 471(1), pp. 103–105.

[84] Barrau, S., Demont, P., Perez, E., Peigney, A., Laurent, C., and Lacabanne, C., 2003, "Effect of Palmitic Acid on the Electrical Conductivity of Carbon Nanotubes−Epoxy Resin Composites," *Macromolecules*, 36(26), pp. 9678–9680.

[85] Špitalský, Z., Krontiras, C. A., Georga, S. N., and Galiotis, C., 2009, "Effect of Oxidation Treatment of Multiwalled Carbon Nanotubes on the Mechanical and Electrical Properties of Their Epoxy Composites," *Composites Part A: Applied Science and Manufacturing*, 40(6), pp. 778–783.

[86] Liu, L., Etika, K. C., Liao, K.-S., Hess, L. A., Bergbreiter, D. E., and Grunlan, J. C., 2009, "Comparison of Covalently and Noncovalently Functionalized Carbon Nanotubes in Epoxy," *Macromol Rapid Commun*, 30(8), pp. 627–632.

[87] Barrau, S., Demont, P., Peigney, A., Laurent, C., and Lacabanne, C., 2003, "DC and AC Conductivity of Carbon Nanotubes−Polyepoxy Composites," *Macromolecules*, 36(14), pp. 5187–5194.

[88] Allaoui, A., Baia, S., Chengb, H. M., and Baia, J. B., 2002, "Mechanical and Electrical Properties of a MWNT/Epoxy Composite."

[89] Thostenson, E. T., and Chou, T.-W., 2006, "Processing-Structure-Multi-Functional Property Relationship in Carbon Nanotube/Epoxy Composites," *Carbon*, 44(14), pp. 3022–3029.

[90] Yuen, S.-M., Ma, C.-C. M., Chuang, C.-Y., Hsiao, Y.-H., Chiang, C.-L., and Yu, A., 2008, "Preparation, Morphology, Mechanical and Electrical Properties of TiO2 Coated Multiwalled Carbon Nanotube/Epoxy Composites," *Composites Part A: Applied Science and Manufacturing*, 39(1), pp. 119–125.

[91] Li, N., Huang, Y., Du, F., He, X., Lin, X., Gao, H., Ma, Y., Li, F., Chen, Y., and Eklund, P. C., 2006, "Electromagnetic Interference (EMI) Shielding of Single-Walled Carbon Nanotube Epoxy Composites," *Nano Lett.*, 6(6), pp. 1141–1145.

[92] Stump, B., 2002, "H.R.4546 - 107th Congress (2001-2002): Bob Stump National Defense Authorization Act for Fiscal Year 2003" [Online]. Available: https://www.congress.gov/bill/107th-congress/house-bill/4546. [Accessed: 07-Mar-2022].

[93] Director, Defense Research & Engineering, 01MAR10, *Defense Nanotechnology Research and Development Program*, DOD.

[94] Savage, S J. 2004. *Defence Applications of Nanocomposite Materials.* Available: https://www.foi.se/rest-api/report/FOI-R--1456--SE.

[95] Burnett, M., "Advanced Materials and Manufacturing – Implications for Defence to 2040," p. 32.

[96] NSET Subcommittee of the NSTC, OCT20, *National Nanotechnology Initiative Supplement to the President's 2021 Budget*, National Science and Technology Counsel.

[97] May 2011, S. T., "Lockheed Martin Reveals F-35 to Feature Nanocomposite Structures," *Flight Global* [Online]. Available: https://www.flightglobal.com/lockheed-martin-reveals-f-35-to-feature-nanocomposite-structures/100174.article. [Accessed: 20-Mar-2022].

[98] "Army Researchers Chase Helicopter Performance Gains," *www.army.mil* [Online]. Available: https://www.army.mil/article/105134/army_researchers_chase_helicopter_performance_gains. [Accessed: 20-Mar-2022].

[99] Volpe, J., 2013, *Unmanned Aircraft System (UAS) Service Demand 2015–2035: Literature Review & Projections of Future Usage*, DOT-VNTSC-DOD-13-01, United States. Department of Transportation. Research and Innovative Technology Administration.

[100] Gohardani, O., Elola, M. C., and Elizetxea, C., 2014, "Potential and Prospective Implementation of Carbon Nanotubes on next Generation Aircraft and Space Vehicles: A Review of Current and Expected Applications in Aerospace Sciences," *Progress in Aerospace Sciences*, 70, pp. 42–68.

[101] Hubbard, J., Tirano, J., Zea, H., and Luhrs, C., 2022, "Effects of Thermal Activation on CNT Nanocomposite Electrical Conductivity and Rheology," *Polymers*, 14(5), p. 1003.

[102] Martin, C. A., Sandler, J. K. W., Shaffer, M. S. P., Schwarz, M.-K., Bauhofer, W., Schulte, K., and Windle, A. H., 2004, "Formation of Percolating Networks in Multi-Wall Carbon-Nanotube–Epoxy Composites," *Composites Science and Technology*, 64(15), pp. 2309–2316.

[103] Du, J.-H., Bai, J., and Cheng, H.-M., 2007, "The Present Status and Key Problems of Carbon Nanotube Based Polymer Composites," *Express Polym. Lett.*, 1(5), pp. 253–273.

[104] Harris, P. J. F., 2004, "Carbon Nanotube Composites," *Int. Mater. Rev.*, 49(1), pp. 31–43.

[105] Kausar, A., Rafique, I., and Muhammad, B., 2016, "Review of Applications of Polymer/Carbon Nanotubes and Epoxy/CNT Composites," *Polymer-Plastics Technology and Engineering*, 55(11), pp. 1167–1191.

[106] Park, S.-H., and Ha, J.-H., 2019, "Improved Electromagnetic Interference Shielding Properties Through the Use of Segregate Carbon Nanotube Networks," *Materials*, 12(9), p. 1395.

[107] Earp, B., Phillips, J., Grbovic, D., Vidmar, S., Porter, M., and Luhrs, C. C., 2020, "Impact of Current and Temperature on Extremely Low Loading Epoxy-CNT Conductive Composites," *Polymers*, 12(4), p. 867.

[108] Li, W., Buschhorn, S. T., Schulte, K., and Bauhofer, W., 2011, "The Imaging Mechanism, Imaging Depth, and Parameters Influencing the Visibility of Carbon Nanotubes in a Polymer Matrix Using an SEM," *Carbon*, 49(6), pp. 1955–1964.

[109] Lillehei, P. T., Kim, J.-W., Gibbons, L. J., and Park, C., 2009, "A Quantitative Assessment of Carbon Nanotube Dispersion in Polymer Matrices," *Nanotechnology*, 20(32), p. 325708.

[110] Kovacs, J. Z., Andresen, K., Pauls, J. R., Garcia, C. P., Schossig, M., Schulte, K., and Bauhofer, W., 2007, "Analyzing the Quality of Carbon Nanotube Dispersions in Polymers Using Scanning Electron Microscopy," *Carbon*, 45(6), pp. 1279–1288.

[111] Hubbard, J., Isik, T., Ansell, T. Y., Ortalan, V., and Luhrs, C., 2021, "Introduction of Rare-Earth Oxide Nanoparticles in CNT-Based Nanocomposites for Improved Detection of Underlying CNT Network," *Nanomaterials*, 11(9), p. 2168.

[112] Mallakpour, S., and Soltanian, S., 2016, "Surface Functionalization of Carbon Nanotubes: Fabrication and Applications," *RSC Adv.*, 6(111), pp. 109916–109935.

[113] Sahoo, N. G., Cheng, H. K. F., Bao, H., Pan, Y., Li, L., and Chan, S. H., 2011, "Covalent Functionalization of Carbon Nanotubes for Ultimate Interfacial Adhesion to Liquid Crystalline Polymer," *Soft Matter*, 7(19), pp. 9505–9514.

[114] Ma, P. C., Tang, B. Z., and Kim, J.-K., 2008, "Effect of CNT Decoration with Silver Nanoparticles on Electrical Conductivity of CNT-Polymer Composites," *Carbon*, 46(11), pp. 1497–1505.

[115] Xin, F., and Li, L., 2011, "Decoration of Carbon Nanotubes with Silver Nanoparticles for Advanced CNT/Polymer Nanocomposites," *Composites Part A: Applied Science and Manufacturing*, 42(8), pp. 961–967.

[116] Wang, K., Fishman, H. A., Dai, H., and Harris, J. S., 2006, "Neural Stimulation with a Carbon Nanotube Microelectrode Array," *Nano Lett.*, 6(9), pp. 2043–2048.

[117] Klein, K. L., Melechko, A. V., McKnight, T. E., Retterer, S. T., Rack, P. D., Fowlkes, J. D., Joy, D. C., and Simpson, M. L., 2008, "Surface Characterization and Functionalization of Carbon Nanofibers," *Journal of Applied Physics*, 103(6), p. 061301.

[118] Chen, X., Tang, X.-Z., Liang, Y. N., Cheah, J. W., Hu, P., and Hu, X., 2016, "Controlled Thermal Functionalization for Dispersion Enhancement of Multi-Wall Carbon Nanotube in Organic Solvents," *J Mater Sci*, 51(12), pp. 5625–5634.

[119] Mercier, G., Gleize, J., Ghanbaja, J., Marêché, J.-F., and Vigolo, B., 2013, "Soft Oxidation of Single-Walled Carbon Nanotube Samples," *J. Phys. Chem. C*, 117(16), pp. 8522–8529.

[120] Huang, Y. Y., Ahir, S. V., and Terentjev, E. M., 2006, "Dispersion Rheology of Carbon Nanotubes in a Polymer Matrix," *Phys. Rev. B*, 73(12), p. 125422.

[121] Arrigo, R., and Malucelli, G., 2020, "Rheological Behavior of Polymer/Carbon Nanotube Composites: An Overview," *Materials*, 13(12), p. 2771.

[122] Allaoui, A., and Bounia, N., 2010, "Rheological and Electrical Transitions in Carbon Nanotube/Epoxy Suspensions," *CNANO*, 6(2), pp. 158–162.

[123] Fogel, M., Parlevliet, P., Geistbeck, M., Olivier, P., and Dantras, E., 2015, "Thermal, Rheological and Electrical Analysis of MWCNTs/Epoxy Matrices," *Composites Science and Technology*, 110, pp. 118–125.

[124] Chakraborty, A. K., Plyhm, T., Barbezat, M., Necola, A., and Terrasi, G. P., 2011, "Carbon Nanotube (CNT)–Epoxy Nanocomposites: A Systematic Investigation of CNT Dispersion," *J Nanopart Res*, 13(12), pp. 6493–6506.

[125] Al-Saleh, M. H., and Irshidat, M. R., 2016, "Effect of Viscosity Reducing Agent on the Properties of CNT/Epoxy Nanocomposites," *Journal of Polymer Engineering*, 36(4), pp. 407–412.

[126] Mochizuki, S., 1977, "Electrical Conductivity of α-Fe2O3," *physica status solidi (a)*, 41(2), pp. 591–594.

[127] Dutta, S., Manik, S. K., Pal, M., Pradhan, S. K., Brahma, P., and Chakravorty, D., 2005, "Electrical Conductivity in Nanostructured Magnetite–Hematite Composites Produced by Mechanical Milling," *Journal of Magnetism and Magnetic Materials*, 288, pp. 301–306.

[128] Weidenfeller, B., Höfer, M., and Schilling, F., 2002, "Thermal and Electrical Properties of Magnetite Filled Polymers," *Composites Part A: Applied Science and Manufacturing*, 33(8), pp. 1041–1053.

[129] "Hematite," *Phantom Plastics* [Online]. Available: https://phantomplastics.com/functional-fillers/hematite-filler/. [Accessed: 01-Feb-2022].

[130] "Magnetite," *Phantom Plastics* [Online]. Available: https://phantomplastics.com/functional-fillers/magnetite/. [Accessed: 01-Feb-2022].

[131] Osswald, S., Flahaut, E., Ye, H., and Gogotsi, Y., 2005, "Elimination of D-Band in Raman Spectra of Double-Wall Carbon Nanotubes by Oxidation," *Chemical Physics Letters*, 402(4–6), pp. 422–427.

[132] Majidian, M., Grimaldi, C., Forró, L., and Magrez, A., 2017, "Role of the Particle Size Polydispersity in the Electrical Conductivity of Carbon Nanotube-Epoxy Composites," *Sci Rep*, 7(1), p. 12553.

[133] Rahatekar, S. S., Koziol, K. K. K., Butler, S. A., Elliott, J. A., Shaffer, M. S. P., Mackley, M. R., and Windle, A. H., 2006, "Optical Microstructure and Viscosity Enhancement for an Epoxy Resin Matrix Containing Multiwall Carbon Nanotubes," *Journal of Rheology*, 50(5), pp. 599–610.

[134] Rupnow, T., and Icenogle, P., MAR-APR2012, "Surface Resistivity Measurements for Quality Assurance Pave the Way to Savings in Louisiana," *Transportation Research Board*, pp. 46–47.

[135] Ferreira, R. M., and Jalali, S., 2006, "Quality Control Based on Electrical Resistivity Measurements." Proceedings of ESCS, 12 June, 2006, p. 325.

[136] "Importance of Viscosity in Food Manufacturing from Cole-Parmer" [Online]. Available: https://www.coleparmer.com/tech-article/viscosity-in-food-manufacturing. [Accessed: 29-Nov-2021].

[137] "Quality Control of Pharmaceutical Products Using Rotational Viscometry :: Anton Paar Wiki," *Anton Paar* [Online]. Available: https://wiki.anton-paar.com/us-en/basic-of-viscometry/quality-control-of-pharmaceutical-products-using-rotational-viscometry/. [Accessed: 29-Nov-2021].

[138] Allen, L. V., 2003, "Quality-Control Analytical Methods: Viscosity Measurement," *International Journal of Pharmaceutical Compounding*, 7(4), p. 305.

[139] "Paints and Coatings: Quality Control and Research :: Anton-Paar.Com," *Anton Paar* [Online]. Available: https://www.anton-paar.com/us-en/viscometry-rheometry/paints-and-coatings-quality-control-and-research/. [Accessed: 29-Nov-2021].

[140] Dash, M., 2021, "High Quality 'Greener' Coatings through Automated Viscosity Monitoring and Control » Rheonics :: Viscometer and Density Meter," *rheonics :: viscometer and density meter* [Online]. Available: https://rheonics.com/high-quality-greener-coatings-through-automated-viscosity-monitoring-and-control/. [Accessed: 29-Nov-2021].

[141] "Optimizing the Measurement and Control of Viscosity for Consistent Quality - Lubrizol" [Online]. Available: https://www.lubrizol.com/Coatings/Blog/2021/09/Viscosity-for-Consistent-Quality. [Accessed: 29-Nov-2021].

[142] "Lubricants | Viscosity Measurement for In-Service Oil :: Anton-Paar.Com," *Anton Paar* [Online]. Available: https://www.anton-paar.com/corp-en/services-support/document-finder/application-reports/lubricants-viscosity-measurement-for-in-service-oil/. [Accessed: 29-Nov-2021].

[143] "Viscosity Index :: Anton Paar Wiki," *Anton Paar* [Online]. Available: https://wiki.anton-paar.com/us-en/viscosity-index/. [Accessed: 29-Nov-2021].

[144] "Alarms 101: Setting Viscosity Alarms and Limits" [Online]. Available: https://www.machinerylubrication.com/Read/429/viscosity-alarms-limits. [Accessed: 29-Nov-2021].

[145] Lee, S.-G., Oh, D., and Woo, J. H., 2021, "The Effect of High Glass Fiber Content and Reinforcement Combination on Pulse-Echo Ultrasonic Measurement of Composite Ship Structures," *Journal of Marine Science and Engineering*, 9(4), p. 379.

[146] Henrich, R., and Schnars, U., "Applications of NDT Methods on Composite Structures in Aerospace Industry," Proceedings of the CDMC, Stuttgart, Germany, 18-19 September, 2006, p. 8.

[147] Stone, D. E. W., and Clarke, B., 1975, "Ultrasonic Attenuation as a Measure of Void Content in Carbon-Fibre Reinforced Plastics," *Non-Destructive Testing*, 8(3), pp. 137–145.

[148] Hsu, D. K., and Jeong, H., 1989, "Ultrasonic Velocity Change and Dispersion Due to Porosity in Composite Laminates," *Review of Progress in Quantitative Nondestructive Evaluation*, D.O. Thompson, and D.E. Chimenti, eds., Springer U.S., Boston, MA, pp. 1567–1573.

[149] Datta, D., Munshi, P., and Kishore, N., 1996, "Automated Ultrasonic NDE of Composite Specimens by Cluster and Fractal Analysis," *Nondestructive Testing and Evaluation*, 13(1), pp. 15–30.

[150] Godinez-Azcuaga, V. F., Carlos, M. F., and Donahue, J., "Automated Ultrasonic Testing during Production: Avoiding Bottlenecks and Increasing Throughput," p. 8.

[151] Zakutailov, K. V., Levin, V. M., and Petronyuk, Yu. S., 2010, "High-Resolution Ultrasonic Ultrasound Methods: Microstructure Visualization and Diagnostics of Elastic Properties of Modern Materials (Review)," *Inorg Mater*, 46(15), pp. 1655–1661.

[152] Levin, V., Petronyuk, Y., Morokov, E., Chernozatonskii, L., Kuzhir, P., Fierro, V., Celzard, A., Mastrucci, M., Tabacchioni, I., Bistarelli, S., and Bellucci, S., 2016, "The Cluster Architecture of Carbon in Polymer Nanocomposites Observed by Impulse Acoustic Microscopy," *physica status solidi (b)*, 253(10), pp. 1952–1959.

[153] Levin, V., Morokov, E., Petronyuk, Y., Cataldo, A., Bistarelli, S., Micciulla, F., and Bellucci, S., 2017, "Cluster Microstructure and Local Elasticity of Carbon-Epoxy Nanocomposites Studied by Impulse Acoustic Microscopy: Cluster Microstructure and Local Elasticity of Carbon-Epoxy Nanocomposites Studied by Impulse Acoustic Microscopy," *Polym Eng Sci*, 57(7), pp. 697–702.

[154] Levin, V. M., Petronyuk, Y. S., Morokov, E. S., Celzard, A., Bellucci, S., and Kuzhir, P. P., 2015, "What Does See the Impulse Acoustic Microscopy inside Nanocomposites?," *Physics Procedia*, 70, pp. 703–706.

[155] Bond, Leonard J. “Fundamentals of Ultrasonic Inspection.” In *Nondestructive Evaluation of Materials*, 155–68. ASTM Handbook Volume 17.

[156] “2.5 Wave Front Dynamics | Olympus IMS” [Online]. Available: https://www.olympus-ims.com/en/ndt-tutorials/flaw-detection/wave-front/. [Accessed: 30-Mar-2021].

[157] “Solids and Metals - Speed of Sound” [Online]. Available: https://www.engineeringtoolbox.com/sound-speed-solids-d_713.html. [Accessed: 22-Mar-2022].

[158] Martin, B. G., 1977, “Ultrasonic Wave Propagation in Fiber-reinforced Solids Containing Voids,” *Journal of Applied Physics*, 48(8), pp. 3368–3373.

[159] Reynolds, W. N., and Wilkinson, S. J., 1978, “The Analysis of Fibre-Reinforced Porous Composite Materials by the Measurement of Ultrasonic Wave Velocities,” *Ultrasonics*, 16(4), pp. 159–163.

[160] “UT Material Properties Tables” [Online]. Available: https://www.nde-ed.org/GeneralResources/MaterialProperties/UT/ut_matlprop_plastics.htm. [Accessed: 25-Aug-2020].

[161] De Volder, M. F. L., Tawfick, S. H., Baughman, R. H., and Hart, A. J., 2013, “Carbon Nanotubes: Present and Future Commercial Applications,” *Science*, 339(6119), pp. 535–539.

[162] Yang, Y., Gupta, M. C., and Dudley, K. L., 2007, “Studies on Electromagnetic Interference Shielding Characteristics of Metal Nanoparticle- and Carbon Nanostructure-Filled Polymer Composites in the Ku-Band Frequency,” *Micro & Nano Letters*, 2(4), pp. 85–89.

[163] Khan, W., Sharma, R., and Saini, P., 2016, “Carbon Nanotube-Based Polymer Composites: Synthesis, Properties and Applications,” *Carbon Nanotubes - Current Progress of Their Polymer Composites*, M. Berber, and I.H. Hafez, eds., Intech Open, London, United Kingdom, pp. 1–45.

[164] Chang, N. C., 1963, “Fluorescence and Stimulated Emission from Trivalent Europium in Yttrium Oxide,” *Journal of Applied Physics*, 34(12), pp. 3500–3504.

[165] Chang, N. C., and Gruber, J. B., 1964, “Spectra and Energy Levels of Eu^{3+} in Y_2O_3,” *The Journal of Chemical Physics*, 41(10), pp. 3227–3234.

[166] Blasse, G., and Grabmaier, B. C., 1994, *Luminescent Materials*, Springer Berlin / Heidelberg, Berlin, Heidelberg, Germany.

[167] Mariscal-Becerra, L., Vázquez-Arreguín, R., Balderas, U., Carmona-Téllez, S., Murrieta Sánchez, H., and Falcony, C., 2017, "Luminescent Characteristics of Layered Yttrium Oxide Nano-Phosphors Doped with Europium," *Journal of Applied Physics*, 121(12), p. 125111.

[168] Wakefield, G., Holland, E., Dobson, P. J., and Hutchison, J. L., 2001, "Luminescence Properties of Nanocrystalline Y2O3:Eu," *Advanced Materials*, 13(20), pp. 1557–1560.

[169] Schmechel, R., Kennedy, M., von Seggern, H., Winkler, H., Kolbe, M., Fischer, R. A., Xaomao, L., Benker, A., Winterer, M., and Hahn, H., 2001, "Luminescence Properties of Nanocrystalline Y2O3:Eu3+ in Different Host Materials," *Journal of Applied Physics*, 89(3), pp. 1679–1686.

[170] Das, G. K., 2010, "Rare Earth Doped Nanomaterials as Potential Contrast Agents for Optical/Magnetic Resonance Imaging," Nanyang Technological University.

[171] Yang, H., Zhang, D., Shi, L., and Fang, J., 2008, "Synthesis and Strong Red Photoluminescence of Europium Oxide Nanotubes and Nanowires Using Carbon Nanotubes as Templates," *Acta Materialia*, 56(5), pp. 955–967.

[172] Technologies, N., "Nanocomp Technologies' Products | Dispersed Products" [Online]. Available: https://www.miralon.com/dispersed-products. [Accessed: 28-Jan-2021].

[173] "Tomviz for Tomographic Visualization of Nanoscale Materials" [Online]. Available: https://tomviz.org/. [Accessed: 29-Jul-2021].

[174] Melnikov, P., Nascimento, V. A., Consolo, L. Z. Z., and Silva, A. F., 2013, "Mechanism of Thermal Decomposition of Yttrium Nitrate Hexahydrate, Y(NO3)3·6H2O and Modeling of Intermediate Oxynitrates," *J Therm Anal Calorim*, 111(1), pp. 115–119.

[175] Melnikov, P., Arkhangelsky, I. V., Nascimento, V. A., de Oliveira, L. C. S., Silva, A. F., and Zanoni, L. Z., 2017, "Thermal Properties of Europium Nitrate Hexahydrate Eu(NO3)3·6H2O," *J Therm Anal Calorim*, 128(3), pp. 1353–1358.

[176] Jack, K. H., and Goodeve, C. F., 1951, "The Iron-Nitrogen System: The Preparation and the Crystal Structures of Nitrogen-Austenite(γ) and Nitrogen-Martensite(α')," *Proceedings of the Royal Society of London. Series A. Mathematical and Physical Sciences*, 208(1093), pp. 200–215.

[177] Tessier, F., Navrotsky, A., Niewa, R., Leineweber, A., Jacobs, H., Kikkawa, S., Takahashi, M., Kanamaru, F., and DiSalvo, F. J., 2000, "Energetics of Binary Iron Nitrides," *Solid State Sciences*, 2(4), pp. 457–462.

[178] Hirai, H., and Kondo, K., 1991, "Modified Phases of Diamond Formed Under Shock Compression and Rapid Quenching," *Science*, 253(5021), p. 772.

[179] Wen, B., Zhao, J. J., and Li, T. J., 2007, "Synthesis and Crystal Structure of N-Diamond," *International Materials Reviews*, 52(3), pp. 131–151.

[180] Wen, B., Zhao, J., Li, T., Dong, C., and Jin, J., 2005, "N-Diamond from Catalysed Carbon Nanotubes: Synthesis and Crystal Structure," *J. Phys.: Condens. Matter*, 17(48), pp. L513–L519.

[181] Earp, B., Hubbard, J., Tracy, A., Sakoda, D., and Luhrs, C., 2021, "Electrical Behavior of CNT Epoxy Composites under In-Situ Simulated Space Environments," *Composites Part B: Engineering*, 219, p. 108874.

[182] Backes, E. H., Sene, T. S., Passador, F. R., and Pessan, L. A., 2018, "Electrical, Thermal and Mechanical Properties of Epoxy/CNT/Calcium Carbonate Nanocomposites," *Materials Research*, 21(1).

[183] Yang, C.-K., Lee, Y.-R., Hsieh, T.-H., Chen, T.-H., and Cheng, T.-C., 2018, "Mechanical Property of Multiwall Carbon Nanotube Reinforced Polymer Composites," *Polymers and Polymer Composites*, 26(1), pp. 99–104.

[184] Udupa, G., Rao, S. S., and Gangadharan, K. V., 2012, "Future Applications of Carbon Nanotube Reinforced Functionally Graded Composite Materials," *IEEE-International Conference On Advances in Engineering, Science and Management (ICAESM -2012)*, pp. 399–404.

[185] Samareh, J. A., and Siochi, E. J., 2017, "Systems Analysis of Carbon Nanotubes: Opportunities and Challenges for Space Applications," *Nanotechnology*, 28(37), p. 372001.

[186] Jen, Y.-M., and Yang, Y.-H., 2010, "A Study of Two-Stage Cumulative Fatigue Behavior for CNT/Epoxy Composites," *Procedia Engineering*, 2(1).

[187] Sampaio, J., Wnuk, E., Vilhena de Moraes, R., and Fernandes, S., 2014, "Resonant Orbital Dynamics in LEO Region: Space Debris in Focus," *Mathematical Problems in Engineering*, 2014, pp. 1–12.

[188] 2020, "LEO Parameters" [Online]. Available: http://www.spaceacademy.net.au/watch/track/leopars.htm. [Accessed: 22-Nov-2020].

[189] “Iridium Satellite Communications | Truly Global Communications,” *Iridium Satellite Communications* [Online]. Available: https://www.iridium.com/. [Accessed: 24-Nov-2020].

[190] “SpaceX Submits Paperwork for 30,000 More Starlink Satellites - SpaceNews” [Online]. Available: https://spacenews.com/spacex-submits-paperwork-for-30000-more-starlink-satellites/. [Accessed: 24-Nov-2020].

[191] Colton, K., Breu, J., Klofas, B., Marler, S., Norgan, C., and Waldram, M., 2020, “Merging Diverse Architecture for Multi-Mission Support,” *Small Satellite Conference*.

[192] “Congressional Hearing Held on Orbital Debris and Space Traffic,” July 2009. *Orbital Debris Quarterly News*.

[193] Banks, B.A., Miller, S., DeGroh, K., Demko, R., 2020, “Atomic Oxygen Effects on Spacecraft Materials” NASA Report No. 20030062195.

[194] Hopkins, A. R., Labatete-Goeppinger, A. C., Kim, H., and Katzman, H. A., 2016, “Space Survivability of Carbon Nanotube Yarn Material in Low Earth Orbit,” *Carbon*, 107, pp. 77–86.

[195] Ishikawa, Y., Fuchita, Y., Hitomi, T., Inoue, Y., Karita, M., Hayashi, K., Nakano, T., and Baba, N., 2019, “Survivability of Carbon Nanotubes in Space,” *Acta Astronautica*, 165, pp. 129–138.

[196] Kemnitz, R. A., Cobb, G. R., Singh, A. K., and Hartsfield, C. R., 2019, “Characterization of Simulated Low Earth Orbit Space Environment Effects on Acid-Spun Carbon Nanotube Yarns,” *Materials & Design*, 184, p. 108178.

[197] Cobb, G. R., O’Hara, R. P., Kemnitz, R. A., Sabelkin, V. P., and Doane, B. M., 2019, “Quantifying the Effects of Ultraviolet Type C Radiation on the Mechanical and Electrical Properties of Carbon Nanotube Sheet for Space-Based Applications,” *Materials Today Communications*, 18, pp. 7–13.

[198] Han, J.-H., and Kim, C.-G., 2006, “Low Earth Orbit Space Environment Simulation and Its Effects on Graphite/Epoxy Composites,” *Composite Structures*, 72(2), pp. 218–226.

[199] Awaja, F., Moon, J. B., Gilbert, M., Zhang, S., Kim, C. G., and Pigram, P. J., 2011, “Surface Molecular Degradation of Selected High Performance Polymer Composites under Low Earth Orbit Environmental Conditions,” *Polymer Degradation and Stability*, 96(7), pp. 1301–1309.

[200] Atar, N., Grossman, E., Gouzman, I., Bolker, A., Murray, V. J., Marshall, B. C., Qian, M., Minton, T. K., and Hanein, Y., 2015, "Atomic-Oxygen-Durable and Electrically-Conductive CNT-POSS-Polyimide Flexible Films for Space Applications," *ACS Appl. Mater. Interfaces*, 7(22), pp. 12047–12056.

[201] Garcia, M., 2015, "Space Debris and Human Spacecraft," *NASA* [Online]. Available: http://www.nasa.gov/mission_pages/station/news/orbital_debris.html. [Accessed: 22-Nov-2020].

[202] Earp, B., Dunn, D., Phillips, J., Agrawal, R., Ansell, T., Aceves, P., De Rosa, I., Xin, W., and Luhrs, C., 2020, "Enhancement of Electrical Conductivity of Carbon Nanotube Sheets through Copper Addition Using Reduction Expansion Synthesis," *Materials Research Bulletin*, 131, p. 110969.

[203] "Nanocomp Technologies' Products | Sheet/Tape" [Online]. Available: https://www.miralon.com/sheet/tape. [Accessed: 25-Mar-2021].

[204] "LACO Technologies Altitude - Presure Conversion Table" [Online]. Available: https://lacotech.com/system/resources/attachments/000/000/131/original/altitude_press_conv_table__low.pdf?1480452827. [Accessed: 22-Nov-2020].

[205] E21 Committee, 2020, *Standard Solar Constant and Zero Air Mass Solar Spectral Irradiance Tables*, ASTM International.

[206] Gueymard, C. A., 2004, "The Sun's Total and Spectral Irradiance for Solar Energy Applications and Solar Radiation Models," *Solar Energy*, 76(4), pp. 423–453.

[207] Ustun, T. S., Nakamura, Y., Hashimoto, J., and Otani, K., 2018, "Performance Analysis of PV Panels Based on Different Technologies after Two Years of Outdoor Exposure in Fukushima, Japan," *Renewable Energy*, 136.

[208] Shen, J. T., Buschhorn, S. T., De Hosson, J. Th. M., Schulte, K., and Fiedler, B., 2015, "Pressure and Temperature Induced Electrical Resistance Change in Nano-Carbon/Epoxy Composites," *Composites Science and Technology*, 115, pp. 1–8.

[209] Li, Q., Xue, Q. Z., Gao, X. L., and Zheng, Q. B., 2009, "Temperature Dependence of the Electrical Properties of the Carbon Nanotube/Polymer Composites," *Express Polymer Letters*, 3(12), pp. 769–777.

[210] Sanli, A., 2020, "Investigation of Temperature Effect on the Electrical Properties of MWCNTs/Epoxy Nanocomposites by Electrochemical Impedance Spectroscopy," *Advanced Composite Materials*, 29(1), pp. 31–41.

[211] Sheng, P., 1980, "Fluctuation-Induced Tunneling Conduction in Disordered Materials," *Phys. Rev. B*, 21(6), pp. 2180–2195.

[212] Mohiuddin, M., and Van Hoa, S., 2011, "Electrical Resistance of CNT-PEEK Composites under Compression at Different Temperatures," *Nanoscale Res Lett*, 6(1), p. 419.

INITIAL DISTRIBUTION LIST

1. Defense Technical Information Center
   Ft. Belvoir, Virginia

2. Dudley Knox Library
   Naval Postgraduate School
   Monterey, California